Wegener Center for Climate and Global Change
University of Graz

Scientific Report No. 69-2017

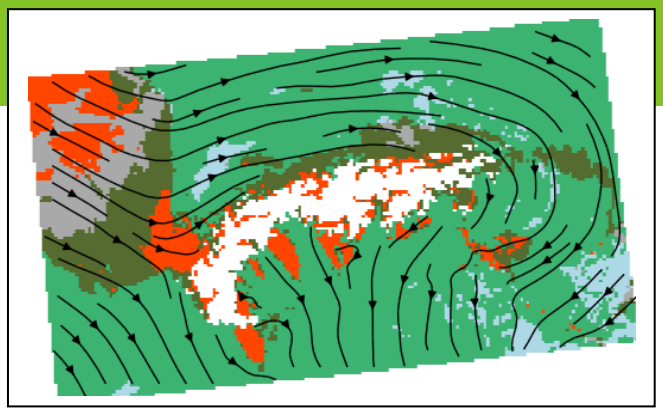

Using the Froude Number to Evaluate Modelled Flow-Above and Blocked-Flow Situations in Complex Terrain

Laurin Herbsthofer

June 2017

Financially supported by

FWF
Der Wissenschaftsfonds.

Wegener Center

UNI GRAZ

The **Wegener Center for Climate and Global Change** combines as an interdisciplinary, internationally oriented research institute the competences of the University of Graz in the research area “Climate, Environmental and Global Change”. It brings together, in a dedicated building close to the University central campus, research teams and scientists from fields such as geo- and climate physics, meteorology, economics, geography, and regional sciences. At the same time close links exist and are further developed with many cooperation partners, both nationally and internationally. The research interests extend from monitoring, analysis, modeling and prediction of climate and environmental change via climate impact research to the analysis of the human dimensions of these changes, i.e., the role of humans in causing and being effected by climate and environmental change as well as in adaptation and mitigation. (more information at www.wegcenter.at)

The present report is the result of a Master thesis work completed in December 2016. The work was funded by the Austrian Science Fund (FWF) under research grant P24758-N29 (project NHCM-2; www.nhcm-2.eu).

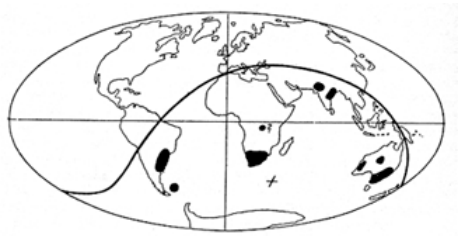

Alfred Wegener (1880–1930), after whom the Wegener Center is named, was founding holder of the University of Graz Geophysics Chair (1924–1930). In his work in the fields of geophysics, meteorology, and climatology he was a brilliant scientist and scholar, thinking and acting in an interdisciplinary way, far ahead of his time with this style. The way of his ground-breaking research on continental drift is a shining role model–his sketch on the relations of continents based on traces of an ice age about 300 million years ago (left) as basis for the Wegener Center Logo is thus a continuous encouragement to explore equally innovative ways:
paths emerge in that we walk them (Motto of the Wegener Center).

Wegener Center Verlag • Graz, Austria
© 2017 All Rights Reserved.
Selected use of individual figures, tables or parts of text is permitted for non-commercial purposes, provided this report is correctly and clearly cited as the source. Publisher contact for any interests beyond such use: wegcenter@uni-graz.at.

ISBN 978-3-9503918-6-2

June 2017

Contact: Laurin Herbsthofer
laurin.herbsthofer@gmx.at

Wegener Center for Climate and Global Change
University of Graz
Brandhofgasse 5
A-8010 Graz, Austria
www.wegcenter.at

Wegener Zentrum für Klima und
Globalen Wandel

Universität Graz

Masterarbeit
zur Erlangung des akademischen Grades
Master of Science
an der Naturwissenschaftlichen Fakultät der
Universität Graz

Using the Froude Number to Evaluate Modelled Flow-Above and Blocked-Flow Situations in Complex Terrain

Laurin Herbsthofer

Graz, Dezember 2016

Betreuer:
Mag. Dr. Heimo Truhetz

Abstract

The atmospheric flow behaviour of air in complex terrain plays an important role for weather phenomena such as mountain waves, downslope windstorms and barrier jets. Additionally, blocking events and orographically forced flows can lead to heavy precipitation events or sustained periods of warm temperatures (foehn winds), thus having a huge impact on our everyday weather. For any Regional Climate Model (RCM) to be meaningful it is necessary that these flow-above and blocked-flow situations are replicated correctly.

This work demonstrates how to use the Froude number of continuum mechanics to categorise the flow behaviour of air in the complex terrain of the European Alps on a grid cell resolution. The influences of moisture and especially condensation effects are also considered. Besides distinguishing flow-above from blocked-flow situations, it is shown how the calculation of the Froude number also provides information on the stratification properties of air.

In the framework of the project Non-Hydrostatic Climate Modelling, Part II (NHCM-2) (www.nhcm-2.eu), funded by the Austrian Science Fund (FWF), a tool based on this Froude number for automated flow analysis is developed. It is then used to study the differences between two RCMs (the COSMO model in CLimate Mode (CCLM) and the Weather Research and Forecasting Model (WRF)), both operating on convection permitting scale (3 km grid spacing). The analysis fields from the operational Swiss forecast system COSMO-7 (7 km grid spacing) are used as a reference data set. To compare the flow behaviour of these data sets, five distinct flow categories are introduced.

The frequency of occurrence of the flow categories for November 2002 based on hourly data is examined in detail using a horizontal cut through the domain at 1500 m above sea level. The influence of several free parameters within the tool is discussed. The located differences between the data sets highlight how this tool can help to improve RCMs and their accuracy regarding flow-above and blocked-flow situations and therefore contribute to model development.

Zusammenfassung

Das Strömungsverhalten der atmosphärischen Luftschichten spielt vor allem in Gebirgsregionen eine wichtige Rolle und ist für zahlreiche Wettersituationen verantwortlich. Angefangen von atmosphärischen Schwerewellen und Föhn bis hin zu Barrier Jets entlang von Gebirgen sind zahlreiche Phänomene auf die Interaktion zwischen Luftmassen und Topographie zurückzuführen. Vor allem große Gebirgsketten können Luftströmungen effizient blockieren oder vertikal Auslenken. Dadurch können starke Niederschlagsereignisse oder ungewöhnlich hohe Temperaturen beim sogenannten Föhnwind entstehen. Damit Regionale Klimamodelle (RCMs) aussagekräftige Ergebnisse liefern können, müssen diese Um- und Überströmungseffekte korrekt reproduziert werden.

Diese Arbeit demonstriert, wie die *Froude-Zahl* aus der Kontinuumsmechanik dazu benutzt werden kann, das Strömungsverhalten der Atmosphäre auf Basis von dreidimensionalen Daten zu kategorisieren. Die Einflüsse von Luftfeuchtigkeit (insbesondere Kondensationseffekte) werden dabei berücksichtigt. Neben der Unterscheidung von geblockten und nicht-geblockten Luftpaketen (*Um*strömung bzw. *Über*strömung) wird gezeigt, wie die Berechnung der Froude-Zahl dazu benutzt werden kann, die Lufstabilität zu analysieren.

Im Rahmen des Projektes Non-Hydrostatic Climate Modelling, Part II (NHCM-2) (www.nhcm-2.eu), finanziert durch den Fonds zur Förderung der wissenschaftlichen Forschung (FWF), wurde ein Tool zur automatisierten Kategorisierung des Strömungsverhaltens der Atmosphäre entwickelt. Mit Hilfe dieses Tools werden die Unterschiede zwischen zwei RCMs mit konvektionserlaubender Auflösung (3 km), dem COSMO model in CLimate Mode (CCLM) und dem Weather Research and Forecasting Model (WRF), sowie dem operationellen schweizer Wettervorhersagesystem COSMO-7 (7 km Auflösung) untersucht. Die Neuheit dieser Methode besteht in der dreidimensionalen Auflösung von fünf unterschiedlichen Strömungskategorien, welche im Zuge dieser Arbeit definiert wurden.

Die relative Häufigkeit dieser Strömungskategorien während einer Beobachtungsperiode von einem Monat (November 2002) wird auf Basis von stündlichen Datensätzen in 1500 m über dem Meeresspiegel analysiert. Der Einfluss von freien Parametern innerhalb des Tools wird diskutiert. Die im Allgemeinen lokal begrenzten Unterschiede zwischen CCLM, WRF und COSMO-7 zeigen auf, wie dieses Tool zur Verbesserung des Strömungsverhaltens von RCMs (sowie Klimamodellen im Allgemein) beitragen kann.

Acknowledgement

I would like to say a big thank-you to Heimo Truhetz for his supervision and for his great support concerning all issues of scientific and administrative nature. He always pointed me in the right direction while still giving me the opportunity to put my own ideas to the test. The presentation of parts of this work at an international conference would not have been possible without his encouragement.

Moreover, I am very grateful for the financial support from the project Non-Hydrostatic Climate Modelling, Part II (NHCM-2), which is funded by the Austrian Science Fund (FWF).

I really appreciate the fruitful discussions within the ReLoClim research group at the Wegener Center for Climate and Global Change that followed my presentations in the weekly group meetings. Many ideas that found their way into this work originated in these discussions. Also, thanks to all the amazing people who work at the Wegener Center for their help and the enjoyable lunch times we spent together and everyone that was involved in creating the LaTeX template that was used to write this thesis.

Finally, I would like to thank my parents for financial and emotional support throughout my years of study. Thanks also to my sister Stephanie and Constantin Schmidt for proofreading this thesis and to Stephanie Frei for her open ears and her encouragement, especially in difficult times. Without you, this work would not have been possible.

Contents

Abstract i

Zusammenfassung iii

Acknowledgement v

1 Introduction 1

2 Atmospheric Blocked-Flow and Flow-Above in Complex Terrain 3
- 2.1 Froude Number . . . 3
- 2.2 Idealised Examples . . . 5
- 2.3 Atmospheric Phenomena Linked to Orographically Forced Flow . . . 8

3 Development of a Froude Number Based Flow Analysis Tool 19
- 3.1 Flow Analysis Tool . . . 19
- 3.2 Search Algorithms for the Barrier Height Calculation . . . 21
  - 3.2.1 Straight Line Method . . . 22
  - 3.2.2 Cone Search Method . . . 23
  - 3.2.3 Precalculated Maximum Mountain Height Maps . . . 24
- 3.3 Calculation of the Brunt-Väisälä Frequency . . . 26
  - 3.3.1 Approximations . . . 26
  - 3.3.2 Moisture and Condensation . . . 27
  - 3.3.3 Temperature Field Selection Based on Relative Humidity . . . 28
- 3.4 Flow Categories . . . 29

4 Practical Application and Results 33
- 4.1 Experimental Setup . . . 33
  - 4.1.1 Models and Data Sets . . . 34
  - 4.1.2 Selecting Cases Using Weather Typing Schemes . . . 38
- 4.2 Properties of the Flow Analysis Tool . . . 39
  - 4.2.1 Influence of Different Parameters . . . 40
  - 4.2.2 Influence of Atmospheric Variables on Flow Categories . . . 43
  - 4.2.3 Vertical Distribution of Flow Categories . . . 45

4.2.4 Time Evolution of Flow Categories 48
4.3 Comparing Different Data Sets 48
4.3.1 Frequency of Occurrence for Flow Categories 51
4.3.2 Differences between WRF, CCLM and COSMO-7 51

5 Discussion and Conclusion **65**

Bibliography **67**

Acronyms **73**

List of Figures **75**

Appendix **81**
A Froude Number from Kinetic and Potential Energy 81
B Weighted Mountain Heights 83
C Atmospheric Modelling and Primitive Equations 85
D Grid Staggering in Atmospheric Models 90

1 Introduction

Understanding the flow behaviour of the lower atmosphere is of great significance for all aspects of atmospheric research. Short term weather forecasting, risk assessment concerning floods and droughts and even long term climate change simulations all require a solid knowledge of the interaction of air with topographic features. This interaction can lead to many familiar weather phenomena like the warm conditions of foehn winds, large scale precipitation events due to orographically forced flows or the high wind speeds of barrier jets (Chow et al. 2012). Since these situations can have a tremendous impact on our everyday weather, they are not only important to scientists but also to the general public. Large scientific research projects, like the Pyrenean Experiment (PYREX) (Bougeault et al. 1993) or the Mesoscale Alpine Programme (MAP) (Bougeault et al. 2001), are devoted to collect atmospheric data to help understand these phenomena.

Especially in complex terrain like the European Alps, it is crucial to develop tools and methods to characterise the atmospheric conditions that either lead to air flowing above a barrier (e.g. a mountain ridge) or situations where air is blocked and forced to move around a barrier (a so-called blocked-flow situation). This is important not only for weather forecasting, where the experience of meteorologists helped determine tomorrow's weather for ages, but also for modern numerical methods, which need to be able to capture all possible flow behaviours to produce meaningful output. Since these models are used for long-term climate change studies, scientists need to rely on their accuracy.

As a result of the ever increasing speed and capabilities of computers within the last decades, so-called Convection Permitting Climate Models (CPCMs) became feasible.

These simulations are able to cover regions like the European Alps at a 3 km grid spacing. However, since the convection parametrisations that have been used in simulations with coarser grid spacings are turned off in CPCMs, it is important to assess their flow behaviour to pinpoint differences between different models and the real atmosphere.

One way to study the flow behaviour of a fluid is to use the Froude number of continuum mechanics. This number is not only of great theoretical interest but it is also used in a variety of atmospheric applications, e.g. the study of heavy precipitation events (Schlemmer et al. 2010) or barrier jets (Olson 2008). However, most of these applications utilise the Froude number only in a qualitative way, using only a single value to characterise an entire atmospheric situation all at once. In contrast, the core of this work is the development of a *flow analysis tool* based on the Froude number that operates on three-dimensional data to study the flow behaviour at a grid cell resolution. The goal of this approach is to identify those air parcels that are able to move over a mountain ridge and separate them from air parcels that are being blocked. Since this is the crucial property that leads to the aforementioned weather phenomena, this method can help to study CPCMs at a grid cell resolution. Especially, it enables the comparison of CPCMs with data sets that resemble the past state of the atmosphere as close as possible, which is also part of this work.

Chapter 2 is devoted to the Froude number as well as atmospheric phenomena linked to orographically forced flows. Furthermore, it is shown how the Froude number can be used to describe the associated atmospheric conditions. An overview of the flow analysis tool that was developed during this work is presented in chapter 3. The flow categories, which are deduced from the computed Froude number values and stability properties of air, are presented there in detail.

Chapter 4 introduces the model data sets that are used to test the flow analysis tool. Also, an investigation of the most important parameters within the tool and its general performance in complex terrain are presented. This includes the vertical distribution of flow categories as well as their evolution in time. A comparison of the monthly frequency of occurrence of flow categories between different data sets is provided for the period of November 2002. Finally, the results are summarised and discussed in chapter 5.

2

Atmospheric Blocked-Flow and Flow-Above in Complex Terrain

Many important atmospheric conditions, like mountain waves or downslope windstorms, are related to orographically forced flows. These phenomena can be studied using the Froude number as introduced in section 2.1 based on wind speed, stability properties and the height of the involved mountains. While section 2.2 demonstrates its use in idealised examples, section 2.3 provides an overview of real atmospheric conditions that can be studied with the Froude number, thus highlighting the importance of understanding air flow in complex terrain. As shown in chapter 3, this approach can be extended to develop a flow analysis tool that represents the core element of this work.

2.1 Froude Number

Orographically forced flows that lead to interesting atmospheric phenomena like mountain waves or downslope windstorms require a very specific air flow pattern in order to occur. Most of these situations rely on air flowing over an obstacle while others only occur when air is blocked by a mountain and is forced to flow around this obstacle. Therefore, it is worth to develop a formalism that is capable of distinguishing flow-above from blocked-flow situations well in advance before the event even takes place without explicit simulation of the atmospheric variables. One way to achieve this task is the utilisation of the Froude number of continuum mechanics as explained hereafter.

William Froude originally introduced a dimensionless number F as a speed to length ratio to study the resistance of ships and boats at certain speeds (White 2003). However,

several different variations and definitions of this so-called *Froude number* are used today in a great variety of applications. A modern hydrodynamic definition (Newman 1977) involves the flow velocity U, the acceleration of gravity g as well as a characteristic length L of the problem under consideration:

$$F_{hydro} = \frac{U}{\sqrt{gL}} \,. \tag{2.1}$$

In a mathematically more rigorous formulation it appears together with the Reynolds number and the Euler number to simplify the equations of fluid dynamics, e.g. the Navier-Stokes equations for incompressible fluids. It also has wide applications in open channel flow (Chanson 2004) and can be used to distinguish stratified from turbulent flow of shallow water waves (Lin 2007). It can even be applied to geophysical mass flows like avalanches (see e.g. Takahashi (2014)).

Nevertheless, equation (2.1) can be considered as the ratio of internal forces of a fluid (inertia) to the external gravitational forces (Lin 2007). However, the equation in its presented form is only suitable to describe surface waves of a liquid where the restoring force is proportional to g. In the case of the atmosphere and its internal waves, the restoring force is proportional to the reduced gravity

$$g' = g\frac{\Delta\theta}{\theta} = g\frac{h\frac{d\theta}{dz}}{\theta} = hN^2 \,, \tag{2.2}$$

using the difference in potential temperature θ of two points that are separated by the distance h along the vertical coordinate z (see e.g. Baines (1998) and Sun and Sun (2015)). In the last step, this expression was further simplified using the definition of the Brunt-Väisälä frequency

$$N^2 = \frac{g}{\theta}\frac{d\theta}{dz} \,, \tag{2.3}$$

which is the angular frequency at which an air parcel oscillates within a statically stable environment if it is vertically displaced (Stull 1988). Section 3.3 provides a more detailed view on this variable as it can be used to incorporate moisture and condensation effects. Furthermore, it is shown that negative values for N^2 indicate unstable stratification.

Considering a mountain ridge as a barrier, the characteristic length L of this problem can be set to the mountain height h. Putting everything together, one obtains the final form of the Froude number F as it is being used throughout this work:

$$F = \frac{U}{\sqrt{g'L}} = \frac{U}{\sqrt{hN^2 \cdot h}} = \frac{U}{hN} \,. \tag{2.4}$$

To separate this definition from equation (2.1) (which uses a characteristic *length* rather than a barrier *height*) sometimes the non-dimensional mountain height $\hat{H} = 1/F$ is used

instead, stressing the fact that large mountains (large $\hat{H}$) are able to block flow from moving over it (Chow et al. 2012). Furthermore, this parameter may also be interpreted as describing the non-linearity of the flow (Reinecke and Durran 2008).

As argued by Sun and Sun (2015), equation (2.4) confirms that this definition of the Froude number represents the ratio of kinetic energy of an air parcel to the potential energy that is required to surmount a barrier in a stratified fluid flow. This interpretation makes the Froude number suitable to study flow-above and flow-around behaviour and their distinction (see e.g. Lin (2007)) .

A different view on the Froude number and its connection to kinetic and potential energy can be found in appendix A.

2.2 Idealised Examples

Two Dimensions

When studying idealised cases of the uniform flow of a liquid (e.g. water or air) in two dimensions, one typically uses a Gaussian shaped mountain as a barrier (Lin 2007) as seen in Fig. 2.1. The liquid shown in this figure is able to follow the shape of the mountain if it obeys $F > 1$ upstream of the barrier. In this so-called supercritical flow, the liquid has enough kinetic energy to surmount the potential energy required to overcome the mountain peak. On the other hand, if $F < 1$ (e.g. in the case of low velocities, high mountains or very stable stratification), the water surface decreases over the mountain peak as the fluid tends to reduce its potential energy upstream to gain kinetic energy directly over the mountain which is also known as the famous Bernoulli effect (Clancy 1975). In this scenario, it is possible that waves propagate upstream. This can lead to increased layer depth in front of the hill which in turn is responsible for increased potential energy of the fluid that can then be converted into kinetic energy to surmount the barrier (Lin 2007).

Another important effect that is related to the Froude number is the so-called hydraulic jump: if a liquid with high velocity enters a zone of low velocity, the surface of the liquid abruptly rises, converting some of the fluids kinetic energy into potential energy and turbulence. This shockwave-like behaviour can be found in the lee of mountains (Chanson 2009) or tap water that hits the kitchen sink and radiates outwards in a stratified manner until it transforms to turbulent flow at the hydraulic jump.

Meteorological situations related to the different flow regimes of Fig. 2.1 include orographically forced flows in which situations like upstream blocking events, wave breaking, severe downslope winds and lee vortices (Lin 2007) as well as mountain waves and barrier jets (Chow et al. 2012) can appear.

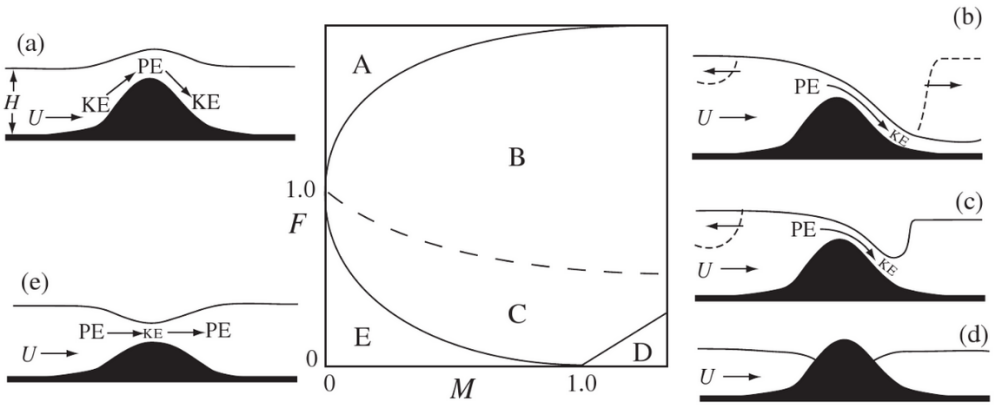

Fig. 2.1 Flow regimes for uniform two dimensional flow for different Froude number values. (a) super-critical flow for large Froude numbers; (b) flow with hydraulic jump that is propagating upstream and downstream; (c) flow with stationary hydraulic jump downstream and an upstream propagating jump; (d) completely blocked flow; (e) sub-critical flow for low Froude numbers. From Lin (2007).

Three Dimensions

To study these phenomena, a three dimensional model is needed to identify flow-above and flow-around (blocked-flow) regimes based on the Froude number F. In a three-dimensional model, if the upstream air possesses high F values, it can move over the barrier and in doing so it creates large amplitude mountain waves. If the Froude number of the upstream flow is small, the air tends to move around the barrier, creating a pair of counter rotating vortices in the lee (Lin 2007).

A more detailed description of three dimensional stably stratified flow may use a slightly different definition of the Froude number (Stull 1988):

$$F_{wave} = \frac{\pi U}{NW} \,, \tag{2.5}$$

where W is the length of the obstacle disturbing the flow and π is the circle constant. Considering that N is the frequency at which an air parcel oscillates vertically while it is embedded within an air mass moving horizontally at wind speed U, the oscillating air parcel creates a wave of wavelength $2\pi U/N$ in its trail. Since the effective wavelength of the disturbance is $2W$, it becomes obvious that a situation with $F = 1$ represents a *resonance condition* between the stratified air and the obstacle (Stull 1988). In fact, it is possible to observe several different flow phenomena in this idealised three-dimensional model which can be distinguished by the corresponding Froude number value F_{wave} of the uniform flow (see Fig. 2.2):

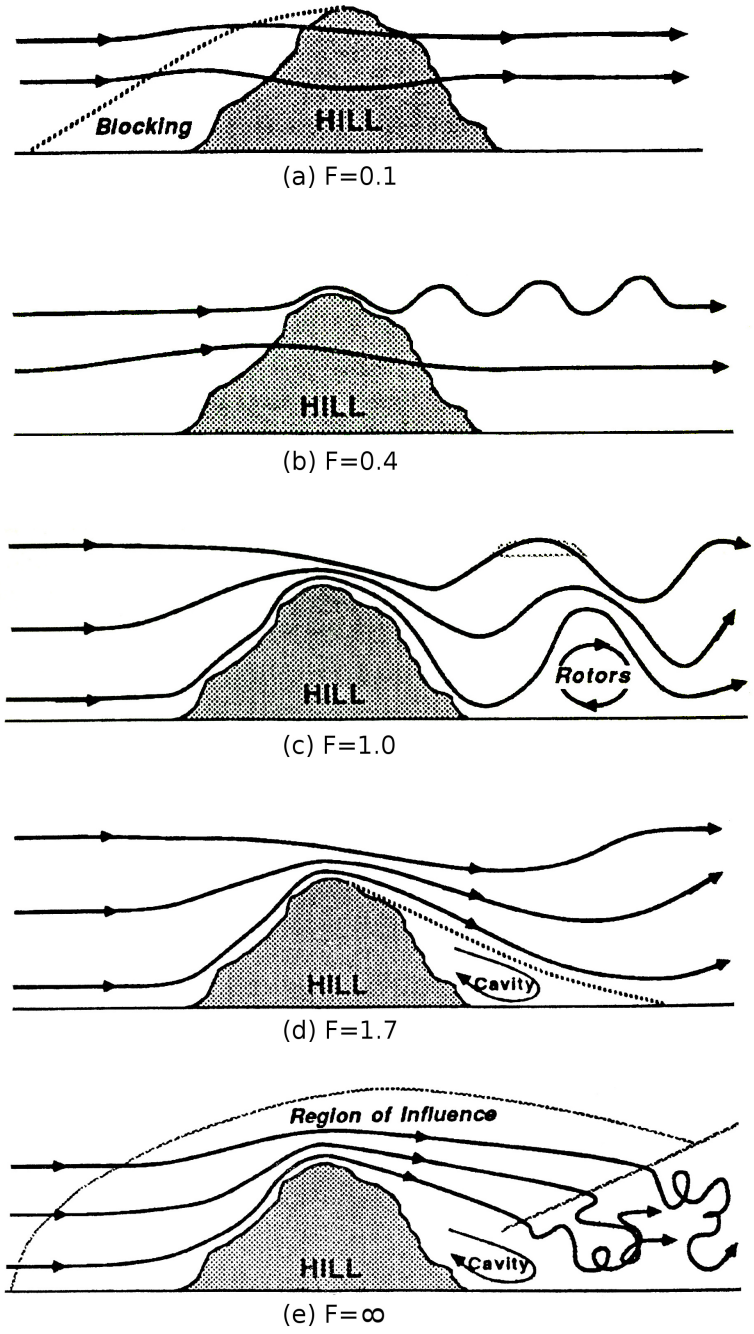

Fig. 2.2 Schematic illustration of flow over an isolated mountain for different Froude number values F_{wave} which compares the natural wavelength of air with the length of the obstacle. Adopted from Stull (1988).

- $F_{wave} \approx 0.1$: Upstream air is highly stable. It has only little kinetic energy and is forced to move around the obstacle rather than over it. Near the mountain some of the air is blocked, becomes stagnant and thus making the hill virtually longer since incoming air now needs to surpass the stagnant air as well. As a result, the obstacle becomes more streamlined.

- $F_{wave} \approx 0.4$: The impinging air has more kinetic energy and some of the high altitude air is able to move over the hill, forming lee waves due to the perturbation downstream of the hill (so-called lee-wave separation). The natural wavelength of the lee-waves is much smaller than the size of the hill. The fraction of the column of air (that was initially below the mountain top) that is able to move over the mountain is approximately equal to the value of F_{wave}.

- $F_{wave} \approx 1.0$: This is the resonance condition between incoming air and the length of the mountain. The stability is weaker and winds are stronger creating large amplitude lee/mountain waves. Rotor circulation behind the mountain is possible, leading to lenticular clouds if the air contains enough moisture.

- $F_{wave} \approx 1.7$: Strong winds with weak stability cause the natural wavelength to be larger than the width of the hill. This causes boundary layer separation and creates a cavity with reverse surface wind direction right behind the hill.

- $F_{wave} \to \infty$: Neutral stratification ($N \to 0$) and strong winds lead to very large values of F_{wave}. In this case wind-shadow effects are observed behind the hill which also is the start of a turbulent wake even farther downstream. An air parcel moving over the barrier either has large inertia (high wind speed) or low stability (small Brunt-Väisälä frequency) (Chow et al. 2012).

Another important result of this analysis reveals that wind at the crest of a gentle hill can be up to 60% faster then the impinging flow, which is a significant amount of kinetic energy that can be harnessed by wind-turbines stressing the importance of the Froude number for real-life applications (Stull 1988).

2.3 Atmospheric Phenomena Linked to Orographically Forced Flow

If atmospheric air flow is modified by mountains (or any orographic feature) a variety of weather phenomena important for our everyday weather can emerge. An air mass moving towards a mountain must either move over it, progress through gaps and valleys or, if it is being blocked, move horizontally around it to follow the pressure gradient that initiated its movement in the first place. Either way, some dynamically-driven wind phenomena, including mountain waves, gap winds and barrier jets (Chow et al. 2012)

are inevitable consequences depending on the path the air took. This section discusses the causes and consequences of some of these atmospheric conditions to highlight the importance of understanding flow-above and blocked-flow situations.

Mountain and Lee Waves

Fluid parcels that are vertically displaced from their equilibrium position produce buoyancy waves (internal gravity waves) as a result of (stable) stratification within the liquid that forces the fluid parcels back into their original position. If the disturbance is caused by lifting of air as it moves over an orographic obstacle (usually a high mountain or mountain ridge), the resulting waves are called mountain waves. Direct consequences of these waves include windstorms that form on the lee side of mountain ridges and so-called clear-air turbulences that are of great importance for aviation safety. The strongest of these waves are able to transport energy and momentum into the stratosphere, therefore having an impact on planetary circulation (Chow et al. 2012). Fig. 2.3 illustrates

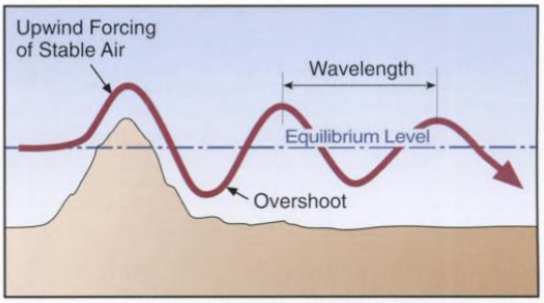

Fig. 2.3 Schematic illustration of the development of mountain waves. From Whiteman (2000).

the most important components of a mountain wave. Air with stable stratification is forced to move over an obstacle, cools down and sinks again once it has surpassed the barrier due to its increased density. After overshooting its equilibrium position it starts to oscillate vertically on the lee side of the obstacle. For this situation to occur, some of the incoming air that is still below the mountain peaks needs to obey $F > 1$ in order to surpass the mountain.

However, two different types of mountain waves can occur in this situation and they can be distinguished using the definition of the length-based Froude number F_{wave} (as introduced in section 2.2) of the impinging air mass. *Mountain waves* (Fig. 2.4a) form in the case of low F_{wave} values (broad mountains). This leads to waves that only propagate vertically and are often indicated by high lenticular clouds. *Lee waves* (Fig. 2.4b) occur in the case of higher F_{wave} values (narrow, steep mountains). Low lying lenticular clouds with regular spacing are an indicator for these (trapped) lee waves. Qualitatively

speaking: low values of F_{wave} lead to mountain waves that are only propagating vertically while higher F_{wave} values lead to waves that can propagate both vertically and horizontally.

The formation of these waves in the lee of a mountain is favoured by perpendicular flow over high and steep mountains. If the wind speeds are low, the generated waves will be rather shallow. However, if the wind speed is increasing (with even greater wind speeds in higher altitudes) the mountain wave can be accompanied by the formation of a standing lee eddy (Whiteman 2000).

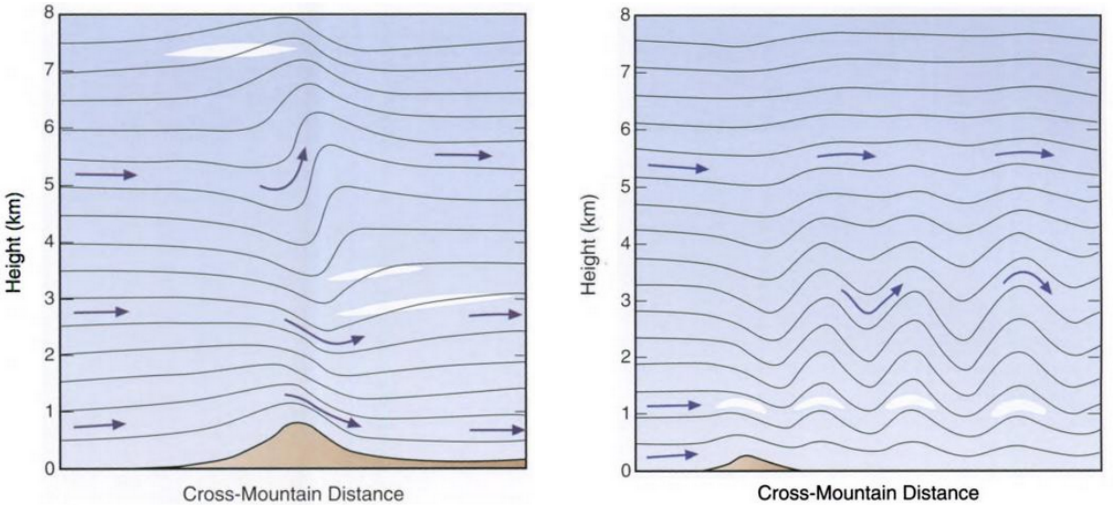

(a) Mountain waves. (b) Lee waves.

Fig. 2.4 Mountain waves and lee waves as generated by flow over a mountain. From Whiteman (2000).

Lee Wave Rotors

Mountain waves inevitably cause turbulences that may not always be restricted to higher altitudes. A so-called mountain wave rotor can form in the lee of a mountain causing low-level turbulence through recirculating airflow (Chow et al. 2012). These rotors lead to high near-surface wind speeds and are especially important for the transport of air pollutants and aviation safety (Lilly 1978).

Fig. 2.5 illustrates the development of lee wave rotors in an idealised, two-dimensional simulation. Note how the dark grey areas denote a small region of strong wind speeds near the ground that point into the opposite direction compared to the dominating air flow. Also, the second rotor farther downstream of the first is already much weaker.

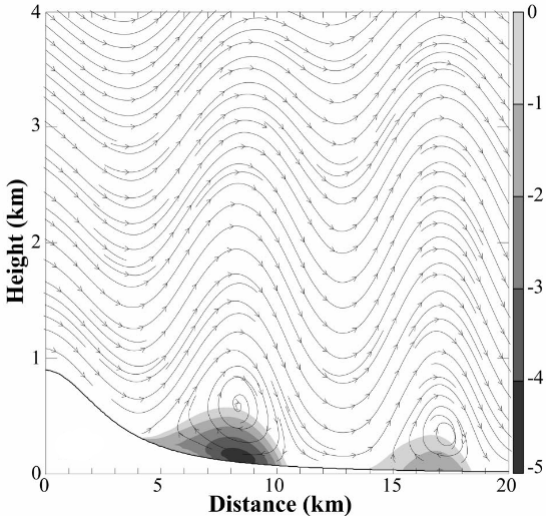

Fig. 2.5 Two lee wave rotors as simulated by Doyle and Durran (2002) for a two-dimensional idealised case. Streamlines depict airflow. Horizontal wind speeds to the left are shaded in grey. From Doyle and Durran (2002).

Downslope Windstorms

One important phenomenon that accompanies strong large-amplitude mountain waves are downslope windstorms which occur in many places around the world. They are highly relevant for regional weather conditions and are given local names such as Bora, Zonda, Boulder Windstorm, Bregenzer Fallwind, Santa Ana Winds and many others. These strong low-level flows accelerate down the lee slopes of a mountain and can reach wind speeds of up to three times the wind speed at the mountain top (Chow et al. 2012). Strong cross-barrier winds, a large mountain barrier and a stable atmosphere are required for these intense accelerations.

Fig. 2.6 shows the cross section of the 11 January 1972 downslope windstorm over Boulder (Colorado, U.S.A.) which was studied in great detail thanks to extensive aircraft observations. This figure highlights the importance of the preceding mountain wave that led to wind speeds as high as $60\,\mathrm{m\,s^{-1}}$. The mountain wave and a hydraulic jump (a region of abrupt discharge from kinetic to potential energy of the flow) between Boulder and Denver can be seen clearly in the potential temperature field.

A wide range of theoretical studies of downslope windstorms are also accompanied by a number of numerical studies,e.g. the Alpine Experiment (ALPEX, Smith (1987)) and the Pyrenees Experiment (PYREX, Bougeault et al. (1993)).

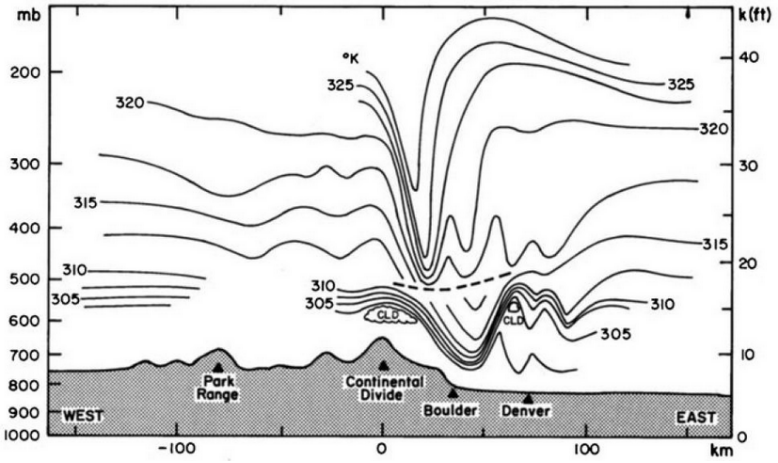

Fig. 2.6 The 11 January 1972 downslope windstorm over Boulder (Colorado, U.S.A.) in a cross section view. Potential temperature field is shown as black lines. From Klemp and Lilly (1975).

Foehn

Warm and dry downslope windstorms can occur in all mountain ranges and are in general called foehn winds (which is the generic term used in the European Alpine region). However, dozens of local nicknames for this phenomenon exist, such as Cape Doctor (South Africa), Sky Sweeper (Spain) or Chinook (U.S.A.) (Chow et al. 2012). Since they lead to higher temperatures on the lee side of a mountain ridge, these winds have a high societal impact since they are associated with pleasant weather. Foehn winds during winter may lead to a temperature increase of up to 25 °C within several hours, possibly resulting in summer-like weather, avalanches and sprouting of spring flowers (Marsh and Kaufman 2012). Therefore, it is not surprising that this phenomenon has been studied since the mid-1800s (see for example "Zur Frage über den Ursprung des Föhns" by J. Hann as early as 1866) (Seibert 2005). However, scientific knowledge has increased since then and an overview of a modern description of foehn winds is presented in the following.

In general, foehn occurs when air moves over a mountain ridge ($F > 1$) and reaches high temperatures in the lee of the mountains due to dry-adiabatic compression. However, two different types, foehn type I (or "Swiss foehn type") and foehn type II ("Austrian foehn type"), can be distinguished by the processes occurring on the windward side of the mountain ridge (Würsch and Sprenger 2015). Fig. 2.7 shows an example of the Swiss foehn type. Air from the south is moving northwards towards the Alps. Due to wet-adiabatic expansion and precipitation on the south side of the Alps, the air, now

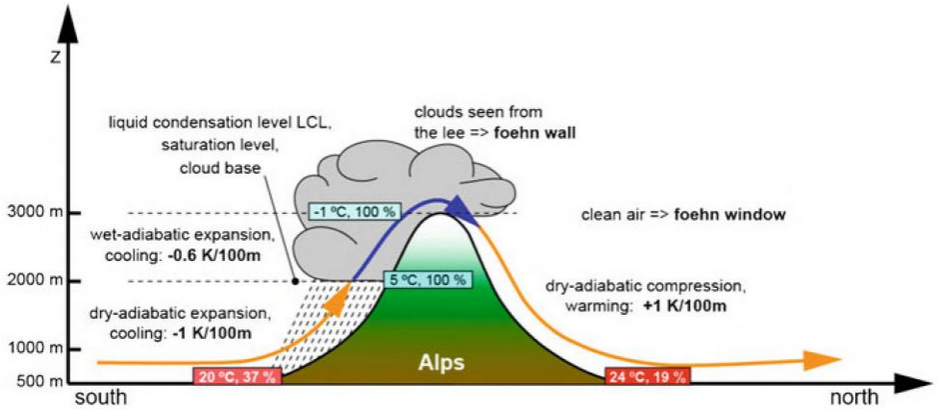

Fig. 2.7 Schematic illustration of the foehn type I ("Swiss foehn type"). From Chow et al. (2012).

disposed of its water content, is dry-adiabatically compressed in the lee of the mountains. Since the adiabatic lapse rates for wet and dry air are different, the dry air that has reached the north side of the Alps is significantly warmer than the initially moist air on the south side.

However, foehn winds can also occur without precipitation on the windward side of a mountain ridge. Fig. 2.8 shows a more general description of foehn situations. This description also includes blocked air on the windward side of the mountain ridge. If air from higher altitudes moves over this layer of blocked air and over the mountain peaks it finally descends in the lee of the mountain leading to higher temperatures through dry-adiabatic expansion. Whenever all of the air below the mountain peak is blocked, the resulting foehn is called foehn type II (Austrian foehn type) and is usually accompanied by only little or no precipitation at all on the windward side (Chow et al. 2012).

It is important to note that flow-above and blocked-flow are equally important for both foehn types. Also, the height of the mountain ridge itself has great influence on the occurrence of heavy precipitation events on the windward side. Furthermore, major valleys perpendicular to the mountain ridge experience the highest frequency of such foehn events (Richner and Gutermann 2007).

Orographically Forced Precipitation

Orographic precipitation is the result of moist air flowing over orographic features, therefore, $F > 1$ is required. This type of precipitation is responsible for floods and some of the heaviest annual rainfall events (Neiman et al. 2002). Examples for some of these heavy precipitation areas are the mountains of Hawaii within the trade wind belt or

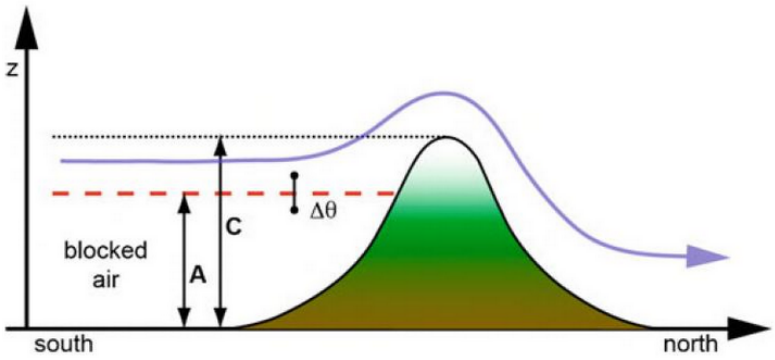

Fig. 2.8 Characterising foehn winds including blocked air (depth A). Foehn type I: $A = 0$ (no blocked air). Foehn type II: $A = C$ (all of the air below ridge height C is blocked). $\Delta\theta$ describes the difference in potential temperature between the blocked air and the air above. From Chow et al. (2012).

the Himalayan mountain front located in the path of the summer monsoon (Marsh and Kaufman 2012).

A representative example is shown in Fig. 2.9. Similar to the foehn type I, ascending moist air masses that are forced to move over a large mountain barrier lose their water content in a heavy precipitation event particularly on the windward side of the the barrier.

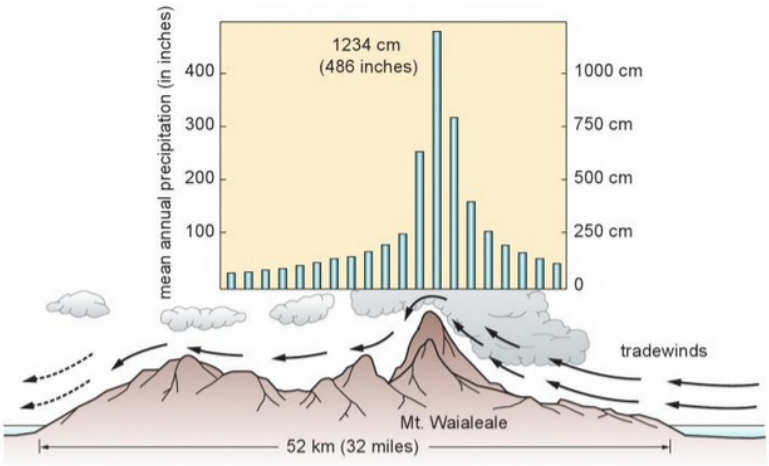

Fig. 2.9 Illustration of massive orographic precipitation on Mt. Waialeale, Hawaii. From Marsh and Kaufman (2012).

Although some of the impinging air has enough kinetic energy to surpass the mountain barrier in these precipitation events, blocked air may also play an important role. Fig. 2.10 shows how blocked flow modifies the area in which precipitation takes place: because the blocked air mass effectively acts as additional terrain upstream of the mountain ridge, precipitation occurs in a larger area and more upstream of the barrier then in the case without blocked air.

As shown with numerical studies by Watson and Lane (2012), the shape of the mountain ridge (e.g. being straight, convex or concave) has a significant influence on flow deceleration and the amount and spatial patterns of precipitation. Since heavy rainfall is responsible for flash flooding, which presents a significant threat to residents and local economy, it is important to understand and predict these events with great precision (Lin et al. 2001).

Barrier Jets

When a synoptic situation forces air against a steep barrier that is able to partially block the impinging air, barrier jets can occur that might exceed wind speeds of $30\,\mathrm{m\,s^{-1}}$ (Olson 2008). This is the case when $F < 1$ upstream of the barrier. The blocked air is forced up the barrier, cools adiabatically and creates higher pressure along the slope which in turn decelerates and blocks the flow. The air then becomes deflected by the barrier and starts accelerating parallel to the mountain ridge (as shown in Fig. 2.10, lower panel) as it needs to move towards the large scale pressure gradient (Parish 1982). The *classical barrier jet* of marine air is a very common phenomenon on the western coasts of continents.

These barrier jets usually require stably stratified flow that is blocked by the mountains for several hours or days to enable geostrophic adjustment between the high pressure along the slope and the flow itself (Chow et al. 2012). In the northern hemisphere this causes the flow to turn left due to reduced Coriolis forces. This sequence of blocking, turning and acceleration of wind is a well documented phenomenon in many regions, for example in Southeast Alaska (Lackmann and Overland 1989), Norway (Økland 1990) or Australia (Baines 1980).

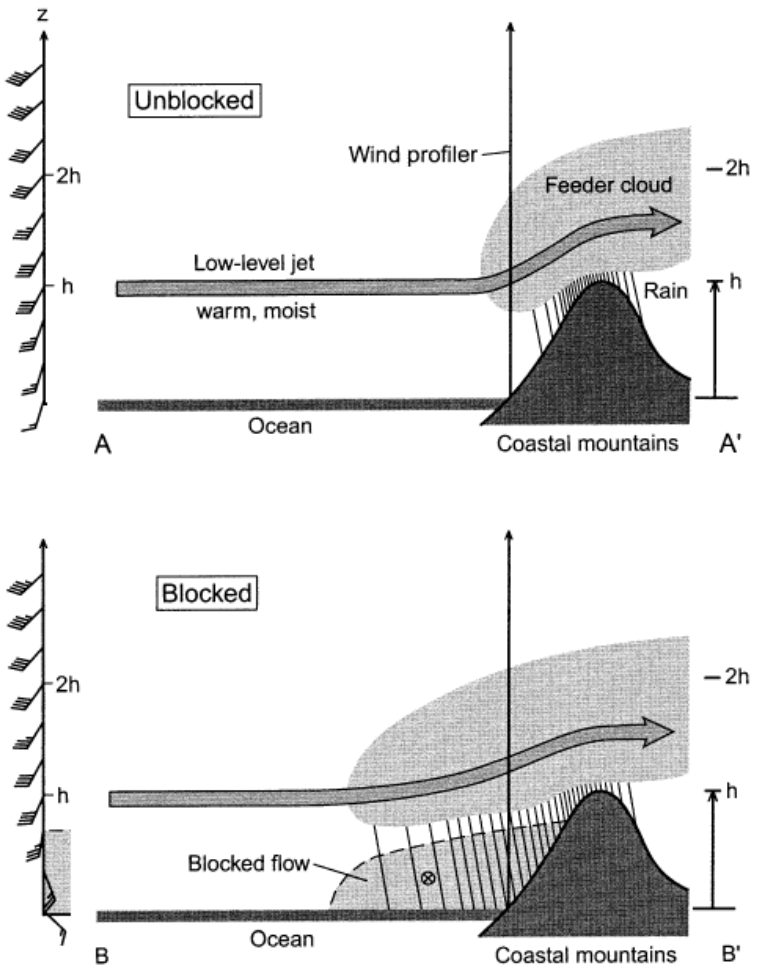

Fig. 2.10 Cross section view of orographically forced precipitation in the case of unblocked (upper panel) and blocked (lower panel) low-level flows towards coastal mountains. Coastal profiles of wind velocity shown on the left. The rain intensity is proportional to the spacing between rain streaks. The blocked flow in the lower panel moves parallel to the mountain ridge and forms a barrier jet. Adopted from Neiman et al. (2002).

The Froude Number in Atmospheric Research

Besides its importance for numerous theoretical models, the Froude number is also actively used in many different atmospheric applications and research fields. Some examples are given hereafter.

Schlemmer et al. (2010) investigated a heavy precipitation event south of the European Alpine region using re-analysis data from the European Centre for Medium-Range Weather Forecasts (ECMWF). To study the impacts of topography on the flow, an average (inverse) Froude number was computed. While the barrier height was set constant to 2000 m, wind speed U and Brunt-Väisälä frequency N were evaluated along a cross section across the Alps parallel to the wind field at 850 hPa to estimate their values for the whole impinging flow at once. The computed Froude number was then used to predict if the incoming air is being blocked by the mountains or not (low-level flow diversion). Finally, they established a link between the Froude number and potential vorticity anomalies which in turn were shown to be driving factors for extreme precipitation events in the Alps.

Another example involves the study of barrier jets and coastal wind jets where the Froude number can be used to identify situations that lead to the highest wind speeds along a barrier (see e.g. Overland and Bond (1995) and Olson (2008)). The scaling of length scales and magnitude of response for the region of blocked flow is related to the Froude number. Especially, a maximum coastal jet response is expected for cases where $F \approx 1$.

The numerical study *Nonlinear Flow Past an Elliptic Mountain Ridge* (Olafsson and Bougeault 1996) provides further in-depth information on how the Froude number can be used to study the occurrence of upstream blocking, the location of stagnation points, lee vortices, flow acceleration, wave breaking and areas of maximum surface wind in an idealised, three-dimensional simulation.

Miglietta and Rotunno (2009) studied the influence of several controlling parameters like Froude number and convective available potential energy (CAPE) on conditionally unstable flow in three dimensional simulations. Using an explicitely resolving cloud model, they investigated several parameter regimes that lead to (heavy) precipitation at different locations across the mountain ridge. Amongst other things, they showed that different mountain ridges and environmental wind speeds can lead to completely different flow patterns even if the Froude number is kept constant. This highlights the fact that the Froude number is only one piece in a larger puzzle to fully understand air flow over mountain ridges.

However, all of these examples have in common that only a *single* Froude number is used to evaluate the *entire* atmospheric situation in a large domain at any given moment. That is, only one value for wind speed, barrier height and stratification are considered, all of which are obtained by some form of averaging or through the selection of a small representative region. The novelty of the flow analysis tool presented in this work is that

the Froude number is evaluated at every grid cell of the domain independently, therefore providing three-dimensional analysis fields to study the flow behaviour of atmospheric situations in greater detail.

3

Development of a Froude Number Based Flow Analysis Tool

This chapter presents the core elements of the flow analysis tool and the underlying methods to calculate the barrier height and the Brunt-Väisälä frequency as well as the flow categories that emerge from this approach.

3.1 Flow Analysis Tool

To study the flow behaviour of climate models, a tool was developed that uses atmospheric variables to compute the Froude number $F = U/Nh$ (see equation (2.4)) individually for every grid cell of a given domain. This tool includes several steps that are carried out for each grid cell individually:

- the calculation of the barrier height in the direction of the air parcels movement in an efficient way,
- the calculation of the Brunt-Väisälä frequency based on the virtual and equivalent potential temperature and finally
- the classification into five distinct flow categories based on the calculated Froude number and the stability properties of the air parcel.

This section provides an outline of the most important features of this tool and how its components are calculated.

It may be noted at this point that using the simple definition of the Froude number is a vast approximation to the numerous atmospheric effects that influence the flow behaviour of air in complex terrain but which are to be neglected here. Furthermore, the Froude number itself is primarily a qualitative measure instead of a quantitative one as one might come to think by how it is being used within the flow analysis tool. That being said, the investigation of the quantitative capabilities of a three-dimensionally resolved Froude number is one of the main purposes of this work. The practical use of the flow analysis tool will almost always need specific tuning of parameters. Especially the value of the Froude number threshold F_{thresh} (as discussed in section 3.4) needs to be adjusted to fit real-life observations. Bearing this disclaimer in mind, the components of the flow analysis tool are to be introduced in the following.

Wind Speed

To measure the horizontal kinetic energy of an air parcel, its absolute wind speed U is used. It is straight forward to compute its value from the longitudinal and latitudinal wind components as provided by atmospheric models using

$$U = \sqrt{U_{long}^2 + U_{lat}^2} \, . \tag{3.1}$$

Low wind speeds will lead to a tendency towards blocked-flow situations while higher wind speeds favour flow-above. However, from a simple algorithmic point of view, the wind *direction* ϕ plays an even greater role within the tool, even if it does not enter the equation explicitly but through determining the maximum mountain height h in an air parcels path. The wind direction angle ϕ is computed using the generic $atan2$ function (as provided by many programming languages), giving the angle between a vector and the positive x-axis. Hence $\phi = 0$ denotes wind from west to east throughout this work.

Barrier Height

As outlined in section 2.1 the barrier height h is the *remaining* height between an air parcel located at height H_{air} and the highest point of orography (*largest mountain height*) H_m in the path of an air parcel if it continues travelling in the same direction as it was at the time of evaluation. h is then calculated by subtracting the height of the air parcel under consideration thus giving the remaining height that the air parcel needs to rise to be able to surpass the barrier:

$$h = H_m - H_{air} \, . \tag{3.2}$$

Negative values for h indicate that the air parcel is already above all orographic features that it is likely to encounter which self-evidently prohibits the occurrence of flow blocking. This reduced mountain height is similar to the *virtual* mountain height as suggested by Olafsson and Bougeault (1996) that is used for upper-level flow that is not being blocked

by a barrier.

Brunt-Väisälä Frequency

The last ingredient to calculate the Froude number F is the Brunt-Väisälä frequency N, named after David Brunt and Vilho Väisälä who studied the vertical oscillations of mass elements in static systems. When applied to atmospheric sciences, this angular frequency describes the rate at which an air parcel will oscillate around its equilibrium position due to buoyancy forces when it is vertically displaced:

$$N = \sqrt{\frac{g}{\theta}\frac{d\theta}{dz}}\,, \tag{3.3}$$

where θ is the potential temperature of air, g is the acceleration due to gravity and $d\theta/dz$ is the change of θ with respect to the vertical coordinate z that is pointing upwards into the atmosphere. Stronger stratification of air manifests itself through larger values of N. If the air parcel is not embedded in stable stratification (i.e. if $d\theta/dz < 0$) then N^2 is negative and hence N is an imaginary number. This prevents the algorithm from computing real valued Froude numbers. Although it is possible to extend the definition of F to be meaningful in the case $N^2 < 0$ (Schoellhamer et al. 1985), this extension is avoided in this work since it does not necessarily provide additional information to distinguish flow-above from blocked-flow situations.

Because the vertical derivative in its first order approximation uses only two points at different elevations (as shown later), it is necessary to use the potential temperature θ in equation (3.3) instead of just using real temperature T. θ makes the temperature of two air parcels at different height comparable by considering the air parcels temperature when they are moved adiabatically to mean sea level pressure. It is therefore computed using

$$\theta = T\left(\frac{p_0}{p}\right)^{R/c_p}\,, \tag{3.4}$$

with the pressure of the air parcel p, a reference pressure p_0 (e.g. sea level pressure), the gas constant of air R and the specific heat capacity for air at constant pressure c_p.

3.2 Search Algorithms for the Barrier Height Calculation

Computing the maximum mountain height H_m in an air parcels path requires the algorithm to scan the entire orography for the highest elevation that the air parcel will encounter. Recalling equation (3.2), this value is needed to compute the actual barrier height according to $h = H_m - H_{air}$. For sake of simplicity it is assumed that the air parcel continues to move into the same direction as it is at evaluation time.

Since a typical domain of interest (like the European Alpine region of Fig. 3.1) in a

reasonable resolution is likely to consist of more than $400 \times 250 = 100000$ grid cells, it is crucial that this part of the algorithm is carried out in a very efficient way. Naturally, there are several possibilities how to find this highest mountain and some of them will be examined in the following. Furthermore, one possible way to deal with large domains (e.g. a whole continent) is outlined in appendix B.

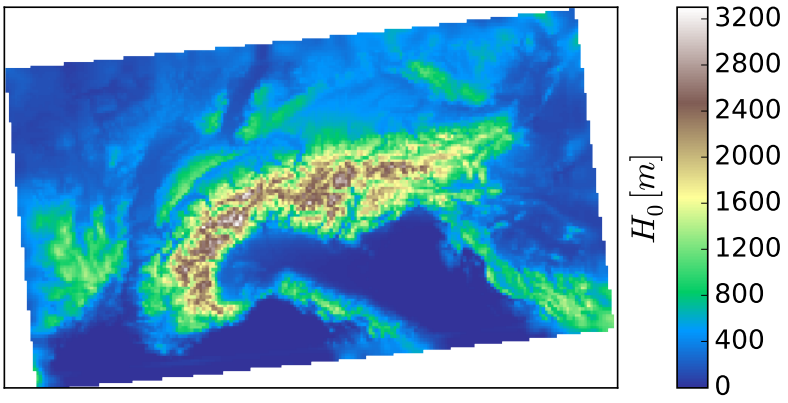

Fig. 3.1 Example orography of the Alpine region for which the maximum mountain heights need to be computed.

3.2.1 Straight Line Method

The Straight Line Method (SLM) is literally the most *straight forward* and simple approach for calculating the barrier height. A fictional straight line is drawn onto the orography field starting from the air parcels location and into the direction of its local wind direction. The highest point in the orography amongst all grid cells, which are directly adjacent to this line is computed and considered to be the *highest mountain* in the air parcels path. Fig. 4.5a in section 4.2.1 shows an example for obstacle height values computed using the Straight Line Method (SLM) for a real situation. However, to show how SLM works, Fig. 3.2 displays computed barrier height values if the wind direction was uniform across the whole domain (from bottom right to upper left). The highest mountain peaks of the Alps clearly cast shadow-like structures into a southeastern direction against the flow direction.

SLM assumes that the local wind direction carries significant information on the exact direction that any air parcel will travel. Since this straight line together with its directly adjacent neighbouring grid cells form a rather narrow path, it is very likely that a steep and high mountain (especially if it is far away from the air parcels initial position) may influence one air parcel but not the air parcels in its direct surrounding. This is expected to lead to significant noise.

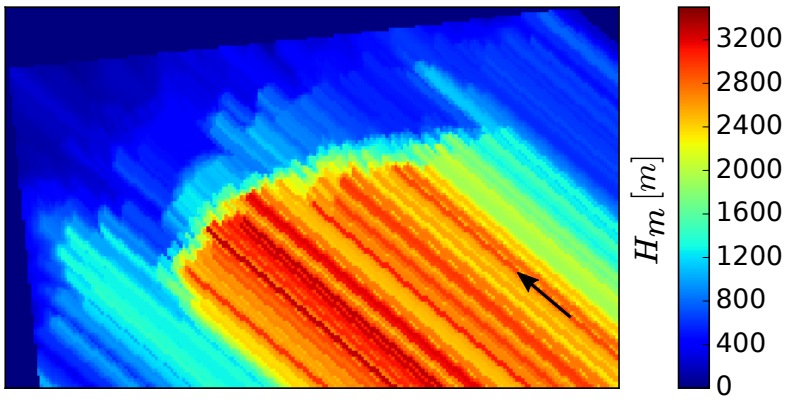

Fig. 3.2 Example for a maximum barrier height field H_m calculated using SLM if the wind direction is assumed to be uniform across the domain at a 140° angle (i.e. from southeast to northwest as denoted by the black arrow). Air parcel height is not yet subtracted.

On the contrary, SLM does not introduce any free parameters and is in this sense the most robust way of calculating the maximum mountain height. Therefore it is worth to study the computational cost of this algorithm to establish a benchmark for other algorithms.

A common application of this algorithm is to compute the flow behaviour of one layer of air located at a given constant geometric height. The domain under consideration is supposed to be quadratic with L grid points in both directions (with typically $L = \mathcal{O}(100)$). A typical search path that arises using SLM involves about L grid points (any factors accounting for the inclusion of adjacent grid points to the straight line are omitted). Therefore, the computational cost of SLM applied to the whole domain involves at least L^3 grid cells that have to be considered for the maximum mountain heights of all air parcels. This scaling behaviour will be used for comparison with other methods.

3.2.2 Cone Search Method

In a first attempt to remove local noise effects due to the narrow search path of SLM, a similar approach but with an ever increasing search path width is used. This Cone Search Method (CSM) introduces a new parameter, the cone opening angle α (or the half cone opening angle $\alpha/2$ as it is being used in section 4). To implement this method properly, all grid points within the search cone and the directly adjacent grid cells are considered when searching for the highest mountain. This solves issues that arise from mountains that are very close to the air parcel when the search cone did not open up

enough to capture even one grid cell in the vicinity of the air parcel. However, using $\alpha = 0°$ is identical to SLM of the previous section.

Using CSM reduces the influence of local wind direction and steep mountains especially for parts of the orography that are still far ahead of an air parcel. Neighbouring air parcels with similar wind direction tend to be assigned with a similar value for the maximum mountain height as opposed to SLM. However, this method still does not account for synoptic processes like cyclones that change an air parcels wind direction systematically before it reaches a possible barrier.

Fig. 3.3 shows an example maximum barrier height field if wind direction is assumed to be uniform across the whole domain. In comparison to Fig. 3.2, it can be seen that single mountain peaks do not create as many sharp lines within the field. However, sharp transitions are still prominent at the edges of the search cones. Fig. 3.3 is also exactly one of the fields that is being used in the maximum mountain height map (MMHM) approach (section 3.2.3).

Note that the way CSM is constructed, it tends to produce larger maximum mountain height values than SLM since more grid cells are taken into account in every single search procedure. As larger mountains lead to more detected blocking events, a direct comparison between these two methods should reveal more blocking situations for CSM. However, the CSM approach strengthens the meaning of detected flow-above situations since, on average, larger barrier heights need to be surpassed in this method.

The free parameter α describing the cone opening angle can be used to adjust to different large scale flow situations: if the wind direction is spatially changing fast within the domain, a larger value for α will produce more meaningful results. On the other hand, if wind direction is more or less constant or changing slowly, then a small value for α leads to a more precise calculation. Values for α below 20° are found to be suitable for domains covering the European Alpine region.

Investigating the computational cost of the CSM reveals that it scales even worse than L^3 especially for large values of α since larger areas are considered in the search process.

3.2.3 Precalculated Maximum Mountain Height Maps

When applying the search algorithms discussed in the previous sections to several consecutive time steps or many different height layers it becomes obvious that nearly the same computations are done over and over again when searching for the maximum mountain height - especially if the wind direction is changing only slowly over time or with height. Since H_m does only depend on the current wind direction, a *pre-calculation* of all necessary H_m values becomes feasible. These values can be stored and accessed by the algorithm when needed. To compute the barrier height h needed for the Froude number, the air parcel height still needs to be subtracted according to (3.2).

These pre-calculated values are stored in the maximum mountain height map (MMHM)

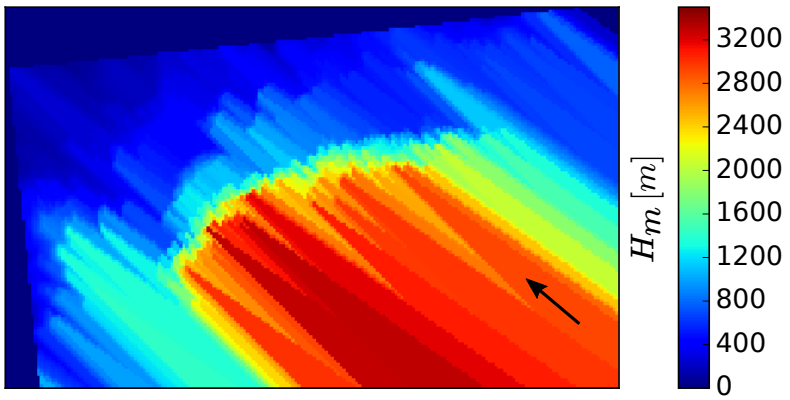

Fig. 3.3 Example for a maximum barrier height field H_m calculated using CSM if the wind direction is assumed to be uniform across the domain at a 140° (i.e. from southeast to northwest as denoted by the black arrow). Air parcel height is not yet subtracted.

that only depends on the orography and explicitly *not* on any wind direction field or detection height. Being applicable for both SLM and CSM, this method calculates the maximum mountain height H_m for every grid cell *in every direction* prior to calculating any Froude numbers. Once this map is created it can be used over and over again for the same domain even for different detection heights since the values stored in MMHM are independent of air parcel height.

Since it is not feasible to calculate every possible wind direction in advance, a new free parameter, the angle resolution γ, is introduced, which is linked to the number of search directions SD included in MMHM as $SD = 360°/\gamma$. This means that a value of $\gamma = 10°$ leads to $SD = 36$ different search directions which are to be considered and stored in MMHM. In general, higher values for SD will lead to more accurate approximations as explained in the following.

Fig. 3.3 already showed an example for one field that is part of a MMHM using CSM for one specific wind direction. Once this map is calculated for every of the SD many wind directions, it is possible to get an approximate value for H_m for an arbitrary wind direction through interpolation of the H_m values of two MMHM fields. E.g., to calculate H_m for an air parcel with wind direction $\phi = 8°$, a linear interpolation between the values from MMHM for wind direction 0° and 10° is performed.

This method works best using CSM since it does not need many search directions because it is still possible to scan the entire orography without a gap compared to SLM. This is achieved by using values for SD such that the resulting angle resolution γ is smaller than the cone opening angle α of CSM. This condition ensures that every orographic feature is captured in MMHM.

3.3 Calculation of the Brunt-Väisälä Frequency

The Brunt-Väisälä frequency is the most versatile ingredient in the Froude number since it allows for the incorporation of moisture and condensation effects but relies on approximations as outlined in this section.

3.3.1 Approximations

In idealised situations of constant wind speed and stratification it is fairly simple to compute N since it does not vary vertically. However, in real situations a proper method to estimate the derivative in (3.3) has to be found. Two possible methods were proposed by Reinecke and Durran (2008). The first one uses an averaging approach that integrates $N(z)$ from the ground level H_0 to the elevation of the air parcel H_{air},

$$N_A = \frac{1}{H_{air} - H_0} \int_{H_0}^{H_{air}} N(z) dz \ , \tag{3.5}$$

while the second one is known as the bulk method,

$$N_B = \sqrt{\frac{g}{\theta_0} \frac{\theta_{air} - \theta_0}{H_{air} - H_0}} \ , \tag{3.6}$$

which uses a reference value for the potential temperature at the ground θ_0 whereas θ_{air} represents the air parcel at elevation H_{air}. This result is obtained by using a simple first order approximation for the derivative in (3.3).

As shown by Reinecke and Durran (2008), the averaging method leading to N_A is best to study flow reversal behaviour while the bulk method for N_B is to be favoured when predicting flow diversion. Therefore, equation (3.6) will be used to estimate N within the algorithm but with a slight modification. Instead of using a reference air parcel at the bottom of the atmosphere (θ_0), an air parcel that is at a higher elevation is used, namely at the highest mountain height H_m in the air parcels path. The modified equation then reads

$$N_B = \sqrt{\frac{g}{\theta_{air}} \frac{\theta_{H_m} - \theta_{air}}{h}} \ , \tag{3.7}$$

whereas h is the remaining barrier height as defined in equation (3.2). The reason for this modification is that we are interested in the column of air above an air parcel rather than below it since we are especially considering cases where air parcels are lifted upwards to overcome a mountain and hence has to interact with the air above it. Fig. 3.4 sums up this method.

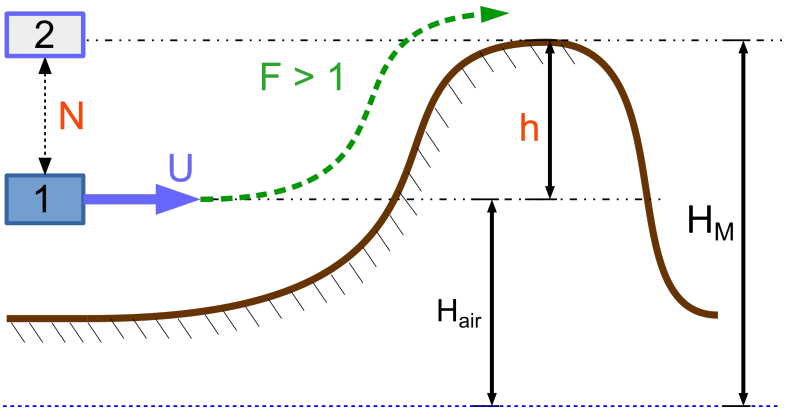

Fig. 3.4 Schematic illustration of the components of the algorithm: an air parcel (1) at height H_{air} is approaching a mountain of height H_m with wind speed U; the remaining barrier height is h. The Brunt-Väisälä frequency N is calculated using a reference air parcel (2) at height H_m. If the computed Froude number fulfils the condition $F > 1$, the air parcel is able to move over the mountain.

3.3.2 Moisture and Condensation

Dry air

The simplest way to calculate N is using just the potential temperature as shown in (3.3). However, this assumes dry air and the corresponding Brunt-Väisälä frequency will therefore be called N_{dry} to avoid confusion with different notations found in the literature.

Moist Air

In order to incorporate moisture into the algorithm, a new temperature field, the virtual potential temperature θ_{virt}, can be used to replace θ in (3.3). This is the potential temperature of a virtual, dry air parcel that has the same total pressure and density as the moist air under consideration, thus:

$$\theta_{virt} = T_v \left(\frac{p_0}{p} \right)^{R/c_p} , \tag{3.8}$$

where T_v is the virtual temperature as defined by:

$$T_v \approx (1 + 0.61r)T , \tag{3.9}$$

with r being the mixing ratio of water in air. It can be computed using the specific humidity q as provided by many atmospheric modelling data sets using

$$r = \frac{q}{1-q} \ . \tag{3.10}$$

It can easily be seen that θ_{virt} is larger for air with higher moisture content. The Brunt-Väisälä frequency computed using θ_{virt} will be called N_{moist} in the following.

Saturated Air

In situations of very high relative humidity, condensation due to lifting of air parcels is likely to take place and the corresponding heating effects need to be taken into account. It is therefore feasible to replace θ with the equivalent potential temperature θ_{equiv} which is the potential temperature of an air parcel when all of its contained water vapour releases its latent heat content through condensation. This leads to

$$\theta_{equiv} = T_e \left(\frac{p_0}{p} \right)^{R/c_p} \ , \tag{3.11}$$

where T_e is the equivalent temperature as defined by

$$T_e = T + L_v/c_p \cdot r \ , \tag{3.12}$$

with L_v being the latent heat of evaporation. It can be approximated by empirical formulas, e.g.

$$L_v(T) = (2500.8 - 2.36 \cdot T_C + 0.0016 \cdot T_C^2 - 0.00006 \cdot T_C^3) \cdot 1000 \ [J/kg] \ , \tag{3.13}$$

with T_C denoting temperature in Celsius (see e.g. Rogers and Yau (1989)). If θ_{equiv} is being used for calculations, the corresponding Brunt-Väisälä frequency will be denoted as N_{sat} (referring to situations of saturation).

Table 3.1 sums up the different ways that the Brunt-Väisälä frequency can be computed.

3.3.3 Temperature Field Selection Based on Relative Humidity

Since in the limit of very dry air ($r \to 0$) we find that $\theta_{virt} \to \theta$, it is sufficient to calculate N_{moist} for nearly all atmospheric conditions while omitting the use of N_{dry} completely. As we have seen, this is not true for situations of high water vapour content (large r), where also N_{moist} is not appropriate. The algorithm will therefore automatically switch (for every grid cell individually) from using N_{moist} for most of the situations to using N_{sat} if the relative humidity exceeds a certain threshold. The relative humidity RH is

Tab. 3.1 Overview of the three different ways to calculate the Brunt-Väisälä frequency N based on different temperature fields and their application within the algorithm.

Temperature field	N	*Application*
Potential temperature θ	N_{dry}	Dry air
Virtual pot. temperature θ_{virt}	N_{moist}	Moist air
Equivalent pot. temperature θ_{equiv}	N_{sat}	Saturated air

defined as the ratio of water vapour pressure e to the saturation water vapour pressure e_s. This can be approximated by the ratio of specific humidity q to the specific humidity for saturation q_s:

$$\begin{aligned} RH[\%] = 100 \cdot \frac{e}{e_s} &\approx 100 \cdot \frac{q}{q_s} \\ &\approx 100 \cdot \frac{q}{0.622 \cdot e_s/p} \,, \end{aligned} \tag{3.14}$$

whereas $q_s \approx 0.622 \cdot e_s/p$ was used. To calculate e_s, any empirical relation like the Magnus formula or the Murray relation

$$e_s = 6.1078 \exp\left(\frac{17.27(T - 273.16\,\mathrm{K})}{T - 35.86\,\mathrm{K}}\right) \,, \tag{3.15}$$

for the saturation water vapour can be employed (Kraus 2007).

As shown by Hughes et al. (2008), using a threshold of $RH_{thresh} = 90\%$ is a meaningful value for the transition between N_{moist} and N_{sat} and the exact value of this threshold is not relevant for the results as long as it is chosen form the interval $85\% - 95\%$.

It may be noted that the reason for the threshold being chosen from said interval is based on physics and not mathematics since there is no analytical transition between N_{moist} and N_{sat} at this specific value for RH. This is obvious since the physical effects behind θ_{virt} and θ_{equiv} are completely different.

3.4 Flow Categories

As it turns out, the Froude number itself is not well suited to make quantitative comparisons of the results. This stems from the fact that it is sometimes not defined (unstable stratification) or incredible high ($F > 10000$ because of small values for N and h that

Tab. 3.2 Overview of the five different flow categories and their properties. The Froude number threshold to separate categories BF and FA was set to $F_{thresh} = 1$. $h > 0$ denotes air parcels that are still below the highest mountain in its path.

Category	*Description*	F	*Stratification*	$h > 0$	*Flow*
BF	blocked flow	< 1	stable	yes	blocked
FA	flow above	> 1	stable	yes	above
FAtriv	trivial flow above	*irrelevant*	stable	no	above
USFAtriv	Unstable with trivial flow above	*imaginary*	unstable	no	above
US	Unstable with unknown flow behaviour	*imaginary*	unstable	yes	unknown

might occur) as compared to its typical values of $F < 10$. This makes the calculation of quantities such as spatial or temporal averages of the Froude number meaningless. However, this naturally leads to the introduction of *flow categories* that use all the information provided by the algorithm: the Froude number F, stratification properties and the relative location of an air parcel to the highest mountain in its path. Table 3.2 shows the five different flow categories that capture the whole spectrum of possible flow situations and are explained in the following.

Most of the results shown in chapter 4 will also contain the pseudo-category *Terrain* which simply denotes grid cells that are below orography and hence do not provide any atmospheric information.

Blocked Flow

The Blocked Flow (BF) flow category is attributed to grid cells that are stably stratified and the computed Froude number is between 0 and a defined threshold F_{thresh}. In this work, the threshold is set to $F_{thresh} = 1$ which is the natural threshold when interpreting the Froude number as the ratio between kinetic and potential energy (see section 2.1). However, higher threshold values may also be used, see e.g. Smolarkiewicz and Rotunno (1990). Also, air parcels of this category are always required to be at a lower altitude than the highest mountain that they are approaching, otherwise blocking events are not possible. BF air parcels usually approach the mountain ridge that is blocking them until they deviate from their flow direction to move around the obstacle rather than over it (McCauley and Sturman 1999).

Flow Above

Similar to BF, the Flow Above (FA) flow category applies only to air parcels with stable stratification that are located at lower altitudes than the highest mountain in their path. However, FA air parcels possess enough kinetic energy to surmount the mountains, which is indicated by Froude number values larger than 1. Since these air parcels are initially lower than the mountains, these events can be considered *true flow above* situations since the air is lifted during the process.

It is important to note that the category FA alone does not account for all air parcels that are able to follow their initial wind direction without orographic blocking. A combination of FA with the categories FAtriv and USFAtriv (as discussed below) captures the full spectrum of *freely flowing* air parcels.

Trivial Flow Above

Air parcels being labelled as Trivial Flow Above (FAtriv) are not blocked by any mountain solely because their initial height is already higher than any obstacle in their path. Nevertheless, stable stratification is required for this category. Since there is no real blocking or lifting involved, the computed Froude numbers for these air parcels are irrelevant.

Unstably Stratified Air with Trivial Flow Above

Similar to FAtriv, air parcels of the Unstably Stratified Air with Trivial Flow Above (USFAtriv) flow category are able to move across any mountain in their path because they are already located at high enough altitudes. However, these air parcels are embedded in unstable stratification and are therefore preventing the algorithm from computing any meaningful (real valued) Froude numbers.

Unstably Stratified Air

Air parcels of the Unstably Stratified Air (US) flow category are located within unstable stratification. This is a result from the calculated squared Brunt-Väisälä frequency being negative (and thus an imaginary value for N) leading to an imaginary Froude number. In this case, the computation of F is omitted in the algorithm (as explained in section 3.3).

To identify the whole spectrum of unstably stratified air, the combination of flow categories US and USFAtriv needs to be considered. It may be noted that this algorithm is not perfectly suited for applications where only the differentiation between stable and unstable air is of interest. As shown in Fig. 3.4, the algorithm uses two different values from the temperature field to compute the Brunt-Väisälä frequency: the value at the air parcels location and the value in the same column of air but at the height of the highest

mountain peak in the air parcels path. As long as the air parcel of interest is below the mountains that it is approaching, this second reference air parcel is located at a higher altitude. If this is not the case, then the reference air parcel is located at a lower altitude than the air parcel of interest to avoid the need for another free parameter within the algorithm. This, however, leads to an inconsistent way of computing stability since it now depends on wind direction and the orography of the whole domain.

A simple solution to this problem would be to always use a reference air parcel that is at a fixed height above the air parcel. Although this would lead to a more consistent calculation of stratification, the algorithm would deviate from its initial goal of capturing the effects of the air column that is most relevant for distinguishing flow-above from blocked-flow situations: the remaining air above the air parcel reaching to the height of the obstacle.

4
Practical Application and Results

This chapter shows how the developed flow analysis tool can be applied to the different data sets introduced in section 4.1.1 and how to interpret the computed results. A method that can highlight differences in the flow behaviour of these data sets is established. Section 4.2 explains the basic setup that is used for most of the presented results but also the influence of different parameter settings. These different settings include a variety of ways to calculate the obstacle height as well as different threshold values for relative humidity and the Froude number (to separate blocked-flow from flow-above). Detailed discussions of the vertical distribution (section 4.2.3) and time series (section 4.2.4) are provided. Finally, the results from two Regional Climate Models (RCMs) for the period of November 2002 are compared to results from the operational Swiss forecast system COSMO model version 7 (COSMO-7) using the monthly frequency of occurrence for the different flow categories.

4.1 Experimental Setup

This section introduces the three different data sets that are used in this work and shows all necessary preprocessing that needs to be done in order to compare the results. Furthermore, a simple weather typing scheme is introduced which is used for evaluation later on.

4.1.1 Models and Data Sets

Since there is no detailed three-dimensional information available on the past or present state of the atmosphere, the flow analysis tool heavily relies on data from atmospheric models (see appendix C). Two different RCMs, operating at convection permitting scale, that are used to test the flow analysis tool, namely the COSMO model in CLimate Mode (CCLM) (Böhm et al. 2006) and the Weather Research and Forecasting Model (WRF) (Skamarock et al. 2008), are introduced in this section. Since many atmospheric models use a spatial grid staggering for the three wind components, appendix D explains the details of this grid layout and explains how to convert the variables to be defined on comparable locations. Furthermore, to establish a way to enable the comparison of results from these RCMs to data that resembles the real past state of the atmosphere as realistically as possible, the operational Swiss forecast system COSMO-7 is presented.

CCLM - COSMO Model in Climate Mode

CCLM (Böhm et al. 2006) is a climate version of the COSMO Limited-area Modelling (LM) (see e.g. Steppeler et al. (2003) and Doms and Baldauf (2015)). LM itself is the operational, non-hydrostatic mesoscale weather forecast model that was developed by the German Weather Service (DWD) and the COnsortium for Small scale MOdeling (COSMO). Non-hydrostatic expresses the fact that the spatial grid is so fine-grained, that the hydrostatic assumption can be dropped because convective phenomena are now resolved explicitly (therefore being a convection-permitting climate model), reaching grid resolutions of about 20 km and below to get access to the resolution required to study regional climate impacts (Böhm et al. 2006).

CCLM does not simulate all of earth's atmosphere but only a smaller sub-region (here the COordinated Regional climate Downscaling EXperiment - EUROpean domain (EURO-CORDEX) (Jacob et al. 2014)), as seen in Fig. 4.1. This figure also shows that the lateral boundary conditions for this simulation is provided by a global European Centre for Medium-Range Weather Forecasts Re-Analysis Interim (ERA-Interim) data set (Dee et al. 2011).

At its core, CCLM consists of Navier-Stokes equations for compressible flow with a multicomponent fluid (dry air, water vapour, liquid and solid water) representing the atmosphere. Despite the high resolution, several parametrisations are still required, e.g. to represent sub grid-scale turbulence or radiation (Doms and Baldauf 2015).

The data that is being used throughout this work was generated by Klaus Keuler (BTU Cottbus) using the model version CCLM5.00_clm3. Like all other versions of CCLM, it uses generalised terrain-following height coordinates. Since the flow analysis tool is designed to work on geometric height levels, a conversion between height-based hybrid coordinate μ and geometric height z is needed. Following the description in Doms and Baldauf (2015), z is calculated using model orography height h at position

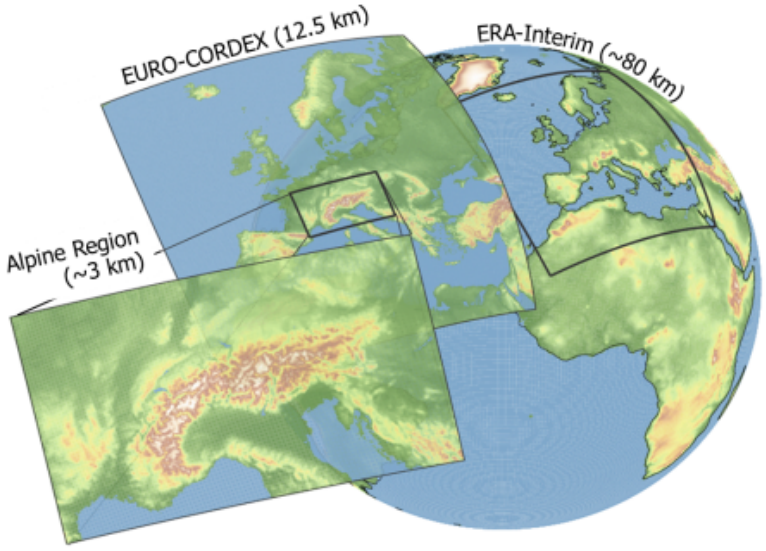

Fig. 4.1 RCM model domains on a 12.5 km grid spacing driven by ERA-Interim data. Dynamically downscaled once more to a 3 km convection permitting scale. Adopted from Prein et al. (2015).

(λ, ϕ) (longitude and latitude, respectively) and two mapping functions $a(\mu)$ and $b(\mu)$ according to

$$z(\lambda, \phi, \mu) = a(\mu) + b(\mu) \cdot h(\lambda, \phi) \ , \tag{4.1}$$

whereas the mapping functions are defined as

$$\begin{aligned} a(\mu) &= \mu \ , \\ b(\mu) &= \begin{cases} 0 & \text{if } \mu_F \leq \mu \leq \mu_T \ , \\ (\mu_f - \mu)/\mu_F & \text{if } 0 \leq \mu < \mu_f \ . \end{cases} \end{aligned} \tag{4.2}$$

μ_T and μ_F describe the models top level and the level where the horizontal layers are flat, respectively. μ takes on values from 0 (surface terrain height) to μ_T (top of the model domain) (Doms and Baldauf 2015).

Finally, the 12.5 km EURO-CORDEX simulation is dynamically downscaled to a convection permitting 3 km grid covering the greater Alpine Region resulting in a horizontal 424×240 grid which will be used throughout this work. This simulation was carried out by the Wegener Center University of Graz (WEGC) during the project Non-Hydrostatic Climate Modelling, Part II (NHCM-2) (www.nhcm-2.eu). However, this data set was regridded to the 7 km grid of the COSMO-7 grid before applying the flow analysis tool

to simplify comparison. This was done using the regridding method *polygrid* which is based on IDL code written by Mati Meron (University of Chicago) in 1991. It is a first order conservative mapping: it is only accurate up to the first order but able to conserve flux quantities (see e.g. Jones (1999)). The underlying method uses an area-weighted remapping with the interpolation weights determined by the area-overlap of the original grid cells with the target grid cells. Fig. 4.2 shows the domain used in this work after it has been regridded. This data set will be referred to simply as CCLM later on.

For more details on the CCLM simulation itself see e.g. Böhm et al. (2006).

WRF - Weather Research and Forecasting Model

The Weather Research and Forecasting Model (WRF) serves as a numerical weather prediction system designed for the mesoscale (Skamarock et al. 2008). It was a joint development by the National Center for Atmospheric Research (NCAR), the National Oceanic and Atmospheric Administration (NOAA), the Earth System Research Laboratory (ESRL) and others.

This model data was created by Klaus Görgen (Forschungszentrum Jülich) with the model version v3.3.1. Similar to the data from CCLM, the WRF data set was dynamically downscaled to 3 km by the WEGC as depicted in Fig. 4.1. Again, this data set was then regridded to the 7 km grid of the COSMO-7 grid using *polygrid*. As an example, Fig. 4.2 shows the regridded orography that outlines the exact domain of the Alpine region as being used in this work. The abbreviation WRF may be understood to refer to this regridded data set from now on.

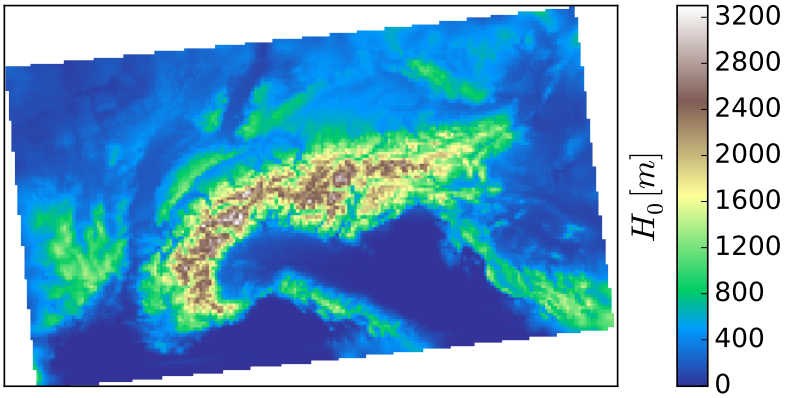

Fig. 4.2 Model orography of the Alpine region after regridding to the COSMO-7 grid (data from WRF).

A comprehensive introduction to the simulations of WRF can be found in Skamarock et al. (2008).

COSMO Model Version 7

In order to compare the flow behaviour of both WRF and CCLM with an appropriate approximation to the real state of the past atmosphere, the operational Swiss forecasting system COSMO-7 is used (Doms and Baldauf 2015). This data set covers Central and Western Europe (see Fig. 4.3) using 393×338 grid points at a 6.6 km grid spacing with 60 vertical layers. The grid structure is similar to that shown in Fig. D.1. COSMO-7 data is created up to three days in advance for short term weather forecasting purposes at a 60 s interval at the Swiss National Supercomputing Centre (MeteoSwiss 2015).

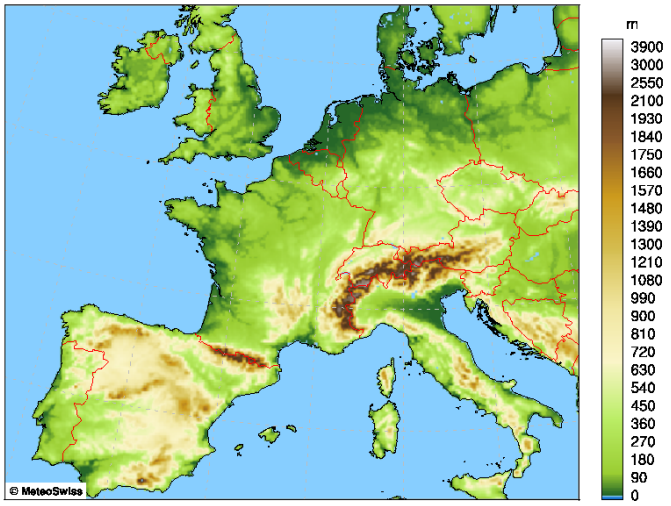

Fig. 4.3 The domain covered by the COSMO-7 forecast system. From MeteoSwiss (2015).

Its boundary conditions are provided by a global simulation of the European Centre for Medium-Range Weather Forecasts (ECMWF). Initial and boundary fields are obtained through a combination of previous model runs, observational data and climatological information. This *assimilation* process includes data from radiosondes, aircraft, weather stations and wind profiler measurements (Doms and Baldauf 2015) (see also MeteoSwiss (2015)). The data from COSMO-7 being used in this work does *not* require regridding but only the domain overlap with CCLM and WRF is considered (see Fig. 4.2).

Further information on COSMO-7 can be found at MeteoSwiss (2015) and in Doms and Baldauf (2015).

4.1.2 Selecting Cases Using Weather Typing Schemes

When studying the frequency of occurrence of the different flow categories for longer time periods, one should not expect to find interesting results. The overall flow pattern in the Alpine region can change quite frequently over the course of several weeks which means that air can move towards the Alps from very different angles during that period. This in turn implies that after the averaging process the occurrence of certain flow categories, e.g. Blocked Flow (BF), is suppressed and no interesting spatial patterns can be observed.

To get a deeper understanding of the real flow properties of certain events like foehn or barrier jets, it is necessary to find a compromise between considering only isolated events while simultaneously looking at longer time periods. This is achieved by using *weather typing schemes* that assign each day to a category of prominent weather classes that occur frequently. For example, the location of high and low pressure systems (responsible for the overall flow pattern) can help to distinguish different weather classes from each other (see e.g Lauscher (1985)). There are many different weather classification schemes available but this work uses a simple k-means cluster analysis (KMN27) with 27 clusters as provided by the software package *cost733class* (Philipp et al. 2016).

This approach includes three main steps. At first, a Gaussian time filter (with a filter length of 31 days) is applied to the input data to remove all variability that appears on longer time scales than the typical duration of weather systems (especially seasonal variability). However, the spatial patterns of the input variables are not lost during this process.

The second step utilises a principal component analysis to reduce the dimensionality of the input variables to a smaller set of variables (principal components) that still explain most of the variability of the original data set. This way, small scale variability and especially noise are removed from the data set. Finally, every day of the input time period is sorted into 27 clusters using a k-means clustering. This iterative procedure takes a starting clustering (which is usually random or can even be provided by a hierarchical clustering) and calculates the center of each cluster in the principal component space (centroids) for this clustering. Then, all days are assigned to the closest centroid regarding the euclidean distance in the principal component space. This means that several days might switch from one cluster to another. In an alternating fashion, the centroids of the new clusters are therefore calculated once more and the days are assigned again to these new centroids until no changes to the clusters are made. At this step, the final output of the k-means clustering is obtained.

For this work, ERA-Interim data from 1979 to 2010 for the Alpine region is used for this the weather typing. Anomalies in the sea level pressure (location of high and low pressure systems), convective available potential energy (CAPE), wind fields at 700 hPa as well as the geopotential at 500 hPa are used. Two of the obtained weather classes, a *Südstau* and a *Nordstau* type (referred to as weather class 3 and 14, respectively) are

investigated concerning their flow behaviour in section 4.3.2.

However, the method of using this separation by weather types is only an approximative procedure since the ERA-Interim data set used to derive the weather types in the first place is only closely tied to the COSMO-7 data set. Kida et al. (1991) showed that when local area models are coupled to a Global Climate Model (GCM) only at the lateral boundaries, the two models tend to separate when integrated over long time periods. Since both WRF and CCLM are only driven by ERA-Interim data at the boundaries of the European domain, their internal dynamics may lead to different situations in the Alpine region at any given point in time. This especially includes the timing of events such as when a cold front hits the Alps or the direction of impinging air flow. Therefore, these results need to be interpreted with caution.

4.2 Properties of the Flow Analysis Tool

This section provides detailed results generated by the flow analysis tool for the period of November 2002. A case study approach examines the effects of different free parameters within the algorithm and how different atmospheric variables and conditions manifest themselves in the flow categories. The vertical and temporal resolutions of the flow categories is also shown for a special event. To establish a comparable environment, all results have been generated using the following setup of parameters (unless otherwise specified):

- The barrier height was calculated using the cone search method using 72 search directions with a half-cone opening angle of 5° with unlimited search range.
- For time efficient calculations of the barrier height, the pre-calculated maximum mountain height map (MMHM) was used.
- All data sets have been regridded to the 7 km grid of the COSMO-7 data set and only the domain overlap between WRF, CCLM and COSMO-7 is displayed.
- Detection height was set to 1500 m above sea level (asl).
- The Froude number threshold to separate BF and Flow Above (FA) categories was set to $F_{thresh} = 1.0$.
- The relative humidity threshold to separate the use of virtual and equivalent potential temperature was set to $RH_{thresh} = 90\%$.

4.2.1 Influence of Different Parameters

First of all, the different methods to calculate the maximum barrier height h are investigated. All of the following calculations use data from WRF of 30 November 2002 at 2200 Coordinated Universal Time (UTC). Fig. 4.4 shows the synoptic situation in Europe at this point in time including the pressure field and weather fronts. Due to the low pressure cell west of the British Isles, air is approaching the Alps from a northwestern direction carrying a small warm front with it. The detection height for the following calculations is set to 1500 m above sea level as stated previously. All results for the flow categories are compared to Fig. 4.7b since this is the parameter setting that will be used later.

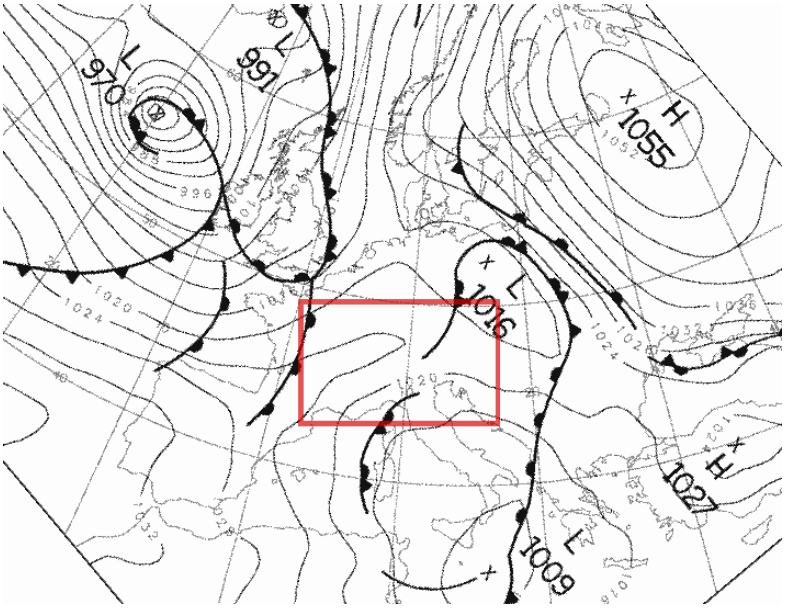

Fig. 4.4 The synoptic situation in Europe two hours after the time of interest for this section (1 December 2002 at 0000 UTC). Pressure is denoted as contour lines and fronts are shown as bold lines (triangles: cold fronts, semicircles: warm fronts). The red rectangle approximately indicates the domain of the Alpine region as used in the following. Adopted from www.wetterzentrale.de.

SLM

As a starting point, Fig. 4.5a shows the maximum barrier height values h using the straight line method (as explained in section 3.2.1). This means that h is evaluated for each grid cell in a straight line within the program without using any pre-calculated maximum mountain height maps. Therefore, no free parameters are introduced but the computation takes relatively long. Fig. 4.5b shows the corresponding flow categories for comparison with other methods. From this figure it can be seen that (especially northwest of the Alps) BF and FA are subject to intense noise.

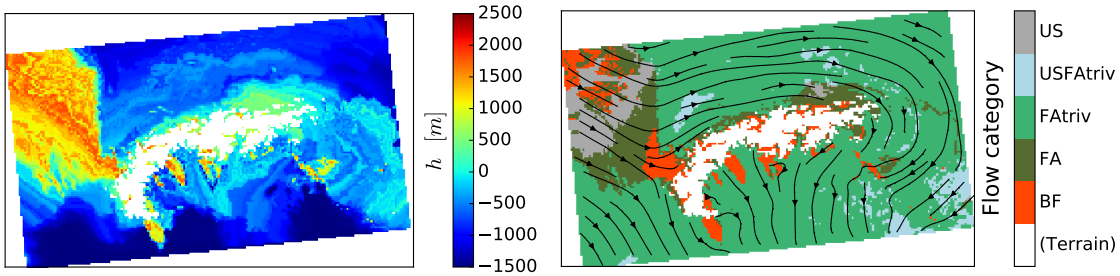

(a) Maximum obstacle height. (b) Flow categories.

Fig. 4.5 Maximum obstacle height and flow categories calculated using SLM.

MMHM for SLM

The more time efficient use of a pre-calculated maximum mountain height map (MMHM) (see section 3.2.3) for the Straight Line Method (SLM) produces different h fields as shown in Fig. 4.6b (with corresponding flow categories in Fig. 4.6b). It can be seen that there is less noise in the flow categories but the overall features stay the same. This highlights that the MMHM interpolation approach does indeed produce meaningful results while reducing the computation time immensely.

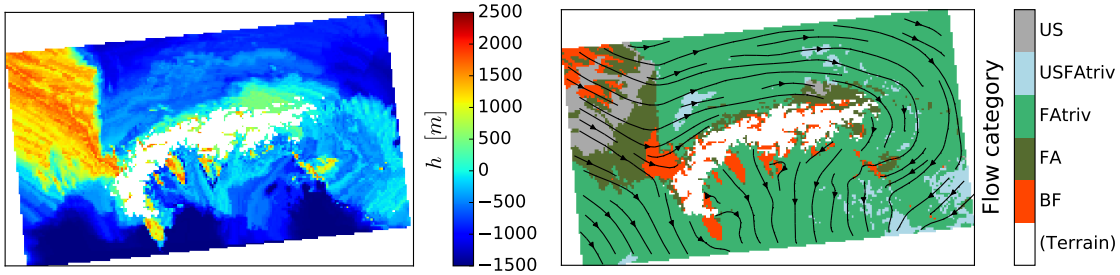

(a) Maximum obstacle height. (b) Flow categories.

Fig. 4.6 Maximum obstacle height and flow categories calculated using MMHM for SLM.

MMHM for CSM

The more robust method of using MMHM with the Cone Search Method (CSM) (section 3.2.2) is shown in Fig. 4.7a and Fig. 4.7b (h and flow categories, respectively). A half cone opening angle of 5° is used. This method and parameter setting acts as a default setting for all further calculations of the later sections. From Fig. 4.7b it can be seen that the flow categories are smoothed even further, resulting in less noise than in Fig. 4.6b. However, most of the noise between BF and FA was assigned to BF due to the overall increase in the maximum obstacle height values.

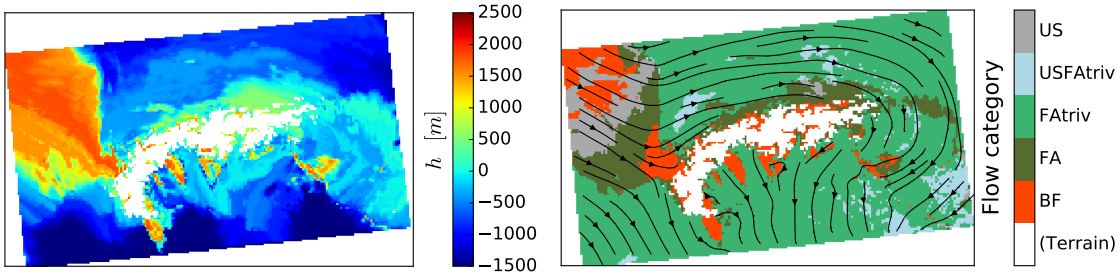

(a) Maximum obstacle height. (b) Flow categories.

Fig. 4.7 Maximum obstacle height and flow categories calculated using MMHM for Cone Search Method (CSM) with a half cone opening angle of 5°.

As an additional comparison, Fig. 4.8 shows results using a different half cone opening angle of 10°. Note that the h field does hardly change between the two methods. However, h values are in general slightly larger compared to using a smaller cone opening angle. The resulting flow categories are nearly indistinguishable from Fig. 4.7b. This shows that the results are not sensitive to a small change of the cone opening angle.

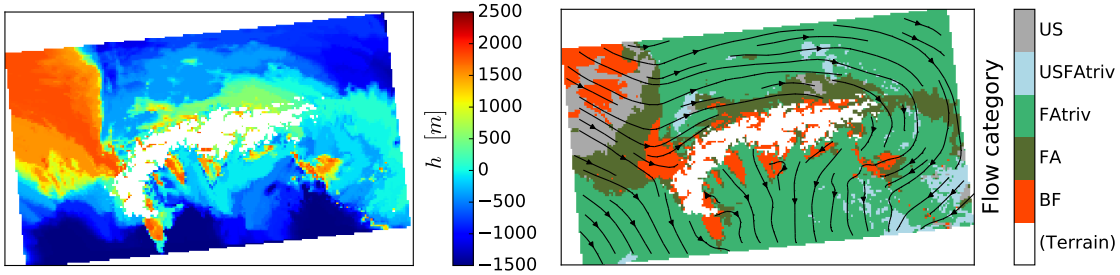

(a) Maximum obstacle height. (b) Flow categories.

Fig. 4.8 Maximum obstacle height and flow categories calculated using MMHM for CSM with a half cone opening angle of 10°.

Results using the method of appendix B are *not* shown here since the domain under consideration is too small for meaningful parameters for this method.

Different Threshold Values

Finally, different values for the relative humidity threshold, $RH_{thresh} = 0.8$ instead of 0.9, and the Froude number threshold, $F_{tresh} = 2.0$ instead of 1.0, are shown in Fig. 4.9a and Fig. 4.9b, respectively. This relative humidity threshold is already outside of the 0.85 to 0.95 interval that was proposed by Hughes et al. (2008). Nevertheless, the flow analysis tool shows stable performance even for this out-of-bounds value. It may be recalled that the relative humidity threshold separates the use of the virtual potential temperature (for air parcels below the threshold value) from the use of the equivalent potential temperature while the Froude number threshold separates BF from FA situations. It can be seen that changing RH_{thresh} affects the regions of unstable air slightly while a larger F_{thresh} converts some of the FA regions to BF as expected.

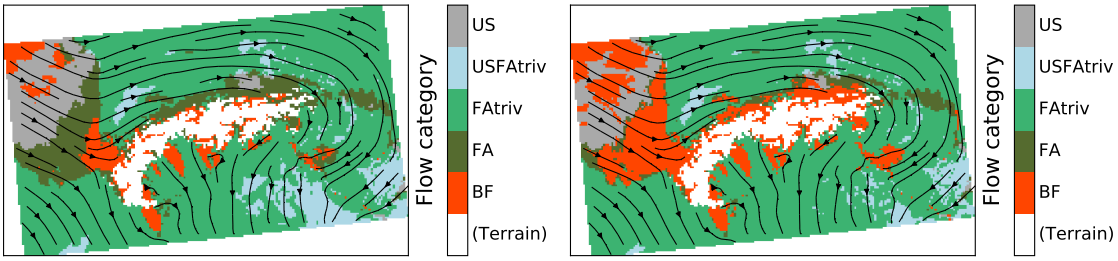

(a) $RH_{thresh} = 0.8$. (b) $F_{thresh} = 2.0$.

Fig. 4.9 Flow categories for changed relative humidity and Froude number thresholds.

4.2.2 Influence of Atmospheric Variables on Flow Categories

To show the impact of the different atmospheric variables on the results of the flow analysis tool, one special event (30 November 2002 at 2200 UTC) is examined in detail in the following, using data from WRF as seen in Fig. 4.10.

Fig. 4.10a shows that air with more than 15 m s^{-1} is approaching the Alps from northwest, part of which is being labelled as BF and FA by the flow analysis tool (Fig. 4.10h). It can be seen that high wind speeds do not automatically lead to a categorisation of FA. It is apparent that all areas labelled as Trivial Flow Above (FAtriv) and Unstably Stratified Air with Trivial Flow Above (USFAtriv) possess negative maximum obstacle height h (Fig. 4.10b). However, while high values for h seem to be a fundamental requirement for the BF category, they are not sufficient enough on their own. Fig. 4.10f shows that the Brunt-Väisälä frequency is strongly influenced by relative humidity values especially in areas where RH is fluctuating around the threshold value ($RH_{tresh} = 90\%$), as seen in Fig. 4.10e. In some areas, these artificial features are responsible for a separation between BF and Unstably Stratified Air (US). This highlights that the relative humidity and especially the corresponding threshold value both have an enormous impact on the

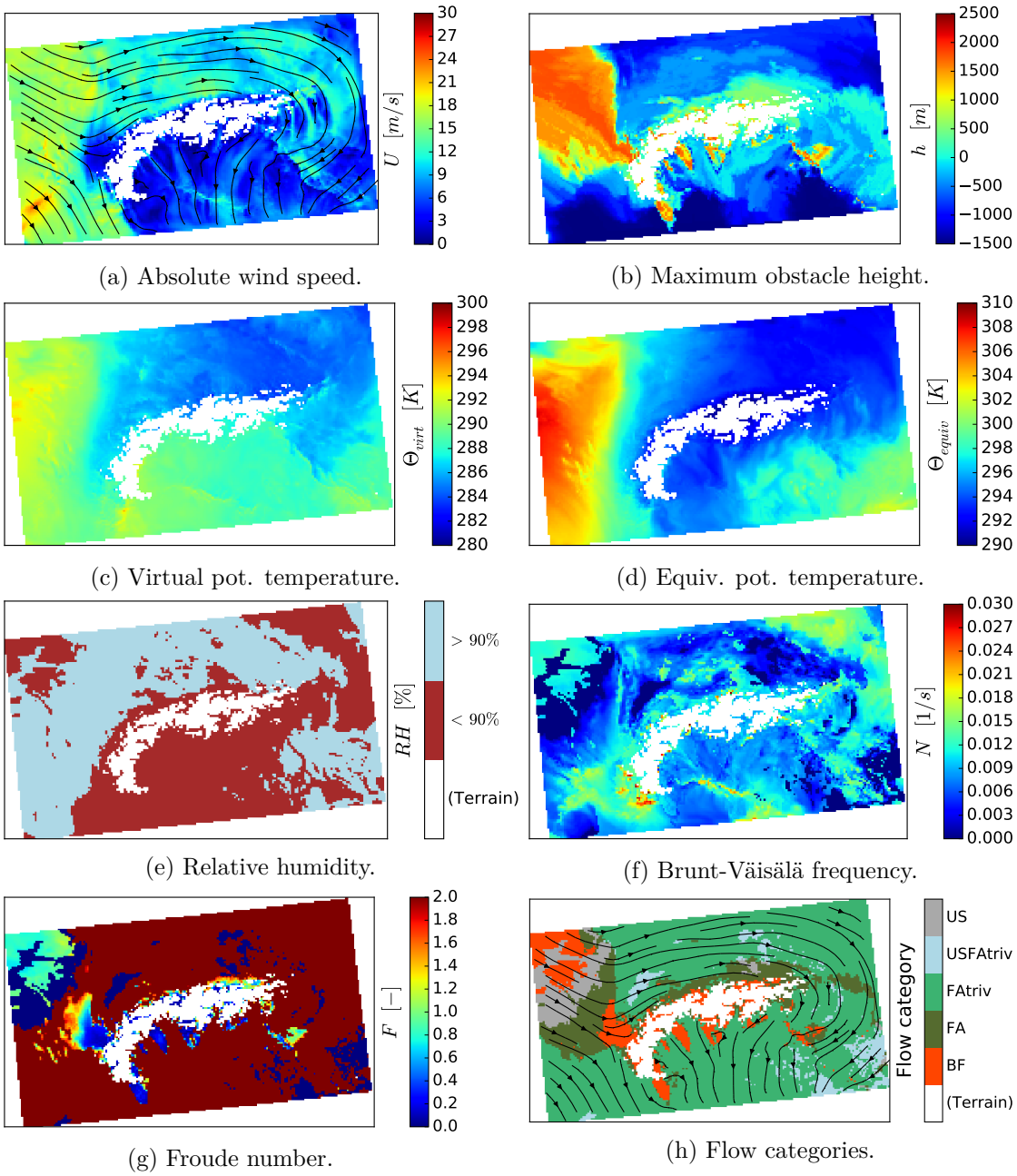

(a) Absolute wind speed.

(b) Maximum obstacle height.

(c) Virtual pot. temperature.

(d) Equiv. pot. temperature.

(e) Relative humidity.

(f) Brunt-Väisälä frequency.

(g) Froude number.

(h) Flow categories.

Fig. 4.10 Input variables and computed fields for 30 November 2002 at 2200 UTC from WRF at 1500m above sea level. Streamlines depict airflow. Relative humidity (e) is separated into above and below the threshold (90%), revealing its influence on the Brunt-Väisälä frequency (f). Imaginary values for N in (f) are set to $N = 0$. Froude number values (g) are capped at 2.0; values of $F = 0$ indicate unstable stratification. Flow categories (h) combine the information of the Froude number and stability.

results. The small areas of BF embedded in FAtriv directly south of the Alps are a result of non-uniform wind directions in these areas.

4.2.3 Vertical Distribution of Flow Categories

Fig. 4.11 shows the vertical distribution of flow categories for the same event as discussed in the previous section. It may be noted that the wind direction, being most important for the flow categories, changes quickly with respect to height at low altitudes, hence leading to a completely different distribution of BF and FA at different elevations. Throughout the figures, it becomes apparent that whenever BF air parcels get close to the mountain that they are approaching, the wind direction changes right in front of the barrier.

As seen in Fig. 4.11g, most of the air approaching from northwest is being labelled as FA while all of the stream lines directly move towards the mountains with only minimal wind direction change. The same effect can be seen in all figures showing data below 900 m over Hungary and Croatia where air is approaching the Adriatic Sea.

As expected, FAtriv and USFAtriv completely dominate the spectrum of flow categories with increasing height. On the other hand, Fig. 4.10c shows how local turbulence in the wind direction leads to alternation between FA and BF south of the Alps.

To study the vertical distribution of flow categories from a different point of view, Fig. 4.12 shows a vertical cut through the domain between the two points A and B that are chosen such that the impinging air is mostly parallel to the vertical plane created this way (Fig. 4.11e). It can be seen how some of the lower lying air directly in front of the main barrier (located at ~ 380 km between A and B) is identified as BF while air higher up and farther upstream is separated into FA and US.

Note that the horizontal wind direction below 1000 m is no longer aligned with the vertical plane used in Fig. 4.11 which is the reason for the appearance of FA and FAtriv below BF air parcels. In Fig. 4.13 it can be seen how the wind component parallel to the line from A to B is high in the FA regions of Fig. 4.12 and drops drastically in the BF regions right before the mountain. Fig. 4.12 also shows how the valley at ~ 550 km between A and B contains mostly BF air that seems to be trapped between the surrounding mountains.

Since the line from A to B directly cuts through the stagnation point of the impinging flow, these air parcels slow down right in front of the mountain and tend to move to the sides. Stull (1988) explains how this stagnant air (if trapped in front of the mountain) together with the mountain itself form a larger, more streamlined obstacle which needs to be surpassed by other impinging air parcels. This situation is illustrated in Fig. 4.14. However, this idealised example does not exactly resemble the situation of Fig. 4.12 because the air labelled as BF is not stuck in front of the mountain but rather tends to flow around the barrier to follow the stream pattern that is present at that time. Since the air labelled as FA also needs to follow this stream pattern, these air parcels do not

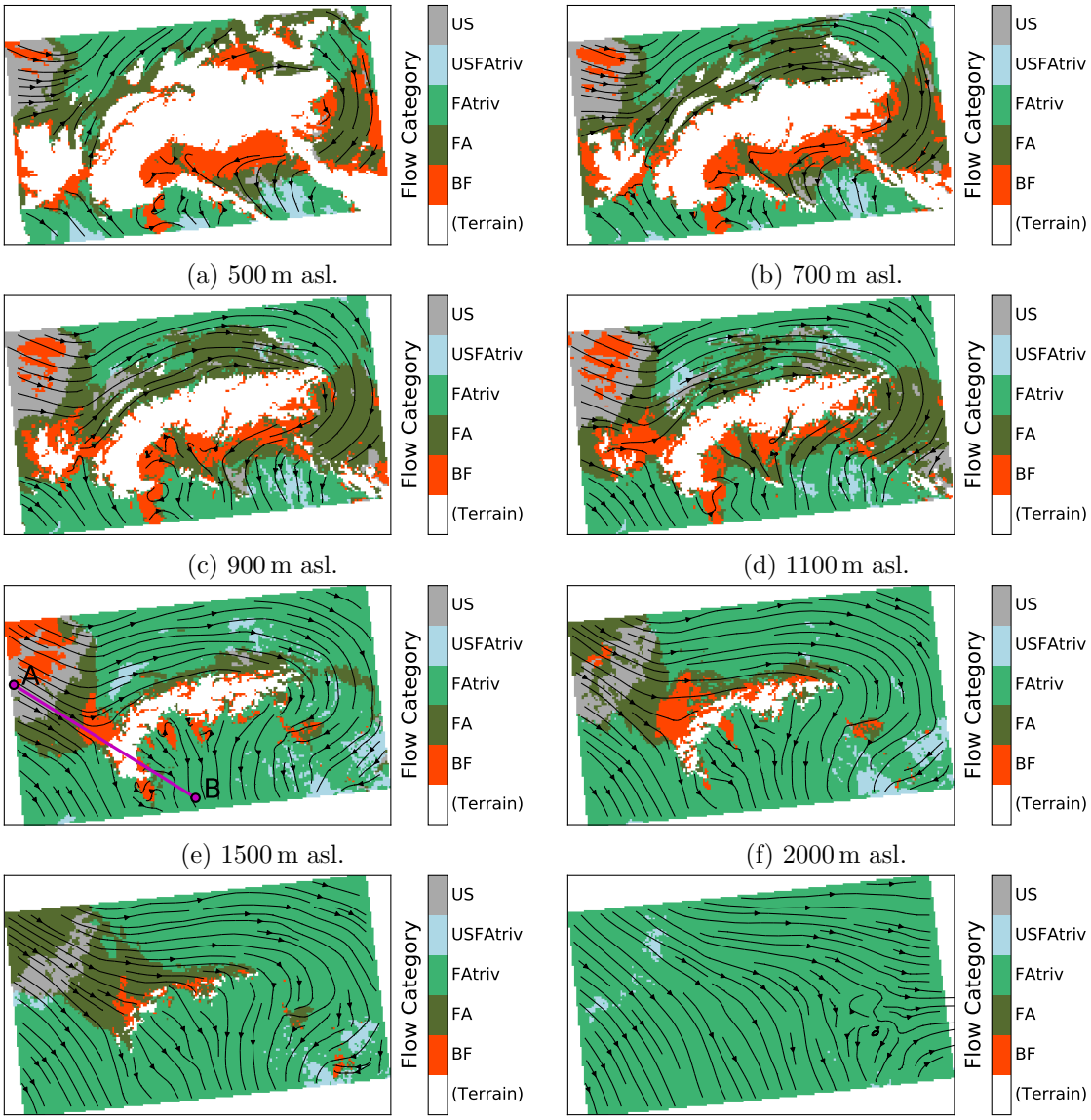

(a) 500 m asl. (b) 700 m asl.

(c) 900 m asl. (d) 1100 m asl.

(e) 1500 m asl. (f) 2000 m asl.

(g) 2500 m asl. (h) 3500 m asl.

Fig. 4.11 Vertical distribution of flow categories for 30 November 2002 at 2200 UTC for different heights above sea level (asl) with data from WRF; streamlines depict airflow. The purple line in (e) shows the vertical domain cut used for Fig. 4.12. Note that the detection height does not increase linearly between the images.

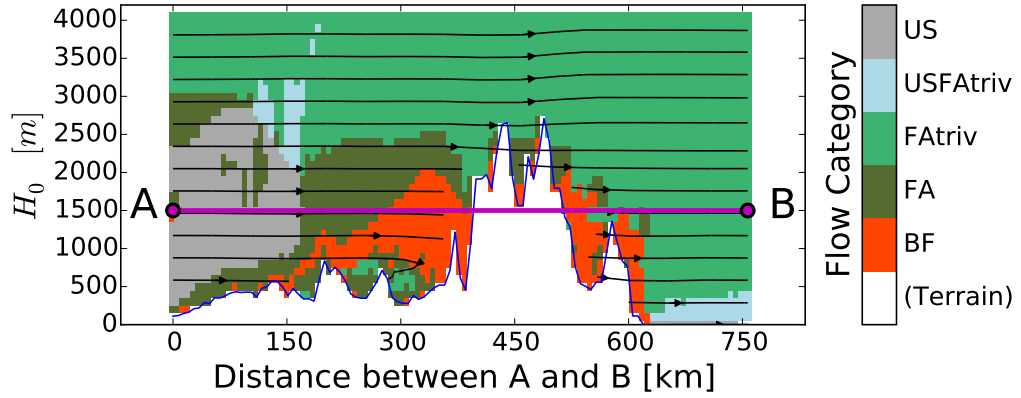

Fig. 4.12 Vertical cut through the domain as indicated by the purple line in Fig. 4.11e for 30 November 2002 at 2200 UTC; data from WRF. The situation is similar to that of Fig. 3.4. Streamlines depict airflow parallel to the direction from point A to B.

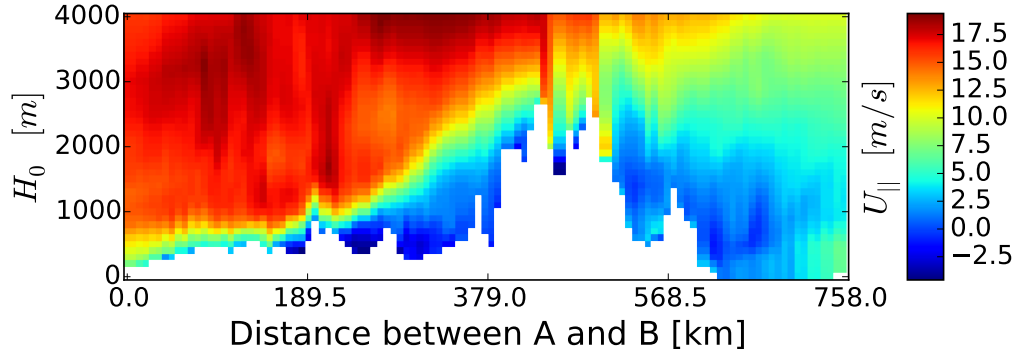

Fig. 4.13 Wind profile for the wind component parallel to the cut through the domain corresponding to Fig. 4.12. Positive values indicate wind from left to right.

show vertical motion because although they possess enough kinetic energy to surmount the barrier, they are likely to also flow around the mountains.

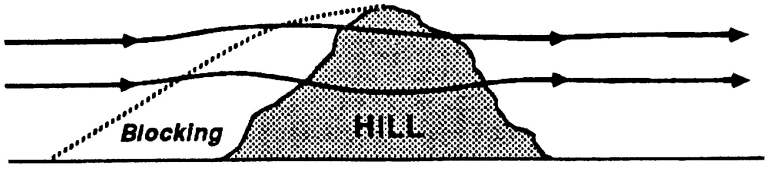

Fig. 4.14 Schematic illustration of stagnant flow for low Froude number (see also Fig. 2.2). Mountain and blocked air together form a combined obstacle that is more streamlined than the mountain on its own. This is similar to Fig. 4.12. Adopted from Stull (1988).

4.2.4 Time Evolution of Flow Categories

Fig. 4.15 shows the change of flow categories during a single day (30 November 2002) together with wind speeds. The development of a stagnation point on the northeastern flank of the Alps (around Geneva) can be identified trough the appearance of BF together with reduced wind speeds. This development peaks at 2100 UTC (Fig. 4.16d). Although the direction and speed of the impinging air flow stays relatively the same during this day, the calculated flow categories change rather vividly. Especially the mixture and transition between FA and BF far upstream of the Alps can be observed. This is presumably a response of the flow analysis tool to subtle changes in the wind direction when the impinging air is at a critical level of Froude numbers at around unity. However, this may also be interpreted as a Froude number threshold that is too small to produce stable results.

The wind speed plots of Fig. 4.16c and Fig. 4.16d show how a large air mass with higher wind speeds than its surrounding is approaching the Alps from a northwestern direction. This directly translates to the appearance of FA in the flow category plots of these figures. However, some areas of this high velocity air mass are labelled as US or BF, indicating a change in stability in this region.

4.3 Comparing Different Data Sets

In order to be able to compare different data sets (or time periods) this section shows how to use the frequency of occurrence for the different flow categories and outlines how this method can be used for model evaluation purposes.

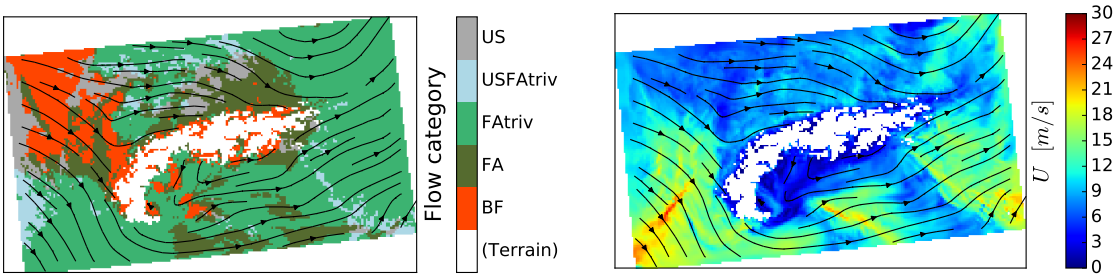

(a) 0000 UTC.

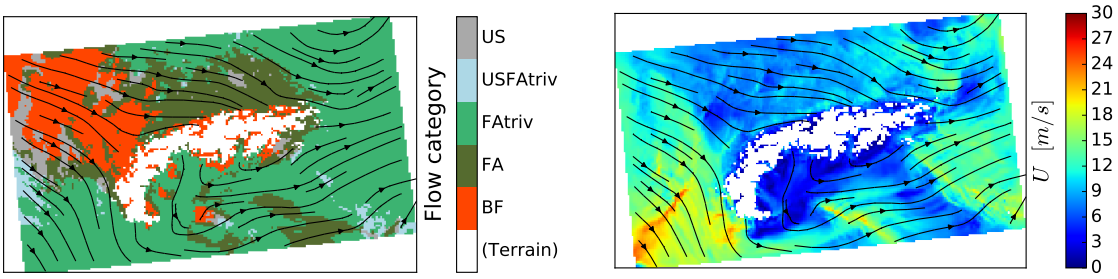

(b) 0300 UTC.

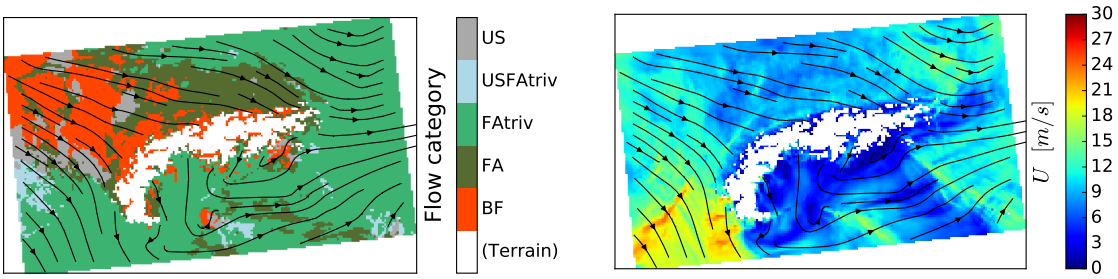

(c) 0600 UTC.

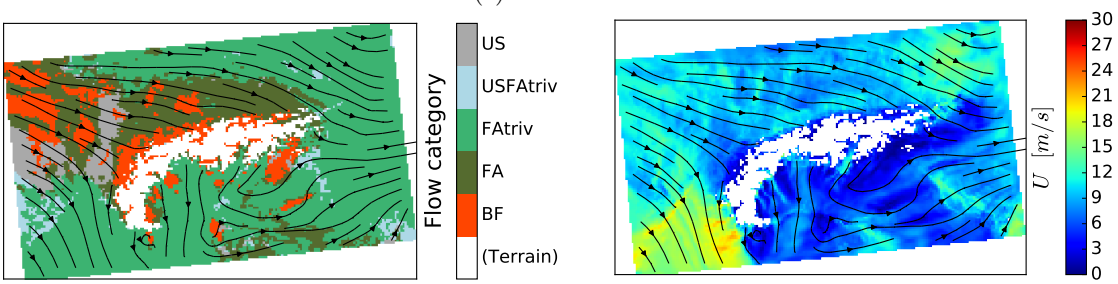

(d) 0900 UTC.

Fig. 4.15 Flow categories (left column) and absolute wind speed (right column) for 30 November 2002 in 1500 m asl. Data from WRF. Stream lines depict airflow.

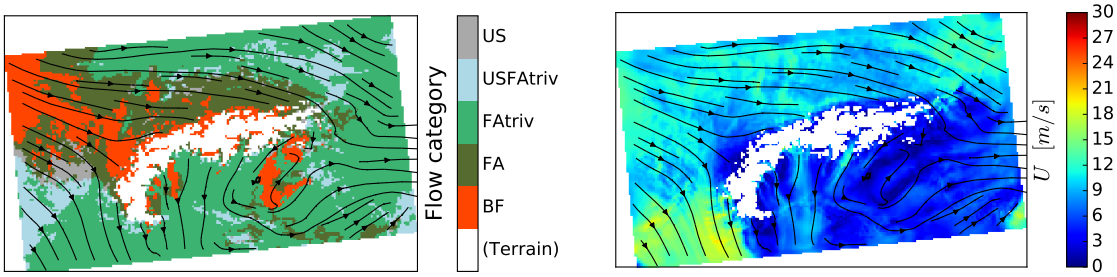

(a) 1200 UTC.

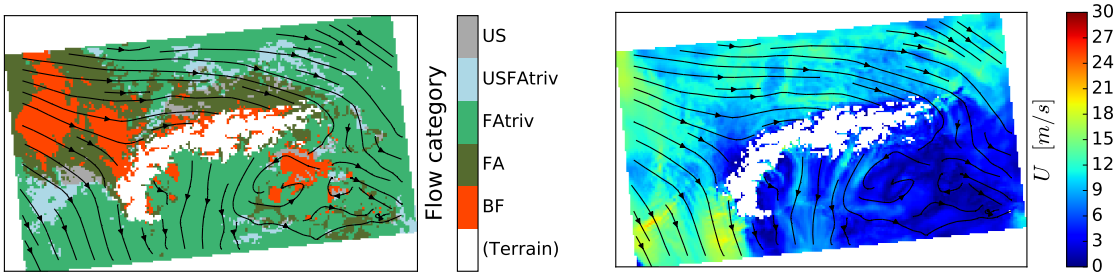

(b) 1500 UTC.

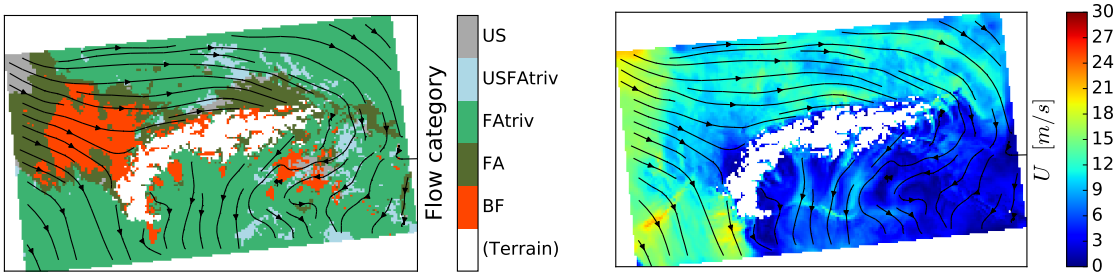

(c) 1800 UTC.

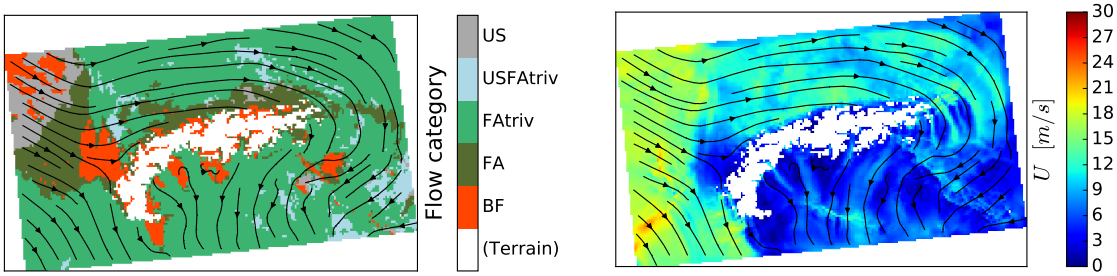

(d) 2100 UTC.

Fig. 4.16 Continuation of Fig. 4.15.

4.3.1 Frequency of Occurrence for Flow Categories

An event based comparison for data sets that are driven by boundary conditions that are far way from the domain under consideration is likely to show only climate variability effects. It is therefore more constructive to look at the frequency of occurrence for the different flow categories over a longer time period. In this case, all 30 days of November 2002 with data on an hourly basis are considered.

As can be seen in Fig. 4.17, FAtriv is the dominant flow category, especially in regions far away from the Alps, which is to be expected since the detection height of 1500 m is already higher than any mountains if air flow is not directly towards the Alps. However, BF becomes more dominant in the close vicinity of the mountain ridge but hardly ever exceeds 40% occurrence in other regions. The low frequency of occurrence of both US and USFAtriv indicates the overall stable stratification of air during this period.

Fig. 4.17f shows the frequency of occurrence for the combination of all flow-above categories (FA, FAtriv and USFAtriv) thus providing a more comprehensive counterpart to the BF category (Fig. 4.17a).

The cause of the *artificial stripes* that can be seen in Fig. 4.17b (FA) and 4.17c (FAtriv) is the use of the MMHM method to approximate the barrier height as discussed in section 3.2.3 and the reasons will be explained in the following. First, it is important to note that these stripes all originate at isolated mountain peaks that cut through the detection surface as highlighted by Fig. 4.18. Also, all stripes show an angular spacing of about 5° which is the same as the angular resolution of the underlying MMHM (using 72 search directions). This is one of the downsides of using the MMHM instead of calculating every barrier height explicitly. However, these stripes persist even when the number of search directions in the MMHM is increased. Appendix B introduces a possible solution to this problem.

4.3.2 Differences between WRF, CCLM and COSMO-7

This section provides the results generated by the flow analysis tool and shows the differences between them when using data from WRF and CCLM in comparison to data from COSMO-7 for November 2002. In general, the monthly averaged frequency of occurrence results for all data sets look roughly the same (not shown). The reason being that the many different synoptic situations of this period are mixed up together in one image, thus hiding potential systematic differences. Therefore, all days of November 2002 are separated into different weather classes as discussed in section 4.1.2. Two of these weather classes and their corresponding frequency of occurrence of flow categories are examined in the following. It may be noted that for both weather classes (a *Südstau* and a *Nordstau* type) the detection height is set to 1500 m above sea level. However, this detection height might be adopted to better fit the atmospheric situation that is currently under consideration. From an algorithmic point of view, this would imply that

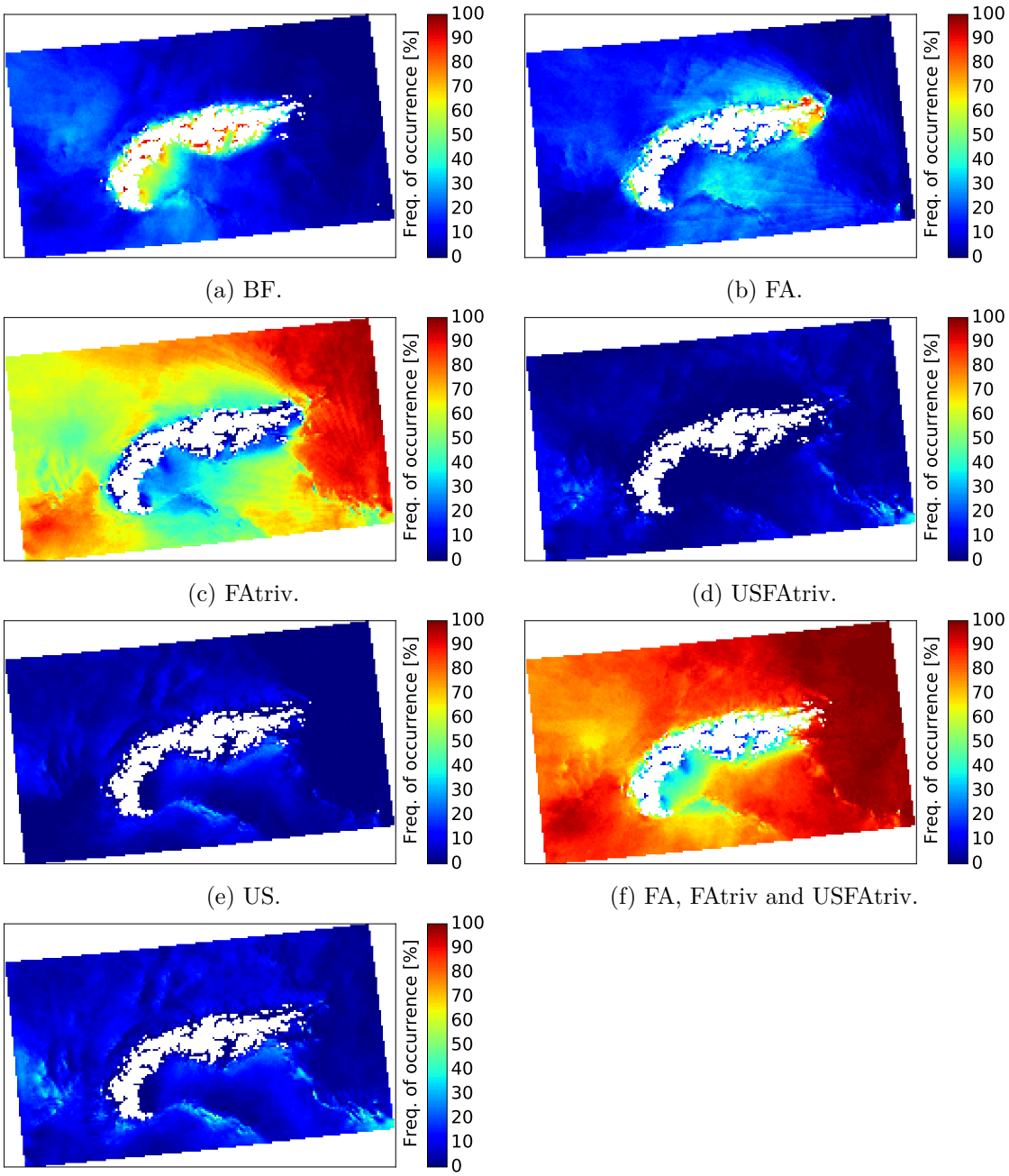

(a) BF.

(b) FA.

(c) FAtriv.

(d) USFAtriv.

(e) US.

(f) FA, FAtriv and USFAtriv.

(g) US and USFATriv.

Fig. 4.17 Frequency of occurrence for the different flow categories for November 2002 using data from WRF on an hourly basis. Detection height is 1500 m. The *stripes* in (b) and (c) are discussed in the text. Combined categories: (f) all categories with flow-above (FA, FAtriv, USFAtriv); (g) all categories with unstable stratification (US, USFAtriv).

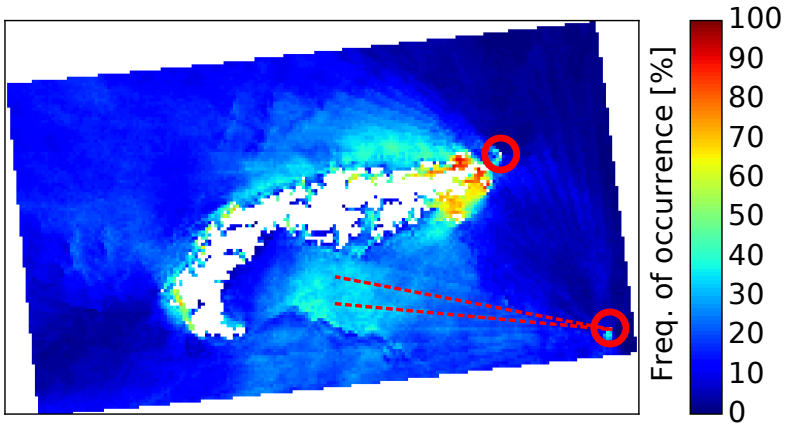

Fig. 4.18 The artificial stripes of Fig. 4.17b examined in detail. Red circles: isolated mountain peaks are the source of all stripes. Dashed lines indicate that the stripes are fanned out with a 5° angle between them.

the detection height is allowed to depend on the synoptic situation. This dependence is not to be discussed in this work.

Südstau: Weather Class 3 of KMN27

The first weather class of the KMN27 weather typing scheme that is to be discussed in this section is a *Südstau* type (weather class 3, see Fig. 4.19) which is characterised by a low pressure system over the British Isles as seen in Fig. 4.19. Therefore, air moves from the Atlantic over the Iberian Peninsula towards the Mediterranean Sea and turns north to encounter the Alps from a southwestern direction where precipitation is likely to occur. This situation is rarely observed during the summer months but can appear during the rest of the year.

Two different events of November 2002 are categorised with this weather class that make up a total of 8 days, the first lasting from 12 to 14 November and the second from 21 to 25 November. Fig. 4.20 shows the frequency of occurrence for all flow categories using data from COSMO-7. It can be seen how BF only occurs in the western part of the Po Valley where air masses are trapped only in a narrow streak at the southern flank of the Alps. Additionally, Fig. 4.20b shows that FA occurs south of the Alps peaking at around 50% occurrence in some areas. Unstable air is rather rare (Fig. 4.20g), except for localised areas over the Dinaric Alps in Croatia and the Northern Apennines in Italy.

Fig. 4.21 shows the absolute difference in the frequency of occurrence between data from WRF and COSMO-7 for this weather type. Deviations are in general fairly small, despite the fact that the period under consideration is still quite short. However, FA is

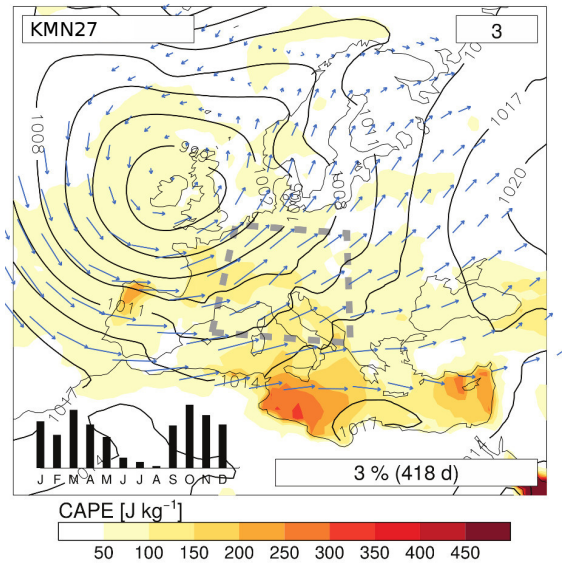

Fig. 4.19 Illustration of the KMN27 weather class 3. Blue arrows depict air flow; black lines denote pressure; convective available potential energy (CAPE) shown in colour. The histogram in the bottom left corner denotes the relative annual frequency of this weather class. Adopted from current work at the WEGC.

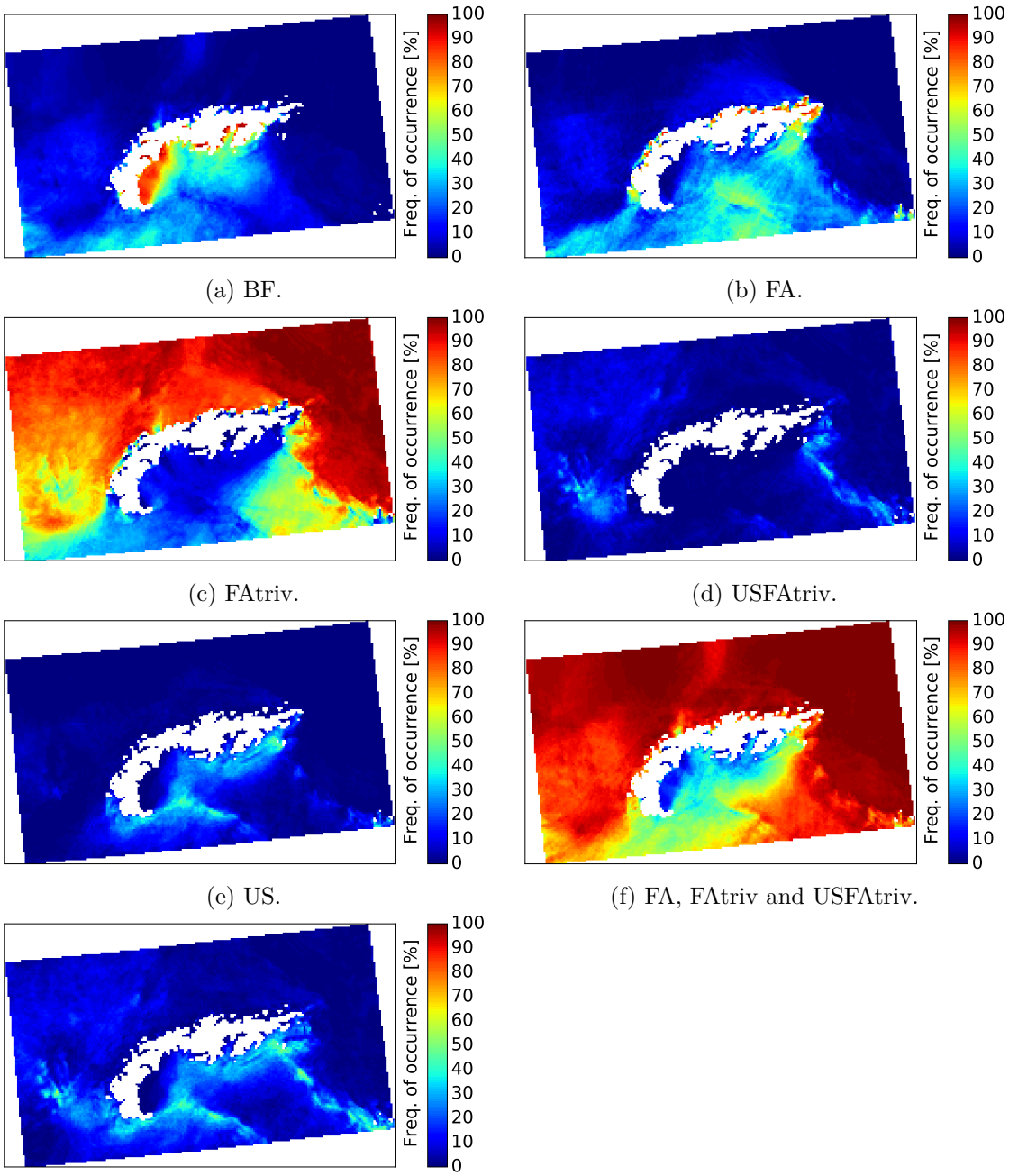

(a) BF.

(b) FA.

(c) FAtriv.

(d) USFAtriv.

(e) US.

(f) FA, FAtriv and USFAtriv.

(g) US and USFATriv.

Fig. 4.20 Frequency of occurrence for the different flow categories for November 2002 using data from COSMO-7 on an hourly basis for the 8 days of the KMN27 weather class 3. Detection height is 1500 m. Combined categories: (f) all categories with flow-above (FA, FAtriv, USFAtriv); (g) all categories with unstable stratification (US, USFAtriv).

overestimated south of the Alps at the cost of BF. This means that air in WRF is more likely to move over the Alps (rather then being blocked) as compared to COSMO-7. Additionally, the occurrence of unstable air (Fig. 4.21g) changes quite drastically south of the Alps between over- and underestimation. Especially the mountainous regions of the Northern Apennines in Italy and the Massif Central in France tend to induce more instability in WRF. The underestimation of FAtriv in Fig. 4.21c west of the Alps indicate a deviation in wind direction between WRF and COSMO-7.

Fig. 4.22 shows the same as Fig. 4.21 but this time comparing CCLM and COSMO-7. It can be seen that the deviations in BF are more localised, especially the underestimation in the Po Valley and the overestimation south of the Massif Central. Furthermore, a confined area of heavy overestimation of unstable air around the southwestern flank of the Alps can be identified (Fig. 4.22g), indicating that terrain induced instability is over-represented in CCLM. Note that this is not the case in WRF (see Fig. 4.21g).

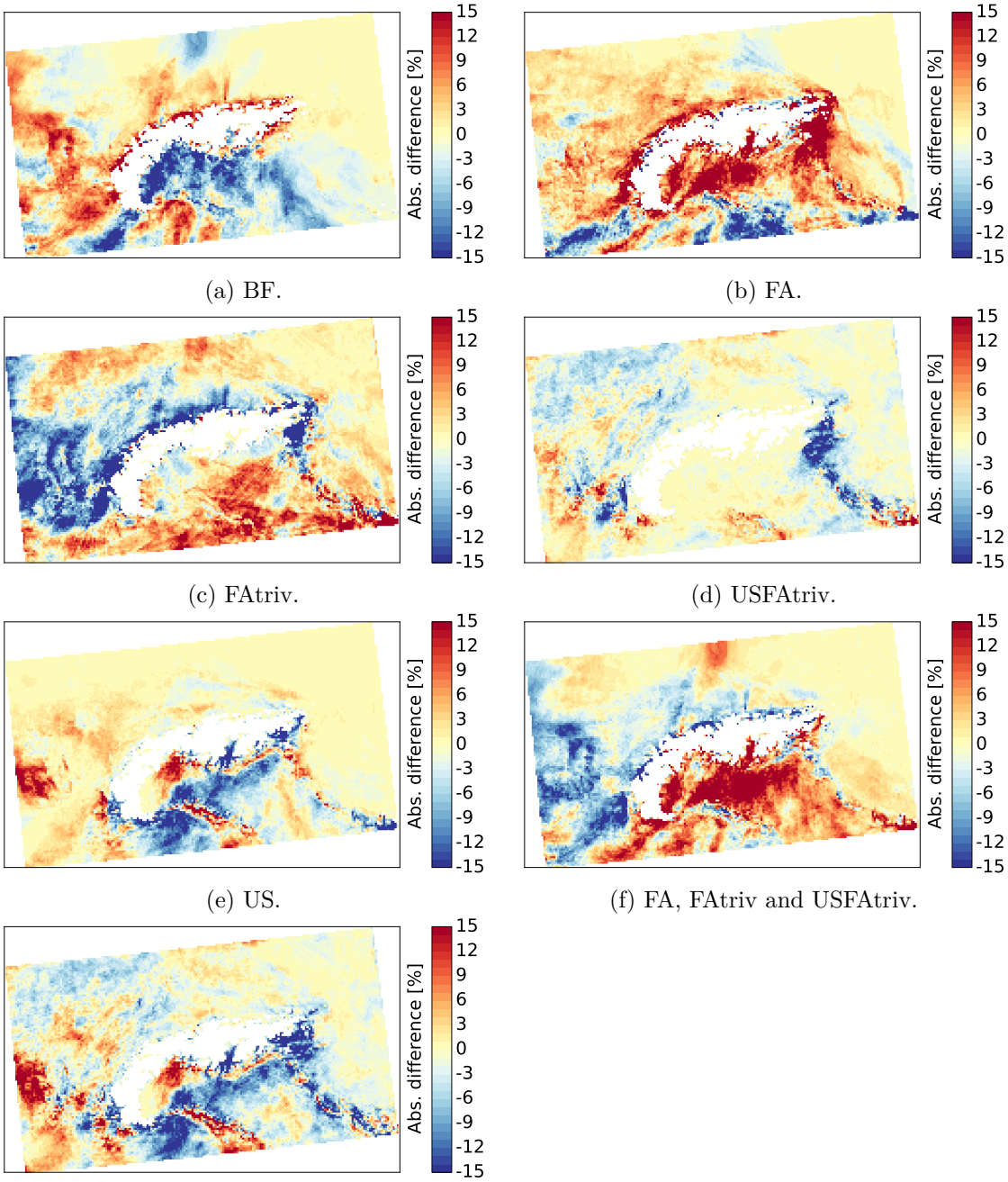

(a) BF.

(b) FA.

(c) FAtriv.

(d) USFAtriv.

(e) US.

(f) FA, FAtriv and USFAtriv.

(g) US and USFATriv.

Fig. 4.21 Absolute difference between the frequency of occurrence for different flow categories between WRF and COSMO-7 (see Fig. 4.20 for details).

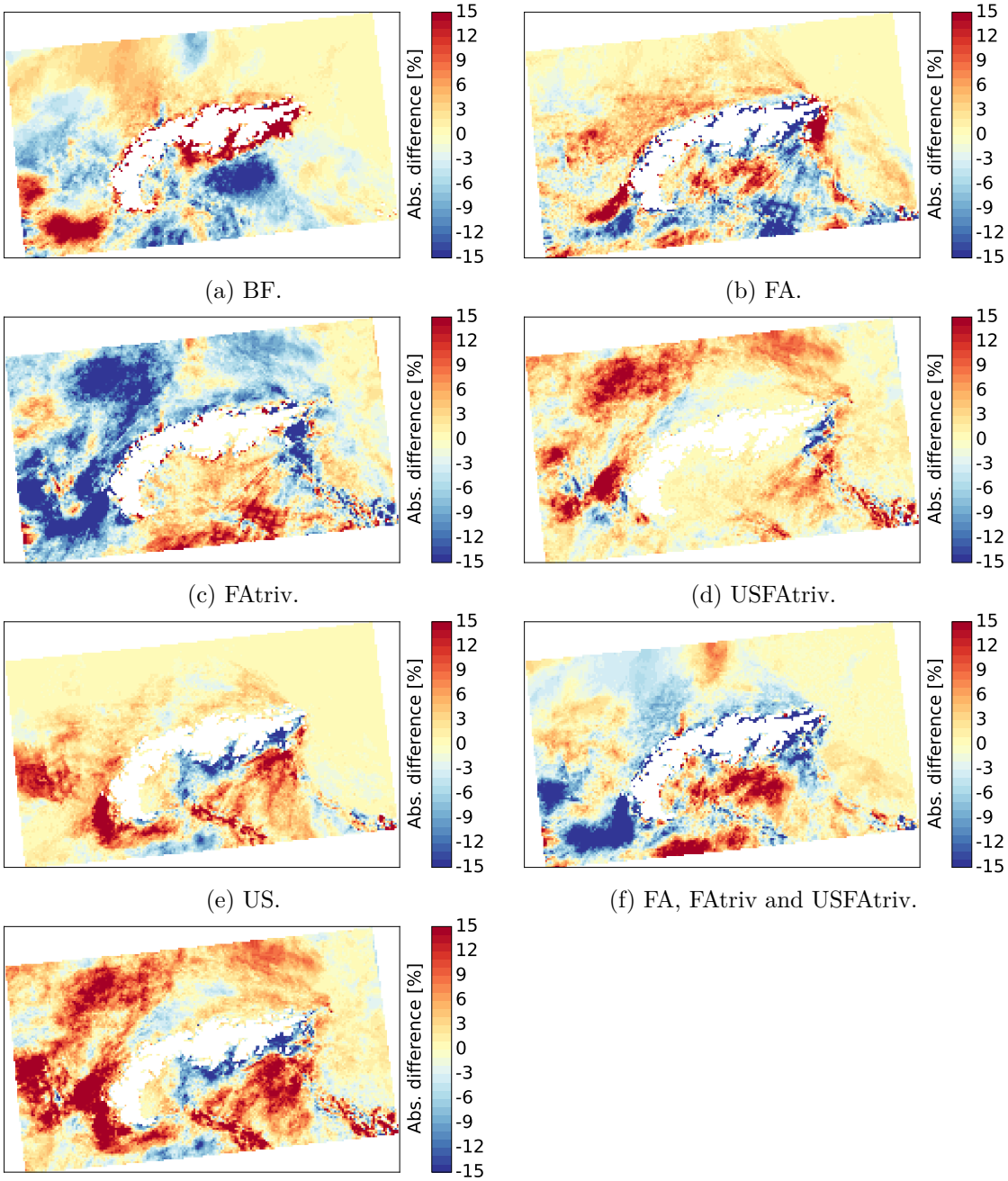

(a) BF.

(b) FA.

(c) FAtriv.

(d) USFAtriv.

(e) US.

(f) FA, FAtriv and USFAtriv.

(g) US and USFATriv.

Fig. 4.22 As Fig. 4.21 but comparing CCLM with COSMO-7 (see Fig. 4.20 for details).

Nordstau: Weather Class 14 of KMN27

The second weather class of the KMN27 weather typing scheme to be examined in more detail is a *Nordstau* type (weather class 14, see Fig. 4.23). This class appears almost exclusively in the colder half of the year, with nearly no occurrence between April and October. It is characterised by a low pressure cell northwest of Scandinavia that extends to the Baltic Sea, together with a high pressure cell west of and over the Iberian Peninsula. This forces air masses from the Atlantic over the British Islands to the Alps from a northwestern direction. In this situation, precipitation occurs mainly on the northern flank of the Alps.

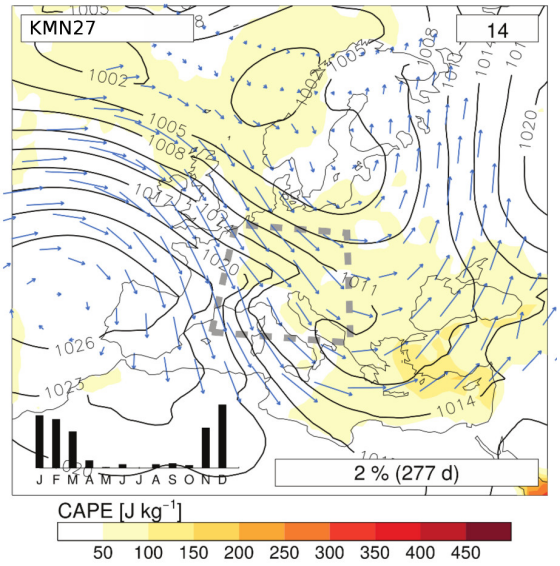

Fig. 4.23 Illustration of the KMN27 weather class 14. Blue arrows depict air flow; black lines denote pressure; CAPE shown in colour. The histogram in the bottom left corner denotes the relative annual frequency of this weather class. Adopted from current work at the WEGC.

All days between 4 and 9 November 2002 have been categorised with this weather class, according to the KMN27 weather typing scheme. Fig. 4.24 shows the frequency of occurrence for all flow categories for this period using data from COSMO-7 as a reference. It can be seen that a significant part of the domain, located northwest of the Alps, shows a BF occurrence of about 40%. While FA is naturally less prominent in this area, it becomes more prominent east and west of this region where air is able to move over the lower outskirts of the Alps. Since air is approaching from northwest, Fig. 4.24c and Fig. 4.24f resemble what can be considered a *reversed wind shadow* created by the Alps,

with low values indicating blocked air. The presence of air with unstable stratification is rather weak, except over the summits of the Massif Central in France that can reach up to the detection height of 1500 m.

In Fig. 4.25, the results from WRF and COSMO-7 are compared. The large red areas in Fig. 4.25a and Fig. 4.25b suggest that the air flow impinges the Alps from a slightly different angle in WRF as compared to COSMO-7. Furthermore, this observation manifests itself in the large area of underestimation of FAtriv (Fig. 4.25c) that can only be the result of different wind directions, meaning that air in WRF tends to approach the Alps more directly, in contrast to COSMO-7. This deviation in wind direction also explains the heavy biases for BF, FA and FAtriv in the Po Valley.

Fig. 4.26 shows that CCLM also suffers from deviating wind direction when compared to COSMO-7 resulting in underestimation of FAtriv as seen in Fig. 4.26c. After all, CCLM tends to overestimate the occurrence of unstable air, as visualised by the combination of US and USFAtriv of Fig. 4.26g, especially over France and north of the eastern outskirts of the Alps.

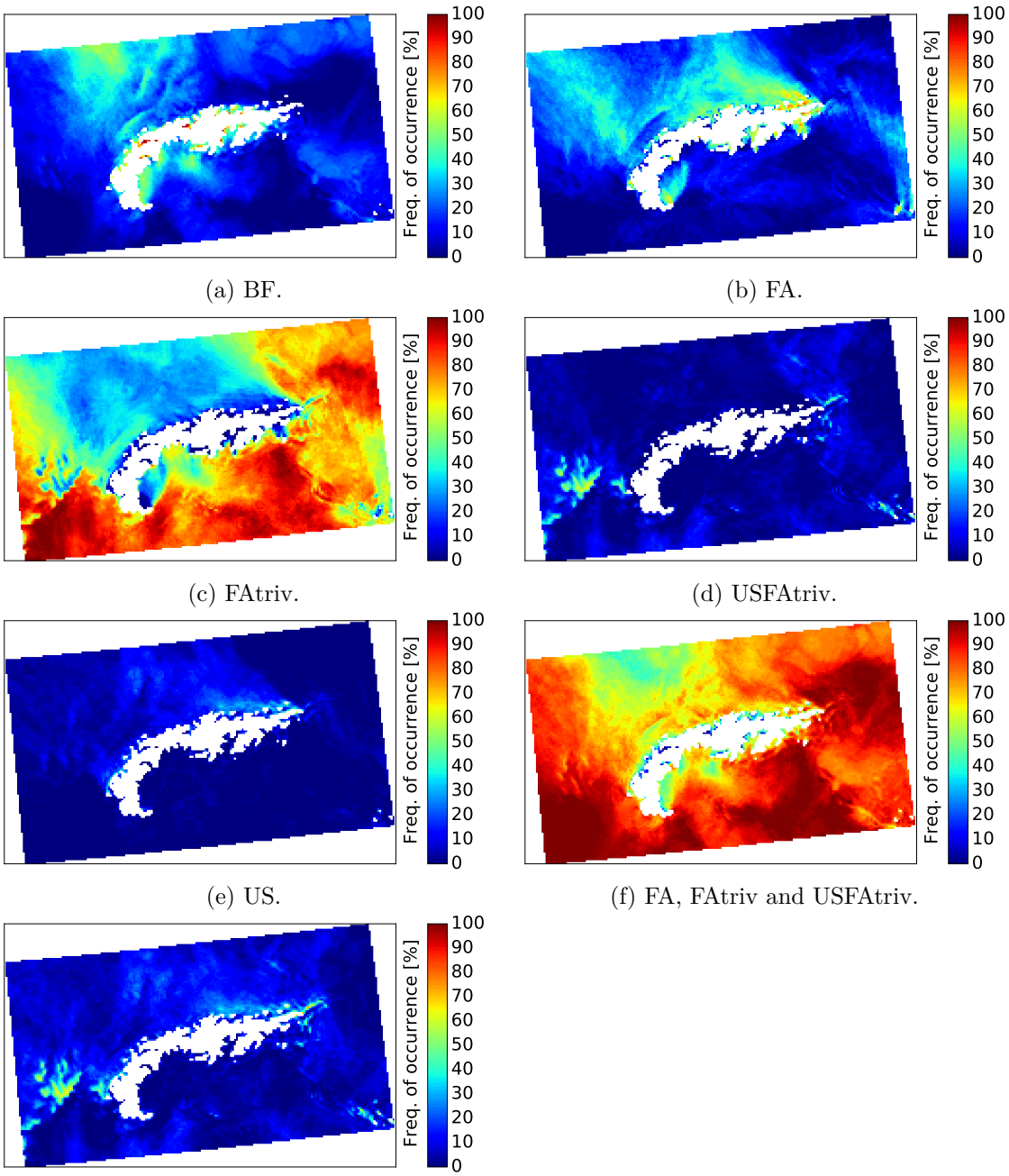

(a) BF.

(b) FA.

(c) FAtriv.

(d) USFAtriv.

(e) US.

(f) FA, FAtriv and USFAtriv.

(g) US and USFATriv.

Fig. 4.24 Frequency of occurrence for the different flow categories for November 2002 using data from COSMO-7 on an hourly basis for the KMN27 weather class 14. Detection height is 1500 m. Combined categories: (f) all categories with flow-above (FA, FAtriv, USFAtriv); (g) all categories with unstable stratification (US, USFAtriv).

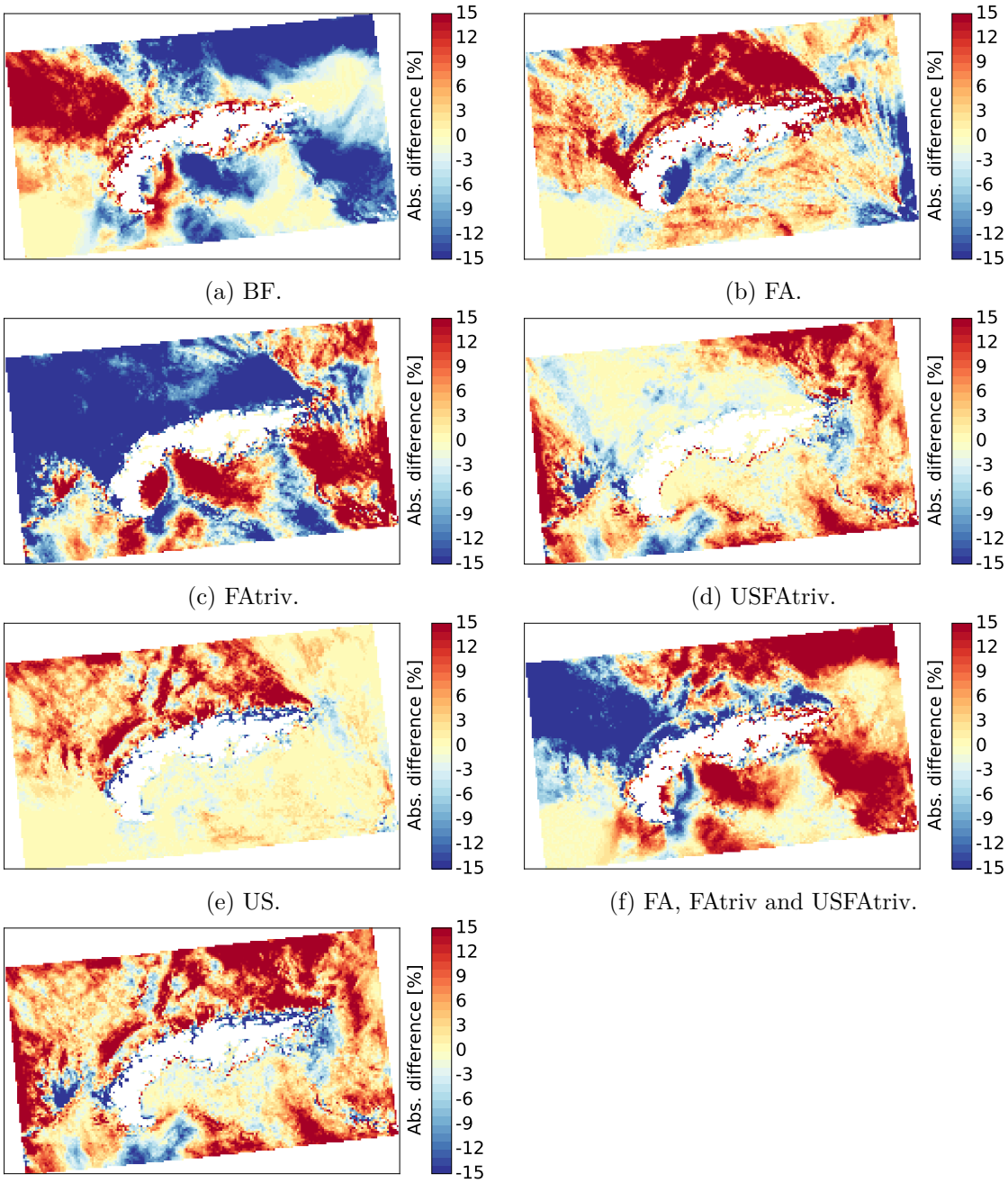

(a) BF.

(b) FA.

(c) FAtriv.

(d) USFAtriv.

(e) US.

(f) FA, FAtriv and USFAtriv.

(g) US and USFATriv.

Fig. 4.25 Absolute difference between the frequency of occurrence for different flow categories between WRF and COSMO-7 (see Fig. 4.24 for details). Red (blue) areas denote an overestimation (underestimation) of flow category appearance in WRF compared to COSMO-7.

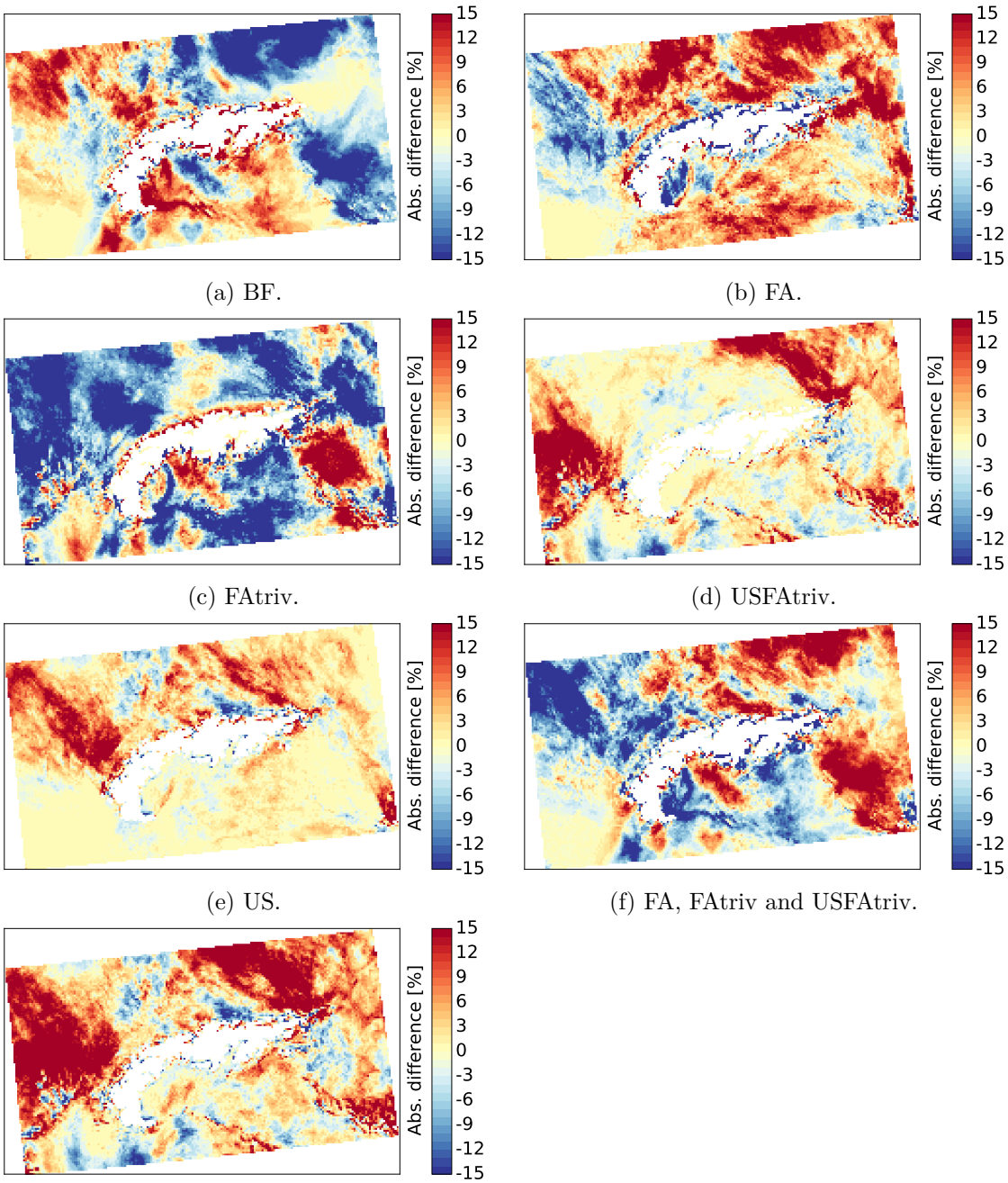

(a) BF.

(b) FA.

(c) FAtriv.

(d) USFAtriv.

(e) US.

(f) FA, FAtriv and USFAtriv.

(g) US and USFATriv.

Fig. 4.26 Same as Fig. 4.25 but comparing CCLM with COSMO-7.

5
Discussion and Conclusion

A variety of atmospheric situations, like foehn winds and barrier jets, are linked to orographically forced flows and are of great importance for the atmospheric sciences as well as the general public. These phenomena and their development can be described by the Froude number of continuum mechanics which is based on the three parameters wind speed, Brunt-Väisälä frequency and the height of the involved mountains. The development of a *flow analysis tool* that is based on this number and operates on three-dimensional data forms the core of this work. Its main components and features are summarised in the following.

Based on the calculated Froude number values and stability properties of air, five different flow categories, Blocked Flow (BF), Flow Above (FA), Trivial Flow Above (FAtriv), Unstably Stratified Air (US) and Unstably Stratified Air with Trivial Flow Above (USFAtriv), are introduced to describe the flow situations in complex terrain. However, the novelty of the flow analysis tool is its ability to operate on three-dimensional data at a grid cell resolution which means that every grid cell of air is individually assigned to one of these flow categories. This requires that the barrier height is calculated for each air parcel individually. Several algorithms that are suited for this task are presented in this work. An extension of these methods for larger domains, the so-called mountain weighting, is also developed in this work (see appendix B). However, this approach still requires further testing, as the domain used throughout this work is too small for this method to be meaningful.

The different methods for estimating the barrier height are compared and especially the Cone Search Method (CSM) is found to perform well. Furthermore, slight modifications of its free parameters only marginally change the computed results. A very time

efficient way to calculate an approximate barrier height (the maximum mountain height map (MMHM)) is also developed. Although this method suffers from artificial gradients in the Froude number field, it still compares well with the non-approximate methods. The mountain weighting method of appendix B, although not designed for this purpose, may provide a solution to this problem but requires further testing in this regard.

The correct treatment of moisture and condensation effects is incorporated using the virtual potential temperature (in cases of low relative humidity) and equivalent potential temperature (high relative humidity). A relative humidity threshold is used to determine which one of these temperature fields is selected within the algorithm on a grid cell level. The impact of the relative humidity field and its threshold value are found to be quite substantially and especially affects the BF category. Further studies that use different threshold values or omit the transition between the different potential temperatures altogether are also feasible and could reveal interesting results. In addition, a change in the Froude number threshold, which separates the flow categories BF and FA, is examined. The results confirm that this parameter has significant impact on the assignment of flow categories. The correct choice of this parameter is most crucial when the flow analysis tool is applied in any situation. Unfortunately, a single value that is optimised for any terrain (see e.g. Watson and Lane (2012)) can not be given at this point in time and may even be impossible.

The method for estimating the barrier height and the value of the Froude number threshold could both be used to incorporate additional non-linear effects like the shape of the barrier, heating from the ground or terrain roughness (see e.g. Reinecke and Durran (2008)). Taking these factors into consideration is crucial to establish a robust and trustworthy setting for all parameters within the flow analysis tool. Future testing may therefore include the tracking of air parcels over time, the comparison with precipitation data, temporal evolution of flow category clusters or even the interplay of the flow categories with front detection algorithms.

The monthly frequency of occurrence for the five different flow categories using data from the COSMO model in CLimate Mode (CCLM) and the Weather Research and Forecasting Model (WRF) are compared to data from the operational Swiss forecasting system COSMO-7. Since only data for one month (November 2002) is used in this work, no definite conclusions can be drawn regarding the performance of these Regional Climate Models (RCMs). Nevertheless, two distinct weather classes (a *Südstau* and a *Nordstau* type) are examined in detail to isolate certain synoptic situations. These results need to be interpreted with caution since the underlying weather typing is primarily tied to the COSMO-7 data set and may not represent the atmospheric conditions within CCLM and WRF at any given point in time (Kida et al. 1991). Therefore, this method may only be considered a first approximative comparison. Regardless of this fact, differences are clearly identified and point to a promising application of the flow analysis tool as a condition for model evaluation and error attribution purposes.

Bibliography

Baines, P. G. (1980). "The dynamics of the Southerly Buster." In: *Australian Meteorological Maganzine* 28, pp. 175–200 (cit. on p. 15).

– (1987). "Upstream Blocking and Airflow Over Mountains." In: *Annual Review of Fluid Mechanics* 19.1, pp. 75–95. DOI: doi:10.1146/annurev.fl.19.010187.000451 (cit. on p. 82).

– (1998). *Topographic Effects in Stratified Flows*. Cambridge Monographs on Mechanics and Applied Mathematics. Cambridge University Press, pp. 1–16. ISBN: 978052-1629232 (cit. on p. 4).

Bjerknes, V. (1904). "Das Problem der Wettervorhersage, betrachtet vom Standpunkte der Mechanik und der Physik." In: *Meteorologische Zeitschrift* 21, pp. 1–7 (cit. on p. 85).

Böhm, U., M. Kücken, W. Ahrens, A. Block, D. Hauffe, K. Keuler, B. Rockel, and A. Will (2006). "CLM - The climate version of LM: A Brief description and long-term applications." In: *COSMO newsletter* 6, pp. 225–235 (cit. on pp. 34, 36).

Bougeault, P. et al. (1993). "The atmospheric momentum budget over a major mountain range: First results of the PYREX field program." In: *Annales Geophysicae* 11, pp. 395–418 (cit. on pp. 1, 11).

– (2001). "The MAP Special Observing Period." In: *Bulletin of the American Meteorological Society* 82 (3), 433–462. DOI: 10.1175/1520-0477(2001)082<0433:TMSOP>2.3.CO;2 (cit. on p. 1).

Chanson, H. (2004). *Hydraulics of Open Channel Flow*. Elsevier Science, p. 39. ISBN: 9780080472973 (cit. on p. 4).

– (2009). "Current knowledge in hydraulic jumps and related phenomena: A survey of experimental results." In: *European Journal of Mechanics B. Fluids* 28 (2), pp. 191–210. DOI: 10.1016/j.euromechflu.2008.06.004 (cit. on p. 5).

Chow, F. K., S. F. J. De Wekker, and B. J. Snyder (2012). *Mountain Weather Research and Forecasting: Recent Progress and Current Challenges*. Springer Atmospheric Sciences. Springer Netherlands, pp. 121–208,219–249. ISBN: 9789400740983 (cit. on pp. 1, 5, 8–15).

Clancy, L. J. (1975). *Aerodynamics*. Pitman Aeronautical Engineering Series. Wiley, pp. 16–32. ISBN: 9780470158371 (cit. on p. 5).

Dee, D. P. et al. (2011). "The ERA-Interim reanalysis: configuration and performance of the data assimilation system." In: *Quarterly Journal of the Royal Meteorological Society* 137.656, pp. 553–597. DOI: 10.1002/qj.828 (cit. on p. 34).

Doms, G. and M. Baldauf (2015). "A Description of the Nonhydrostatic Regional COSMO-Model, Part I: Dynamics and Numerics." In: pp. 1–6,41. URL: http://www.cosmo-model.org/content/model/documentation/core/#p1 (visited on 06/22/2016) (cit. on pp. 34, 35, 37, 91).

Doyle, J. D. and D. R. Durran (2002). "The Dynamics of Mountain-Wave-Induced Rotors." In: *Journal of the atmospheric sciences* 59 (2), 186–201. DOI: 10.1175/1520-0469(2002)059<0186:TDOMWI>2.0.CO;2 (cit. on p. 11).

Holton, J. (2004). *An Introduction to Dynamic Meteorology*. An Introduction to Dynamic Meteorology Bd. 1. Elsevier Academic Press, pp. 118,474. ISBN: 97801235-40157 (cit. on pp. 89, 90).

Hughes, M., A. Hall, and R. G. Fovell (2008). "Blocking in Areas of Complex Topography, and Its Influence on Rainfall Distribution." In: *Journal of the Atmospheric Sciences* 66 (2), pp. 508–518. DOI: 10.1175/2008JAS2689.1 (cit. on pp. 29, 43).

Jacob, D. et al. (2014). "EURO-CORDEX: new high-resolution climate change projections for European impact research." In: *Regional Environmental Change* 14.2, pp. 563–578. DOI: 10.1007/s10113-013-0499-2 (cit. on p. 34).

Jones, P. W. (1999). "First- and Second-Order Conservative Remapping Schemes for Grids in Spherical Coordinates." In: *Monthly Weather Review* 127.9, 2204–2210 (cit. on p. 36).

Kida, H., T. Koide, H. Sasaki, and M. Chiba (1991). "A New Approach for Coupling a Limited Area Model to a GCM for Regional Climate Simulations." In: *Journal of the Meteorological Society of Japan. Ser. II* 69.6, pp. 723–728 (cit. on pp. 39, 66).

Klemp, J. B. and D. K. Lilly (1975). "The dynamics of wave-induced downslope winds." In: *Journal of the atmospheric sciences* 32 (2), pp. 320–339. DOI: 10.1175/1520-0469(1975)032<3C0320:TDOWID>3E2.0.CO;2 (cit. on p. 12).

Kraus, H. (2007). *Die Atmosphäre der Erde: Eine Einführung in die Meteorologie*. Springer Berlin Heidelberg, pp. 40–44,209–212. ISBN: 9783540350170 (cit. on pp. 29, 86).

Lackmann, G. M. and J. E. Overland (1989). "Atmospheric structure and momentum balance during a gap-wind event in Shelikof Strait, Alaska." In: *Monthly Weather Review* 117.8, pp. 1817–1833. DOI: 10.1175/1520-0493(1989)117<1817:ASAMBD>2.0.CO;2 (cit. on p. 15).

Lauscher, F. (1985). *Klimatologische Synoptik Österreichs mittels der ostalpinen Wetterlagenklassifikation*. Vol. 64. Arbeiten aus der Zentralanstalt für Meteorologie und Geodynamik: Publikation, Publikation Nr. 302. Zentralanstalt für Meteorologie und Geodynamik (cit. on p. 38).

Lilly, D. K. (1978). "A Severe Downslope Windstorm and Aircraft Turbulence Event Induced by a Mountain Wave." In: *Journal of the atmospheric sciences* 35 (1), 59–77. DOI: 10.1175/1520-0469(1978)035<0059:ASDWAA>2.0.CO;2 (cit. on p. 10).

Lin, Y. L. (2007). *Mesoscale Dynamics*. Cambridge University Press. ISBN: 9780521-808750 (cit. on pp. 4–6, 81).

Lin, Y.-L., S. Chiao, T.-A. Wang, M. L. Kaplan, and R. P. Weglarz (2001). "Some common ingredients for heavy orographic rainfall." In: *Weather and Forecasting* 16 (6), pp. 633–660. DOI: 10.1175/1520-0434(2001)016<0633:SCIFHO>2.0.CO;2 (cit. on p. 15).

Lions, J. L., R. Temam, and S. Wang (1992). "New formulations of the primitive equations of atmosphere and applications." In: *Nonlinearity* 5.2, p. 237 (cit. on p. 87).

Marsh, W. and M. Kaufman (2012). *Physical Geography: Great Systems and Global Environments*. Cambridge University Press, p. 123. ISBN: 9781107376649 (cit. on pp. 12, 14).

McCauley, M. P. and A. P. Sturman (1999). "A Study of Orographic Blocking and Barrier Wind Development Upstream of the Southern Alps, New Zealand." In: *Meteorology and Atmospheric Physics* 70 (3), pp. 121–131. DOI: 10.1007/s00703005-0029 (cit. on p. 30).

MeteoSwiss (2015). "COSMO-7 - the model for western and central Europe." In: URL: http://www.meteoswiss.admin.ch/home/measurement-and-forecasting-systems/warning-and-forecasting-systems/cosmo-forecasting-system/cosmo-7-the-model-for-western-and-central-europe.html (visited on 06/22/2016) (cit. on p. 37).

Miglietta, M. M. and R. Rotunno (2009). "Numerical simulations of conditionally unstable flows over a mountain ridge." In: *Journal of the Atmospheric Sciences* 66.7, pp. 1865–1885. DOI: 10.1175/2009JAS2902.1 (cit. on p. 17).

Neiman, P. J., F. M. Ralph, A. B. White, D. E. Kingsmill, and P. O. G. Persson (2002). "The statistical relationship between upslope flow and rainfall in California's coastal mountains: Observations during CALJET." In: *Monthly Weather Review* 130.6, pp. 1468–1492. DOI: 10.1175/1520-0493(2002)130<1468:Tsrbuf>2.0.Co;2 (cit. on pp. 13, 16).

Newman, J. N. (1977). *Marine Hydrodynamics*. Wei Cheng Cultural Enteroprise Company, p. 375. ISBN: 9780262140263 (cit. on p. 4).

Økland, H. (1990). "The dynamics of coastal troughs and coastal fronts." In: *Tellus A* 42.4, pp. 444–462. DOI: 10.1034/j.1600-0870.1990.t01-3-00004.x (cit. on p. 15).

Olafsson, H. and P. Bougeault (1996). "Nonlinear Flow Past an Elliptic Mountain Ridge." In: *Journal of the Atmospheric Sciences* 53.17, pp. 2465–2489. DOI: http://dx.doi.org/10.1175/1520-0469(1996)053<2465:NFPAEM>2.0.CO;2 (cit. on pp. 17, 20).

Olson, J. B. (2008). "The structure and dynamics of barrier jets along the southeast Alaskan coast." PhD thesis. State University of New York at Stony Brook (cit. on p. 17).

Olson, J. (2008). *The Structure and Dynamics of Barrier Jets Along the Southeast Alaskan Coast*. State University of New York at Stony Brook, pp. 1–4. ISBN: 97805-49914877 (cit. on pp. 2, 15).

Overland, J. E. and N. A. Bond (1995). "Observations and Scale Analysis of Coastal Wind jets." In: *Monthly Weather Review* 123.10, 2934–2941. DOI: http://dx.doi.org/10.1175/1520-0493(1995)123<2934:OASAOC>2.0.CO;2 (cit. on p. 17).

Parish, T. R. (1982). "Barrier Winds Along the Sierra Nevada Mountains." In: *Journal of Applied Meteorology* 21 (7), pp. 925–930. DOI: 10.1175/1520-0450(1982)021<0925:BWATSN>2.0.CO;2 (cit. on p. 15).

Philipp, A., C. Beck, R. Huth, and J. Jacobeit (2016). "Development and comparison of circulation type classifications using the COST 733 dataset and software." In: *International Journal of Climatology* 36.7, pp. 2673–2691. DOI: 10.1002/joc.3920 (cit. on p. 38).

Pielke, R. (2001). *Mesoscale Meteorological Modeling*. International Geophysics. Elsevier Science, p. 22. ISBN: 9780080491820 (cit. on p. 88).

Prein, A. F., W. Langhans, G. Fosser, A. Ferrone, N. Ban, K. Georgen, M. Keller, M. Tölle, O. Gutjahr, F. Feser, E. Brisson, S. Kollet, J. Schmidli, N. P. M. van Lipzig, and R. Leung (2015). "A review on regional convection-permitting climate modeling: Demonstrations, prospects, and challenges." In: *Review of Geophysics* 53 (2), pp. 323–361. DOI: 10.1002/2014RG000475 (cit. on p. 35).

Reinecke, P. A. and D. R. Durran (2008). "Estimating topographic blocking using a Froude number when the static stability is non-uniform." In: *Journal of Atmospheric Sciences* 65 (3), 1035–1048. DOI: 10.1175/2007JAS2100.1 (cit. on pp. 5, 26, 66, 85).

Richner, H. and T. Gutermann (2007). "Statistical analysis of foehn in Altdorf, Switzerland." In: *29th International Conference on Alpine Meteorology (ICAM 2007) 4 - 8 june, 2007, Chambéry, France ; extened abstracts. 2*, pp. 457–460 (cit. on p. 13).

Rogers, R. and M. Yau (1989). *A short course in cloud physics*. International series in natural philosophy. Pergamon Press. ISBN: 9780080348643 (cit. on p. 28).

Schlemmer, L., O. Martius, M. Sprenger, C. Schwierz, and A. Twitchett (2010). "Disentangling the Forcing Mechanisms of a Heavy Precipitation Event along the Alpine South Side Using Potential Vorticity Inversion." In: *Monthly Weather Review* 138.6, 2336–2353. DOI: http://dx.doi.org/10.1175/2009MWR3202.1 (cit. on pp. 2, 17).

Schoellhamer, D., J. Peters, and B. Larock (1985). "Subdivision Froude Number." In: *Journal of Hydraulic Engineering* 111 (7), pp. 1099–1104. DOI: 10.1061/(ASCE)0733-9429(1985)111:7(1099) (cit. on p. 21).

Seibert, P. (2005). *Hann´s Thermodynamic Foehn Theory and its Presentation in Meteorological Textbooks in the course of Time*. From Beaufort to Bjerknes and Beyhond, pp. 169–180. ISBN: 9783936905137 (cit. on p. 12).

Sheppard, P. A. (1956). "Airflow over mountains." In: *Quarterly Journal of the Royal Meteorological Society* 82.354, pp. 528–529. DOI: 10.1002/qj.49708235418 (cit. on p. 82).

Skamarock, W. C., J. B. Klemp, J. Dudhia, D. O. Gill, D. M. Barker, M. G. Duda, X.-Y. Huang, W. Wang, and J. G. Powers (2008). "A Description of the Advanced Research WRF Version 3." In: *NCAR Technical Note NCAR/TN-475+STR* 88. DOI: 10.5065/D68S4MVH (cit. on pp. 34, 36).

Smith, R. B. (1987). "Aerial observations of the Yugoslavian bora." In: *Journal of the atmospheric sciences* 44 (2), 269–297. DOI: 10.1175/1520-0469(1987)044<0269:AOOTYB>2.0.CO;2 (cit. on p. 11).

Smolarkiewicz, P. and R. Rotunno (1990). "Low Froude number flow past three-dimensional obstacles. Part II: Upwind flow reversal zone." In: *Journal of the Atmospheric Sciences* 47 (12), pp. 1498–1511. DOI: 10.1175/1520-0469(1990)047<1498:LFNFPT>2.0.CO;2 (cit. on p. 30).

Stensrud, D. (2007). *Parameterization Schemes: Keys to Understanding Numerical Weather Prediction Models*. ISBN: 9780521865401 (cit. on p. 90).

Steppeler, J., G. Doms, U. Schättler, W. H. Bitzer, A. Gassmann, U. Damrath, and G. Gregoric (2003). "Meso-gamma scale forecasts using the nonhydrostatic model LM." In: *Meteorology and Atmospheric Physicso* 82, pp. 75–96. DOI: 10.1007/s00703-001-0592-9 (cit. on p. 34).

Storch, H. von, S. Güss, and M. Heimann (2013). *Das Klimasystem und seine Modellierung: Eine Einführung*. Springer Berlin Heidelberg, pp. 99–114. ISBN: 97836425-85289 (cit. on pp. 85, 86).

Stull, R. B. (1988). *An Introduction to Boundary Layer Meteorology*. Atmospheric and Oceanographic Sciences Library. Springer Netherlands, pp. 75–80,587–609. ISBN: 9789027727688 (cit. on pp. 4, 6–8, 45, 48, 86–88).

Sun, W.-Y. and O. M. Sun (2015). "Bernoulli equation and flow over a mountain." In: *Geoscience Letters* 2.1, pp. 1–12. DOI: 10.1186/s40562-015-0024-1 (cit. on pp. 4, 5).

Takahashi, T. (2014). *Debris Flow: Mechanics, Prediction and Countermeasures, 2nd edition*. CRC Press, p. 148. ISBN: 9780203576748 (cit. on p. 4).

Watson, C. D. and T. P. Lane (2012). "Sensitivities of Orographic Precipitation to Terrain Geometry and Upstream Conditions in Idealized Simulations." In: *Journal of the atmospheric sciences* 69.4, pp. 1208–1231. DOI: 10.1175/JAS-D-11-0198.1 (cit. on pp. 15, 66).

White, F. M. (2003). *Fluid Mechanics*. McGraw-Hill international editions. McGraw-Hill, p. 314. ISBN: 9780072402179 (cit. on p. 3).

Whiteman, C. (2000). *Mountain Meteorology: Fundamentals and Applications*. Oxford University Press, pp. 147–148. ISBN: 9780198030447 (cit. on pp. 9, 10).

Würsch, M. and M. Sprenger (2015). "Swiss and Austrian Foehn revisited: A Lagrangian-based analysis." In: *Meteorologische Zeitschrift* 24 (3), 225–242. DOI: 10.1127/metz/2015/0647 (cit. on p. 12).

Acronyms

BF Blocked Flow. 30, 38, 39, 41–43, 45, 48, 51, 53, 56, 59, 60, 65, 66

CAPE convective available potential energy. 17, 38, 53, 59, 77, 78

CCLM COSMO model in CLimate Mode. i, iii, 33–37, 39, 51, 56, 60, 66, 78

COSMO COnsortium for Small scale MOdeling. 34

COSMO-7 COSMO model version 7. i, 33, 35–37, 39, 51, 53, 56, 59, 60, 66, 76, 78

CPCM Convection Permitting Climate Model. 1, 2, 90

CSM Cone Search Method. 23–25, 42, 65, 76, 77, 83

DWD German Weather Service. 34

ECMWF European Centre for Medium-Range Weather Forecasts. 17, 37

ERA-Interim European Centre for Medium-Range Weather Forecasts Re-Analysis Interim. 34, 38, 39, 76

EURO-CORDEX COordinated Regional climate Downscaling EXperiment - EUROpean domain. 34, 35

FA Flow Above. 30, 31, 39, 41–43, 45, 48, 51, 53, 59, 60, 65, 66, 77, 78

FAtriv Trivial Flow Above. 31, 43, 45, 51, 53, 60, 65, 77, 78

FWF Austrian Science Fund. v

GCM Global Climate Model. 39

KMN27 k-means cluster analysis. 38, 53, 59, 60, 77, 78

LM COSMO Limited-area Modelling. 34

MAP Mesoscale Alpine Programme. 1

MMHM maximum mountain height map. 24, 25, 39, 41, 42, 51, 65, 76, 77

NHCM-2 Non-Hydrostatic Climate Modelling, Part II. i, iii, v, 35

PYREX Pyrenean Experiment. 1

RCM Regional Climate Model. i, 33, 34, 66, 76

SLM Straight Line Method. 22–25, 41, 76, 83

US Unstably Stratified Air. 31, 43, 45, 48, 51, 53, 60, 65, 77, 78

USFAtriv Unstably Stratified Air with Trivial Flow Above. 31, 43, 45, 51, 53, 60, 65, 77, 78

UTC Coordinated Universal Time. 40, 43, 45, 48, 76, 77

WEGC Wegener Center University of Graz. 35, 36, 53, 59, 77, 78

WRF Weather Research and Forecasting Model. i, iii, 33, 36, 37, 39, 40, 43, 45, 51, 53, 56, 60, 66, 77, 78

List of Figures

2.1 Flow regimes for uniform two dimensional flow for different Froude number values. (a) super-critical flow for large Froude numbers; (b) flow with hydraulic jump that is propagating upstream and downstream; (c) flow with stationary hydraulic jump downstream and an upstream propagating jump; (d) completely blocked flow; (e) sub-critical flow for low Froude numbers. From Lin (2007). 6

2.2 Schematic illustration of flow over an isolated mountain for different Froude number values F_{wave} which compares the natural wavelength of air with the length of the obstacle. Adopted from Stull (1988). 7

2.3 Schematic illustration of the development of mountain waves. From Whiteman (2000). 9

2.4 Mountain waves and lee waves as generated by flow over a mountain. From Whiteman (2000). 10

2.5 Two lee wave rotors as simulated by Doyle and Durran (2002) for a two-dimensional idealised case. Streamlines depict airflow. Horizontal wind speeds to the left are shaded in grey. From Doyle and Durran (2002). . . 11

2.6 The 11 January 1972 downslope windstorm over Boulder (Colorado, U.S.A.) in a cross section view. Potential temperature field is shown as black lines. From Klemp and Lilly (1975). 12

2.7 Schematic illustration of the foehn type I ("Swiss foehn type"). From Chow et al. (2012). 13

2.8 Characterising foehn winds including blocked air (depth A). Foehn type I: $A = 0$ (no blocked air). Foehn type II: $A = C$ (all of the air below ridge height C is blocked). $\Delta\theta$ describes the difference in potential temperature between the blocked air and the air above. From Chow et al. (2012). . . . 14

2.9 Illustration of massive orographic precipitation on Mt. Waialeale, Hawaii. From Marsh and Kaufman (2012). 14

2.10 Cross section view of orographically forced precipitation in the case of unblocked (upper panel) and blocked (lower panel) low-level flows towards coastal mountains. Coastal profiles of wind velocity shown on the left. The rain intensity is proportional to the spacing between rain streaks. The blocked flow in the lower panel moves parallel to the mountain ridge and forms a barrier jet. Adopted from Neiman et al. (2002). 16

3.1 Example orography of the Alpine region for which the maximum mountain heights need to be computed. 22
3.2 Example for a maximum barrier height field H_m calculated using Straight Line Method (SLM) if the wind direction is assumed to be uniform across the domain at a 140° angle (i.e. from southeast to northwest as denoted by the black arrow). Air parcel height is not yet subtracted. 23
3.3 Example for a maximum barrier height field H_m calculated using CSM if the wind direction is assumed to be uniform across the domain at a 140° (i.e. from southeast to northwest as denoted by the black arrow). Air parcel height is not yet subtracted. 25
3.4 Schematic illustration of the components of the algorithm: an air parcel (1) at height H_{air} is approaching a mountain of height H_m with wind speed U; the remaining barrier height is h. The Brunt-Väisälä frequency N is calculated using a reference air parcel (2) at height H_m. If the computed Froude number fulfils the condition $F > 1$, the air parcel is able to move over the mountain. 27

4.1 RCM model domains on a 12.5 km grid spacing driven by European Centre for Medium-Range Weather Forecasts Re-Analysis Interim (ERA-Interim) data. Dynamically downscaled once more to a 3 km convection permitting scale. Adopted from Prein et al. (2015). 35
4.2 Model orography of the Alpine region after regridding to the COSMO model version 7 (COSMO-7) grid (data from WRF). 36
4.3 The domain covered by the COSMO-7 forecast system. From MeteoSwiss (2015). 37
4.4 The synoptic situation in Europe two hours after the time of interest for this section (1 December 2002 at 0000 Coordinated Universal Time (UTC)). Pressure is denoted as contour lines and fronts are shown as bold lines (triangles: cold fronts, semicircles: warm fronts). The red rectangle approximately indicates the domain of the Alpine region as used in the following. Adopted from www.wetterzentrale.de. 40
4.5 Maximum obstacle height and flow categories calculated using SLM. . . . 41
4.6 Maximum obstacle height and flow categories calculated using MMHM for SLM. 41

4.7 Maximum obstacle height and flow categories calculated using MMHM for CSM with a half cone opening angle of 5°. 42
4.8 Maximum obstacle height and flow categories calculated using MMHM for CSM with a half cone opening angle of 10°. 42
4.9 Flow categories for changed relative humidity and Froude number thresholds. 43
4.10 Input variables and computed fields for 30 November 2002 at 2200 UTC from WRF at 1500m above sea level. Streamlines depict airflow. Relative humidity (e) is separated into above and below the threshold (90%), revealing its influence on the Brunt-Väisälä frequency (f). Imaginary values for N in (f) are set to $N = 0$. Froude number values (g) are capped at 2.0; values of $F = 0$ indicate unstable stratification. Flow categories (h) combine the information of the Froude number and stability. 44
4.11 Vertical distribution of flow categories for 30 November 2002 at 2200 UTC for different heights above sea level (asl) with data from WRF; streamlines depict airflow. The purple line in (e) shows the vertical domain cut used for Fig. 4.12. Note that the detection height does not increase linearly between the images. 46
4.12 Vertical cut through the domain as indicated by the purple line in Fig. 4.11e for 30 November 2002 at 2200 UTC; data from WRF. The situation is similar to that of Fig. 3.4. Streamlines depict airflow parallel to the direction from point A to B. 47
4.13 Wind profile for the wind component parallel to the cut through the domain corresponding to Fig. 4.12. Positive values indicate wind from left to right. 47
4.14 Schematic illustration of stagnant flow for low Froude number (see also Fig. 2.2). Mountain and blocked air together form a combined obstacle that is more streamlined than the mountain on its own. This is similar to Fig. 4.12. Adopted from Stull (1988). 48
4.15 Flow categories (left column) and absolute wind speed (right column) for 30 November 2002 in 1500 m asl. Data from WRF. Stream lines depict airflow. 49
4.16 Continuation of Fig. 4.15. 50
4.17 Frequency of occurrence for the different flow categories for November 2002 using data from WRF on an hourly basis. Detection height is 1500 m. The *stripes* in (b) and (c) are discussed in the text. Combined categories: (f) all categories with flow-above (FA, FAtriv, USFAtriv); (g) all categories with unstable stratification (US, USFAtriv). 52
4.18 The artificial stripes of Fig. 4.17b examined in detail. Red circles: isolated mountain peaks are the source of all stripes. Dashed lines indicate that the stripes are fanned out with a 5° angle between them. 53

4.19 Illustration of the k-means cluster analysis (KMN27) weather class 3. Blue arrows depict air flow; black lines denote pressure; convective available potential energy (CAPE) shown in colour. The histogram in the bottom left corner denotes the relative annual frequency of this weather class. Adopted from current work at the Wegener Center University of Graz (WEGC). 54
4.20 Frequency of occurrence for the different flow categories for November 2002 using data from COSMO-7 on an hourly basis for the 8 days of the KMN27 weather class 3. Detection height is 1500 m. Combined categories: (f) all categories with flow-above (FA, FAtriv, USFAtriv); (g) all categories with unstable stratification (US, USFAtriv). 55
4.21 Absolute difference between the frequency of occurrence for different flow categories between WRF and COSMO-7 (see Fig. 4.20 for details). 57
4.22 As Fig. 4.21 but comparing CCLM with COSMO-7 (see Fig. 4.20 for details). 58
4.23 Illustration of the KMN27 weather class 14. Blue arrows depict air flow; black lines denote pressure; convective available potential energy (CAPE) shown in colour. The histogram in the bottom left corner denotes the relative annual frequency of this weather class. Adopted from current work at the WEGC. 59
4.24 Frequency of occurrence for the different flow categories for November 2002 using data from COSMO-7 on an hourly basis for the KMN27 weather class 14. Detection height is 1500 m. Combined categories: (f) all categories with flow-above (FA, FAtriv, USFAtriv); (g) all categories with unstable stratification (US, USFAtriv). 61
4.25 Absolute difference between the frequency of occurrence for different flow categories between WRF and COSMO-7 (see Fig. 4.24 for details). Red (blue) areas denote an overestimation (underestimation) of flow category appearance in WRF compared to COSMO-7. 62
4.26 Same as Fig. 4.25 but comparing CCLM with COSMO-7. 63

B.1 One possible way for a mountain height weighting function using a combination of Gaussian functions surrounding a plateau of constant values. The air parcel under consideration is located at the origin with wind direction along the positive x-axis. 83
B.2 An example application of the mountain weighting function, as evaluated for an air parcel sitting at the sharp tip of the structure of the left panel, moving in a northeastern direction (as denoted by the white arrow). The right panel shows the *effective orography* as used for calculating the maximum obstacle height for this air parcel. 84

B.3 Example for a maximum barrier height field H_m calculated using weighted mountain heights if the wind direction is assumed to be uniform across the domain with a 140° angle (i.e. from southeast to northwest as denoted by the black arrow). Air parcel height is not yet subtracted. 84
D.1 Arakawa-C/Lorenz grid staggering used in many atmospheric models. u, v and w denote wind components. From Doms and Baldauf (2015). 91

Appendix

A Froude Number from Kinetic and Potential Energy

Alongside its many different forms, the Froude number F (i.e. its square F^2) can also be defined simply as the ratio of kinetic energy T of an air parcel to the potential energy Φ that is required to surpass a barrier of certain height (Lin 2007),

$$F^2 = T/\Phi \; . \tag{A.1}$$

Section 2.1 already presented a straightforward way to obtain the final form of the Froude number $F = U/Nh$. Nevertheless, an instructive alternative derivation for equation (2.4) based on the energy ratio is given hereafter. For simplicity, the height dependence of the air density is considered instead of the change of potential temperature.

First of all, the kinetic energy of an air parcel with mass m and velocity U can be defined per unit volume V as

$$\frac{T}{V} = \frac{mU^2}{2}\frac{1}{V} = \frac{\rho U^2}{2} \; , \tag{A.2}$$

using the density ρ of the given air parcel.

Secondly, the required energy for moving an object along the coordinate s for a distance h when a force $F(s)$ acts on that object is the integral over the force

$$\Phi = \int_0^h F(s) ds \; . \tag{A.3}$$

For an air parcel in the atmosphere, this force is not simply the force due to gravity mg_0 but the remaining force acting on an air parcel that is already floating in a stable stratified surrounding. Therefore, this force (per unit volume V) follows Hooke's law for the restoring forces of a spring and is proportional to the vertical density change and the amount of vertical displacement s

$$\frac{F(s)}{V} = -g_0 \left(\frac{d\rho}{dz} \right) s \; . \tag{A.4}$$

This expression can be derived considering the net force onto an air parcel due to pressure

forces. However, this simply corresponds to the air parcel being *too heavy* compared to its new surrounding after lifting, thus being forced back into its original position.

Assuming that the vertical change of density $d\rho/dz$ is constant (for small distances h), the integral in (A.3) can be carried out easily to obtain the potential energy per unit volume

$$\begin{aligned}\frac{\Phi}{V} &= \int_0^h \frac{F(s)}{V} ds = -g_0 \left(\frac{d\rho}{dz}\right) \int_0^h s \; ds \\ &= \underbrace{-g_0 \left(\frac{d\rho}{dz}\right)}_{\rho N^2} \frac{h^2}{2} \\ &= \frac{\rho h^2 N^2}{2} \; .\end{aligned} \tag{A.5}$$

The last step utilises the definition of the squared Brunt-Väisälä frequency

$$N^2 = -\frac{g_0}{\rho} \left(\frac{d\rho}{dz}\right) \; . \tag{A.6}$$

Equation (A.1) can now be expressed using the kinetic and potential energy (per unit volume) to obtain

$$F^2 = \frac{T}{\Phi} = \frac{T/V}{\Phi/V} = \frac{\rho U^2/2}{\rho h^2 N^2/2} = \frac{U^2}{h^2 N^2} \; . \tag{A.7}$$

Taking the square root finally yields the desired equation for the Froude number as used throughout this work

$$F = \sqrt{F^2} = \frac{U}{hN} \; . \tag{A.8}$$

This derivation can also be carried out for replacing density ρ with potential temperature θ. In that case, the definition for the Brunt-Väisälä frequency from equation (2.3) has to be used.

Additional information on the energy argument for the Froude number can be found in Sheppard (1956) and Baines (1987).

B Weighted Mountain Heights

Section 3.2 provides some basic algorithms for the calculation of the maximum mountain height values for any given domain. However, using a large domain (e.g. whole Europe) means that mountains that are very far away can influence the calculated maximum mountain height even if the air parcel is unlikely to reach these mountains. In this case, neither the Straight Line Method (SLM) nor the Cone Search Method (CSM) are suitable choices since both methods use unlimited search range. However, limiting the search range by a fixed cut-off value naturally introduces large gradients in the spatial distribution of highest mountain values.

One possible solution to this problem is the use of weighted mountain heights using an artificial but well-considered weighting function in order to suppress the influence of mountains that are far away. This method can be generalised to also suppress the height of mountains that deviate strongly from the air parcels flow direction. Fig. B.1 shows one possible weighting function with non-trivial angle and radial dependence.

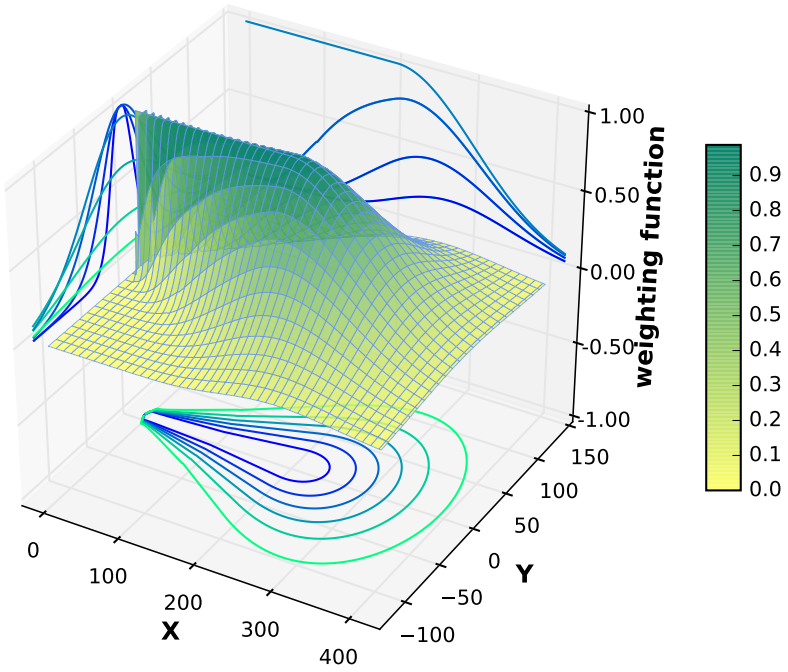

Fig. B.1 One possible way for a mountain height weighting function using a combination of Gaussian functions surrounding a plateau of constant values. The air parcel under consideration is located at the origin with wind direction along the positive x-axis.

Fig. B.2 explains the process of the mountain weighting in more detail. When the weighting function of Fig. B.2a is applied to the entire model orography (see Fig. 3.1)

only the forward-cone region, with its round end pointing into the flow direction of the air parcel, remains (Fig. B.2b). Finally, the highest point of orography in this modified field needs to be found.

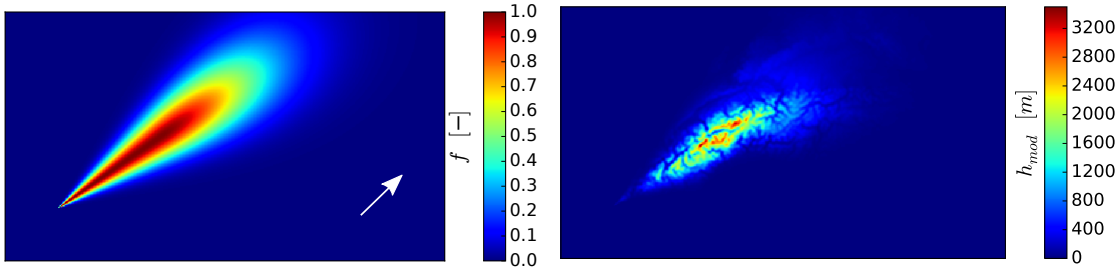

(a) Weighting function values.

(b) Effective orography

Fig. B.2 An example application of the mountain weighting function, as evaluated for an air parcel sitting at the sharp tip of the structure of the left panel, moving in a north-eastern direction (as denoted by the white arrow). The right panel shows the *effective orography* as used for calculating the maximum obstacle height for this air parcel.

Fig. B.3 shows that the *reversed shadow* created by the Alps in the maximum barrier height plot for uniform wind direction does not carry over to the edges of the domain. This cut-off does not produce any artefacts since the edges are smoothed out using the weighting function as shown in Fig. B.1.

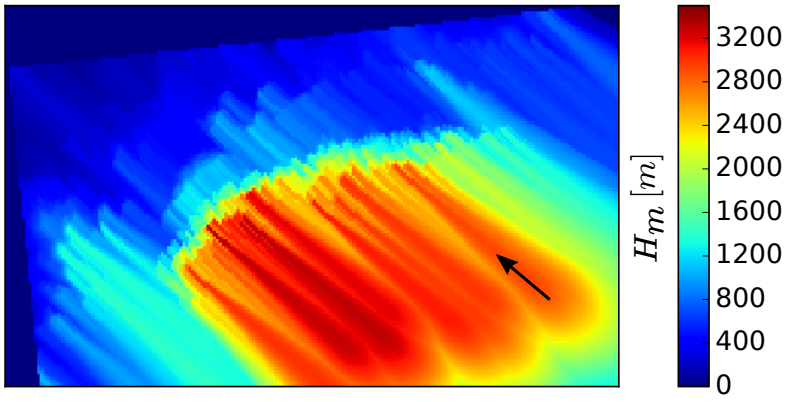

Fig. B.3 Example for a maximum barrier height field H_m calculated using weighted mountain heights if the wind direction is assumed to be uniform across the domain with a 140° angle (i.e. from southeast to northwest as denoted by the black arrow). Air parcel height is not yet subtracted.

However, the domain size as used throughout this work can be considered too small for the mountain weighting approach to be necessary which is why this approach is no

longer pursued in this work. This methods potential to remove the *artificial stripes* of section 4.3 is also not examined in this work.

This method might be extended by using *any* other way of estimating the barrier height, including vigorous smoothing of the model orography to further reduce sharp edges at the cone borders, constant barrier height values for more or less uniform flow or more complicated methods taking into account the shape of the mountain ridge, friction and other effects (as discussed in Reinecke and Durran (2008)).

C Atmospheric Modelling and Primitive Equations

The flow analysis tool (as introduced in chapter 3) is designed to use data from numerical simulations of the state of the atmosphere. This section provides a short introduction to the basic equations of these simulations.

In order to get a quantitative description of the state of the atmosphere, atmospheric modelling utilises the equations of fluid mechanics to describe the (thermo-)dynamics of the gases in the atmosphere. Forecasting, mostly numerical, is not only useful for short term weather predictions but also for the evaluation of the long term climate behaviour in the case of changes to the energy budget (e.g. a change in carbon dioxide concentrations) (Storch et al. 2013). In this case, due to the chaotic nature of the system, only mean variables are to be interpreted. In either case, the underlying equations are the same and contain both time and space derivatives that require boundary and initial conditions to be solved. These equations (called *primitive equations* in the following) have been compiled first by Bjerknes (1904) and consist of:

- the hydrodynamic equations of motion,
- the equation of state for the atmosphere,
- the equation of continuity for a fluid in motion and
- the laws of thermodynamics.

Together they describe the seven atmospheric variables:

- density of air ρ,
- temperature T,
- pressure p,
- specific humidity q and
- the three velocity components of the wind vector $\vec{v}$.

It should be noted that the inclusion of other variable components of the atmosphere (like air pollutants) would result into additional equations for each additional component. However, this description obviously lacks any inclusion of other effects that may influence

the atmosphere, whether they are of electrical, optical or of any other nature. This highlights that any system that is to be modelled - especially a complex one such as the earth's atmosphere - is always subject to *simplifications* of reality. This is achieved by only including the dominant and important processes while neglecting others (Storch et al. 2013). Regardless of this fact, a short description of the primitive equations of atmospheric modelling is given in the following.

Most of the discussed equations are based on conservation principles that make use of a simple budget equation for different conserved variables (see e.g. Kraus (2007) and Stull (1988)). If ϕ is such a conserved variable, this equation states that its change over time at a fixed point in space can only stem from advection of ϕ itself (e.g. the transport of a pollutant by the wind field $\vec{v}$) or by explicit sources or sinks S_ϕ of ϕ (e.g. the creation of a pollutant through chemical combustion or the absorption of the same by biological processes):

$$\frac{\partial \phi}{\partial t} = -\vec{v} \cdot \nabla \phi + S_\phi(\vec{r}, t) \; . \tag{C.1}$$

$S_\phi(\vec{r}, t)$ is in general allowed to change in space and time with positive values representing sources and negative values representing sinks. In the special case of $S(\vec{r}, t) = 0$, the variable ϕ is said to be conserved.

Equation of Motion

Using Newtons second law $\vec{F} = m\vec{a}$ in a rotating frame of reference (the earth's rotation), the acceleration field $\vec{a}$ for the hydrodynamic flow of air can be written as:

$$\vec{a} = \dot{\vec{v}} = -2(\vec{\Omega} \times \vec{v}) + \vec{F}/m \; , \tag{C.2}$$

with $\vec{\Omega}$ denoting the angular velocity of the rotating frame. To expand the total (or advective) derivative $\dot{\vec{v}} = d\vec{v}/dt$ into an explicit and an advective term, the general definition of a total derivative of an arbitrary variable ϕ

$$\frac{d\phi}{dt} = \frac{\partial \phi}{\partial t} + \vec{v} \cdot \nabla \phi \; , \tag{C.3}$$

needs to be used (which is similar to the advection term in equation (C.1)). $\vec{F}$ in equation (C.2) still contains all forces that are acting within the system. For example, any local variation in pressure will evoke *pressure gradient forces* that attempt to balance these deviations. Together with a gravitational force term $\vec{g}$, equation (C.2) can be written as

$$\frac{\partial \vec{v}}{\partial t} + \vec{v} \cdot \nabla \vec{v} = -2\vec{\Omega} \times \vec{v} - \frac{1}{\rho} \nabla p + \vec{g} + \vec{f} \; . \tag{C.4}$$

An additional force term $\vec{f}$ (force per unit mass) was included to denote other forces that are not yet accounted for by this equation (e.g. viscous stress) (Stull 1988).

Equation of State

To a good approximation, the earth's atmosphere can be described as an ideal gas. Therefore, the ideal gas law

$$p = \rho R_s T \ , \tag{C.5}$$

applies, with pressure p, density of air ρ, specific gas constant of air mixture R_s and the absolute temperature T (Stull 1988). This is the only one of the primitive equations that is not in differential form.

Equation of Continuity

The equation of continuity is a result of the claim that mass needs to be conserved during motion. That is, mass cannot be destroyed or created but only be transported through the system. Using $S_{mass} = 0$, the conservation principle of equation (C.1) leads to the familiar equation of continuity

$$\frac{\partial \rho}{\partial t} + \nabla(\vec{j}) = 0 \ , \tag{C.6}$$

with mass current density $\vec{j} = \rho\vec{v}$. The conservation of mass m in an arbitrary volume V has been formulated by means of the density ρ in this volume. However, this equation is only true for the *total mass* of air. Any single constituent of the air (may it be moisture or chemical components) satisfies its own equation of conservation with non-vanishing sink/source term S according to equation (C.1).

Thermodynamic Energy Equation

To account for the conservation of total internal energy U^{tot} from the first law of thermodynamics,

$$\Delta U^{tot} = W + Q \ , \tag{C.7}$$

with work upon the system W and added heat content Q, the total derivative of the temperature T of an air parcel can be written as

$$c_p \frac{dT}{dt} = \frac{RT}{p}\frac{dp}{dt} + \frac{dQ}{dt} \ , \tag{C.8}$$

using the specific heat for constant pressure c_p. dQ/dt describes the heat flux including molecular, turbulent, radiative and evaporative heating (Lions et al. 1992).

Numeric Solution of the Primitive Equations

The above discussed equations of motion together with the other conservational properties of the atmosphere form a set of equations that should enable the ambitious mathematician to write down the (analytical) solution (i.e. the evolution in time) for all atmospheric parameters as introduced above. However, the complexity of this set of equations renders any analytical solution for general flows impossible as explained below. The urge to solve the primitive equations has led to the following steps to obtain a useful climate model:

- gathering information on initial and boundary conditions,
- simplification of the equations,
- discretisation of the equations,
- Reynolds averaging and
- parametrisations of subscale processes,

all of which are to be explained briefly in the following.

First of all, when applying the primitive equations to the turbulent flow of the atmosphere, the differential nature of the equations requires sufficiently detailed knowledge of initial and boundary conditions to resolve all turbulent scales - from large scale planetary waves to every single little turbulence on a microscopic scale. Gathering this information is of course an impossible task. On the other hand, most of the time forecasting every single eddy is not even of interest in climate simulations. To simplify this tremendous task, a cut-off eddy size can be applied that separates the resolved motions of the atmosphere (large scale) from the statistically treated small scale effects (Stull 1988). This cut-off can range from 10 to 100 km for *synoptic models* down to 100 m for so-called *large eddy simulation models*.

The systematic approach to isolate the important processes that need to be captured in the simulation is known as the *scale analysis* which compares the order of magnitude of different physical processes to identify effects that can be neglected in the simulation (Pielke 2001). This reduction of complexity has allowed progress in atmospheric simulations that would otherwise have been very difficult or even impossible (Stull 1988).

The second problem with the derived set of equations is their complexity: even after solving the initial and boundary condition problem, it turns out that the non-linearities within the equations and their coupling renders any analytical solution impossible. This fact becomes quite obvious considering that even the rather simple three-body problem of celestial mechanics eludes itself from any analytical solution. One way to solve this problem is to utilise the powerful machinery of numerical approaches as enabled by the fast improvement of computational capabilities of the last decades.

One of the first steps of obtaining a numerical solution to differential equations always includes discretisation of the equations, that is, introducing a discrete grid for space and time on which the equations are defined (as compared to a continuum), using grid spacing parameters Δx and Δt. This is necessary to dissect the derivatives of the equations using only known quantities. For example, the spatial derivative of a variable ϕ at position n can be written as a function of ϕ itself using the *central difference method* as:

$$\left.\frac{\partial \phi}{\partial x}\right|_n = \frac{\phi^{n+1} - \phi^{n-1}}{2\Delta x} + \mathcal{O}\left(\Delta x^2\right) \ , \tag{C.9}$$

using the grid spacing of the spatial discretisation Δx and evaluating ϕ at grid points spatially adjacent to point n. This equation also highlights that these discretisations are always only approximations, in this case neglecting terms of order Δx^2. Although the discretisation schemes used in modern climate simulations (such as 3rd order Runge-Kutta or 2nd order leapfrog schemes) are far more sophisticated than the simple central difference method of equation (C.9), this error can be reduced to higher orders of the discretisation parameter but can never be eliminated entirely. Of course, the accuracy of the obtained solution can be increased by smaller grid spacing at the expense of increased computational effort.

An important observation regarding turbulent fluids is that many field variables, e.g. the velocity at any given point, changes rapidly with time since eddies of all scales pass through the point. To further simplify the model equations that should represent large-scale flow the so-called *Reynolds averaging* assumes that any variable of interest ϕ can be separated into a slowly varying average value $\overline{\phi}$ and a rapidly changing turbulent component ϕ' which represents the unresolved sub-grid scale fluctuations of ϕ according to

$$\phi = \overline{\phi} + \phi' \ . \tag{C.10}$$

The reason for doing so reveals itself when acting upon the model equations with an *averaging operator*, that may be denoted with an overbar symbol as $\overline{(\quad)}$, and may represent either spatial or temporal averaging or a combination of both. Since per definition, the average of a fluctuation component vanishes, that is $\overline{\phi'} = 0$, the equations simplify and turn into a set of equations for the averaged quantities. However, the average of a product (e.g. $\overline{\phi\,\omega}$) of variables ϕ and ω does not simplify in a trivial way as can be seen from

$$\overline{\phi\,\omega} = \overline{(\overline{\phi} + \phi')(\overline{\omega} + \omega')} = \overline{\phi}\overline{\omega} + \overline{\phi'\omega'} \ , \tag{C.11}$$

introducing the *covariance* as the product of deviation components which in general is not zero (Holton 2004).

To circumvent the calculation of terms including the fluctuations of variables, they are replaced by *parametrisations* that represent the approximation of unresolved physical processes using only resolved variables. This can be considered one of the most

difficult and controversial areas of climate modelling (Holton 2004). Although it is desirable that these parametrisations are based on real physical relationships, not all of the underlying processes are fully understood for all appearing terms. Additionally, since these parametrisations need to be evaluated quite frequently in a climate simulation, a simple parametrisation scheme that is easy and thust fast to calculate might be preferred over complex ones that try to mimic physical effects as close as possible. However, all parametrisations have the drawback of being limited in their applicability to certain conditions that they have been designed for. An overview of this topic topic as well as a comprehensive introduction to parametrisations can be found in Stensrud (2007).

One of the most prominent physical processes to be parametrised in many climate simulations that operate on large grid scales is convection. To maintain the observed tropospheric lapse rate and moisture distribution, heat is transferred vertically by convection, which can not be simulated directly by coarse grid simulations. However, recent climate simulations operating on finer grids are able to explicitly resolve convection thus making the convection parametrisations redundant. The flow behaviour of two of these so-called Convection Permitting Climate Models (CPCMs) are investigated during in this work (see section 4.1.1).

D Grid Staggering in Atmospheric Models

Many atmospheric models use a spatial grid staggering in order to ensure stability or increase precision of the numerical integration method. This means that velocity components (wind speeds) are staggered one half of a grid length away from the thermodynamic variables (grid cell center), leading to their allocation at the faces of the grid cell cubes. This situation is shown in Fig. D.1. All velocity components included in the output of an atmospheric model need to be interpolated to the center of the grid cells before they can be used by the flow analysis tool.

To get the value of the horizontal wind component u at the center of grid cell i, one needs to calculate the average of the u values at locations $i-1/2$ and $i+1/2$ (to calculate v at j, one needs to average over $j-1/2$ and $j+1/2$, respectively).

Furthermore, in order to convert from the vertical model levels to geometric height, the constant geopotential PHB and its perturbation PH (defined at the grid cell faces together with the vertical wind component) can be employed using

$$h_w(i,j,k) = \frac{PHB(i,j,k) + PH(i,j,k)}{g_0} \,, \tag{D.1}$$

whereas $h_w(i,j,k)$ is the geometric height of the horizontal face of the grid cell at location (i,j,k) and $g_0 = 9.81\,\mathrm{m\,s^{-2}}$ denotes the standard acceleration due to gravity. The

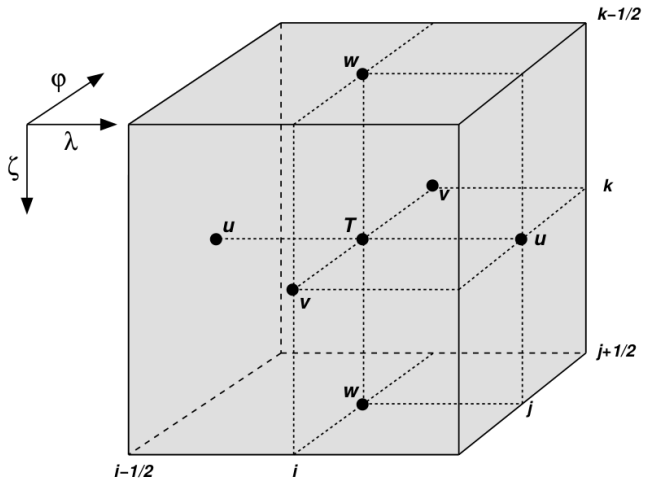

Fig. D.1 Arakawa-C/Lorenz grid staggering used in many atmospheric models. u, v and w denote wind components. From Doms and Baldauf (2015).

geometric height of the grid cell centre h_T can be found by interpolation using

$$h_T(i,j,k) = \frac{PHB(i,j,k) + PH(i,j,k) + PHB(i,j,k+1) + PH(i,j,k+1)}{2g_0} \,. \qquad \text{(D.2)}$$

Abstract:
The atmospheric flow behaviour of air in complex terrain plays an important role for weather phenomena such as mountain waves, downslope windstorms and barrier jets. For any Regional Climate Model (RCM) to be meaningful, it is necessary that these flow-above and blocked-flow situations are replicated correctly.
This work demonstrates how to use the Froude number of continuum mechanics to categorise the flow behaviour of air in the complex terrain of the European Alps on a grid cell resolution. The influences of moisture and condensation effects are also considered. Besides distinguishing flow-above from block-flow situations, it is shown how the Froude number also provides information on the stratification properties of air.
The developed flow analysis tool is used to study the differences between two RCMs (the COSMO model in CLimate Mode (CCLM) and the Weather Research and Forecasting Model (WRF)), both operating on convection permitting scale (3 km grid spacing). The analysis fields from the operational Swiss forecast system COSMO-7 (7 km grid spacing) are used as a reference data set. To compare the flow behaviour of these data sets, five distinct flow categories are introduced and their frequency of occurrence for November 2002 based on hourly data is examined in detail. The located differences between the data sets highlight how this tool can help to improve RCMs and their accuracy regarding flow-above and blocked-flow situations and therefore contribute to model development.

Zum Inhalt:
Das Strömungsverhalten der atmosphärischen Luftschichten spielt vor allem in Gebirgsregionen eine wichtige Rolle und ist für zahlreiche Wettersituationen wie Schwerewellen, Föhnwinde und Barrier Jets verantwortlich. Damit Regionale Klimamodelle (RCMs) aussagekräftige Ergebnisse liefern können, müssen diese Um- und Überströmungseffekte korrekt reproduziert werden.
Diese Arbeit demonstriert, wie die Froude-Zahl der Kontinuumsmechanik dazu benutzt werden kann, das Strömungsverhalten der Atmosphäre auf Basis von dreidimensionalen Daten zu kategorisieren. Die Einflüsse von Luftfeuchtigkeit (insbesondere Kondensationseffekte) werden dabei berücksichtigt. Neben der Unterscheidung von geblockten und nicht-geblockten Luftpaketen (*Um*strömung bzw. *Über*strömung) wird gezeigt, wie die Froude-Zahl dazu benutzt werden kann, um die Luftstabilität zu analysieren.
Mit Hilfe des in dieser Arbeit entwickelten Tools zur automatisierten Kategorisierung des Strömungsverhaltens der Atmosphäre werden die Unterschiede zwischen zwei RCMs mit konvektionserlaubender Auflösung (3 km), dem COSMO model in CLimate Mode (CCLM) und dem Weather Research and Forecasting Model (WRF), sowie dem operationellen schweizer Wettervorhersagesystem COSMO-7 (7 km Auflösung) untersucht. Dazu werden in dieser Arbeit fünf unterschiedliche Strömungskategorien definiert. Die relative Häufigkeit dieser Strömungskategorien im November 2002 wird auf Basis von stündlichen Datensätzen analysiert. Die gefunden Unterschiedene zwischen den Modellen zeigen auf, wie dieses Tool zur Verbesserung des Strömungsverhaltens von RCMs beitragen kann.

Wegener Center for Climate and Global Change
University of Graz
Brandhofgasse 5
A-8010 Graz, Austria
www.wegcenter.at
ISBN 978-3-9503918-6-2